Title
The Spatial Patterning of Signals during Neutrophil Migration

Author
Houk, Andrew

Publication Date
2011

Peer reviewed|Thesis/dissertation

The Spatial Patterning of Signals during Neutrophil Migration

by

Andrew Houk

DISSERTATION

Submitted in partial satisfaction of the requirements for the degree of

DOCTOR OF PHILOSOPHY

in

Cell Biology

in the

GRADUATE DIVISION

[redacted]

to my family

Mary, Sam and Linda Houk

ACKNOWLEDGEMENTS

Many people have helped me get to this point. First and foremost, none of my scientific accomplishments would have been possible without my family. My parents are both scientists and they nurtured my curiosity from an early age. Dad, in particular, was my personal science teacher when I was a child. As I finished high school, Dad put me into contact with Xueyu Song at Iowa State University who gave me my first research job. He also gave me advice on choosing graduate schools and emphasized the impact that my choice would have on my subsequent career. He encouraged me to seek out the best school, even if that school was a long way from home. My mom and sister have been wonderful sources of love and support during my entire life and especially during graduate school.

My success as a graduate student resulted from the outstanding preparation that I received at the University of Iowa. The biology courses there inspired me to pursue pure biology research instead of protein biophysics and drug development as I had initially planned. Bob Malone, Steven Greene and others were also such rigorous teachers that I succeeded in my graduate course work despite having no research experience in biology. I was also fortunate to do research in the labs of three excellent mentors: Xueyu Song, Jan Jensen and Andy Robertson. Xueyu gave me the chance to do actual research for the first time and helped me learn computer programming. Andy and Jan taught me physical chemistry and protein biophysics. While I am no longer a protein biophysicist, the physical intuition I gained from them has been the foundation for everything I have learned and thought about as a graduate student.

My decision to study at UCSF was the best I have ever made. This is an inspiring place to work. The faculty pursue interesting new questions and seek out novel ways to solve them, in contrast to so many scientists who fear to wander out of their comfort zone. The diversity of research here and collaborative atmosphere were a

breath of fresh air from some of the narrowly focused and territorial programs that I had experienced previously. My new social environment here was also great. For the first time in my life, I was completely surrounded by people who shared my curiosity and interests. All of my fears about graduate school dissolved immediately and I realized that, instead of a hellish crucible, my years at UCSF would be the best of my life to date. I am very grateful to have spent time in this wonderful place and I thank the entire community here for making it such an intellectually stimulating yet warm and supportive place to study.

The intellectual talent and friendly atmosphere that make UCSF great are exemplified by my classmates. Like all first-year Tetrad students, we quickly bonded into a close, yet inclusive group of friends who shared experiences that I will never forget. These people were so special to me that I dreaded the prospect of graduating and separating from them. Han was the first friend I made at UCSF and I am still inspired by her combination of kindness and strength. Sarah shared my love of AFC North football and is such an amazing person that I like her even though she roots for the Ravens. Will is so kind and generous that I am not even jealous of his extreme handsomeness. Mike combines intellectual talent and intensity with a certain wildness giving him a unique personality that is always fun to be around. Paul and Manisha are two of the funniest people I know and they have always cheered me up when I was down. While my graduate school years have been wonderful, there have been some tough times that I could not have handled without them.

I was fortunate to work with great collaborators at other institutions. Steve, Lani, Sasha and Sigurd made me realize there was far more to reaction/diffusion systems than I initially believed. My Yale collaborators Cecile, Ross and Eric performed one of the most critical experiments in the paper. I owe Jason Forster and Beezer de Martelly a huge debt of gratitude for housing me while I was at Yale and being wonderful friends.

I owe a debt of gratitude to the Weiner lab – Arthur, Sheel, Sarah, Delquin, Oliver, Anna (x2), Grace, Jared, Doug and Julie - for being great colleagues and friends over the years. The diverse scientific interests and creative approaches used by the different lab members make our lab a very interesting place to study. I give special thanks to the early lab members, Arthur and Sheel for making our lab the close circle of friends that it is and for taking the time to teach me skiing. I thank Jared for being an excellent mathematical biology teacher who deepened my understanding of reaction/diffusion systems. All of my experiments depended on the hard work of Sarah and Grace who kept our lab running smoothly over the years.

I am extremely grateful for my thesis committee. Given their intelligence, personalities and research interests, I don't think I could find a better committee if I scoured the entire planet. Wallace's unique approach to science drew me into the field of cell biology when I arrived at UCSF. I love the way he thinks. Wendell's scientific vision inspires everyone who knows him. Dyche is a uniquely brilliant man and his advice for me to keep an open mind and look beyond reaction/diffusion systems for neutrophil polarity became the foundation of my thesis work. Henry taught me the importance of clarity in thought, speech and writing. They are a dream team of scientists and I am lucky to have studied with them.

Finally, I must acknowledge my outstanding mentor, Orion Weiner. Orion has many qualities that make him a great PI. He genuinely cares about everyone in his lab and works very hard to be the best mentor he can be. While my interest in chemotaxis research has temporarily wavered from time to time; his enthusiasm for science and support for me never wavered. When I needed day-to-day guidance and support, especially early on, he provided it. Despite his willingness to help, he does not overdo it and micromanage. He has allowed me to grow into an independent scientist, confident in my own ideas and abilities – something I was not when first I joined his lab. I have

never met anybody who has more cool ideas than Orion does. He taught me the power of thinking outside the box and applying new technology to my research. He encourages all of his students to pursue projects that interest them even when that leads us into areas that are new to him. As a result, the research projects in our lab are very diverse which makes the lab a fascinating place to be. In short, he is exactly the type of curiosity-driven scientist with diverse research interests that I aspire to become.

ABSTRACT

The spatial patterning of signals during neutrophil migration

Andrew Houk

Cells must migrate for neurons to make connections with distant partners, immune cells to find their prey and cancer cells to metastasize. Actin filament assembly at the leading edge and actomyosin contraction at the trailing edge cause protrusion and retraction, respectively, which enable most human cells to crawl through their environment. We do not understand how the cell spatially restricts the signals promoting actin assembly to the leading edge.

In my first project, I described the polarization behavior of an essential actin assembly signal (WAVE complex) in response to external chemical cues (chemoattractants). At that time, there were contradictory theories for the establishment of polarized signals. One theory proposed that the signals initiate throughout the cell and then get carved down to just the leading edge. A competing theory proposed that the signals only initiate at the leading edge. We found that both modes of polarization can occur, depending on the circumstances. At high chemoattractant concentrations, WAVE signaling initiates uniformly and subsequently polarizes. At lower concentrations, WAVE signaling was polarized from the outset. Polarized initiation even occurred in response to uniform chemoatractant, although gradients made it more likely.

In my second project, I investigated the spatial restriction mechanism itself. Numerous theoretical studies proposed that the signals at the front limit themselves either by depleting essential signaling components via diffusion and capture or by producing inhibitory molecules which diffuse throughout the cell. I used cell-severing experiments and severe morphological perturbations to demonstrate that the leading edge produces an inhibitory signal that operates when the cell morphology reduces diffusion by 1000-fold. We suspected that tension in the membrane or cytoskeleton

provides an inhibitory signal that does not spread via diffusion. Consistent with this, we found that tension in the membrane increases during polarization. Furthermore, we demonstrated that artificial tension increases, induced by micropipette suction, inhibited WAVE signaling throughout the cell. Finally, artificially reducing membrane tension with hyperosmotic buffer expands signaling throughout the cell leading to uniform protrusion. Thus, membrane tension spatially confines signals to the leading edge to enable migration.

Table of contents

Dedication and Acknowledgments iii

Abstract viii

List of Figures xi

Chapter 1: Introduction 1

Chapter 2: Neutrophils establish rapid and robust WAVE complex polarity in an actin dependent fashion 9

Chapter 3: Membrane tension maintains cell polarity by confining signals to the leading edge during neutrophil migration 42

Chapter 4: Summary and Future Directions 108

Publishing Agreement 115

List of figures

Chapter 1

None

Chapter 2

Figure 1: Propagating waves of the WAVE complex are mechanistically conserved in other mammalian cells and represent a dynamic quantitative polarity readout in neutrophils. 25

Figure 2: Cells establish Hem-1 wave asymmetry through either focused generation or uniform generation followed by selection. 26

Figure 3: Directional bias limits wave generation in response to small increases in mean receptor occupancy. 27

Figure 4: Actin polymer is required for establishment of Hem-1 wave asymmetry. 28

Figure S1: Illustration of image acquisition, processing, and analysis used in this paper. 37

Figure S2: Angle difference and quiescence period do not affect wave distribution, nor are cells skewed toward original micropipette location. 39

Figure S3: The WAVE complex biochemically fractionates to the plasma membrane upon fMLP stimulation and latrunculin treatment. 41

Chapter 3

Figure 1: Conceptual mechanisms for long-range inhibiton 71

Figure 2: Maintenance of polarity in tethered cells 72

Figure 3: Cells generate a new pseudopod after severing 73

Figure 4: The tethered morphology dramatically attenuates diffusion 74

Figure 5: Membrane tension increases during protrusion 75

Figure 6: Increasing tension with aspiration reversibly inhibits leading-edge protrusion and signaling 76

Figure 7: Membrane tension reduction causes expansion of signaling 77

Figure S1: Polarization behavior for cut cells is similar to highly stretched cells 102

Figure S2: Cutting the tether with a laser beam does not activate neighboring cells 103

Figure S3: Correcting for fluorophore regeneration during FRAP experiments 104

Figure S4: Membrane tension measurements in the presence of blebbistatin 105

Figure S5: Analysis of plasma membrane integrity during aspiration experiments 106

Figure S6: Membrane tension reduction, but not cytoskeletal tension reduction, results in ectopic leading-edge signaling 107

CHAPTER ONE

Introduction

While appearing static to the naïve observer, many types of human cells are constantly changing their shape and moving around. Cells must be able to migrate for a human body to form and remain alive. When we were embryos, cells migrated throughout our bodies to form our peripheral nervous system, facial bones and the connective tissue of the heart. When we cut ourselves, neighboring cells at the wound edge migrate into the wound to heal it. As you read this, immune cells are patrolling your tissues looking for invading pathogens. When we get an infection, huge numbers of immune cells crawl through blood vessels into the tissues to destroy the pathogens. The ability to migrate is a basic property of cells and a major focus of cell biology. In the next several paragraphs, I will outline our current understanding of cell migration, focusing on the immune cells (neutrophils) that I study.

Different types of cells utilize vastly different types of movement. Cells that swim through liquids, like bacteria and sperm, use spinning flagella to move similar to the propeller of a ship. In general, cells moving on or through solid environments do not use flagellar propulsion and instead perform a crawling-like process. In this case, growing networks of interlinked actin filaments push on the plasma membrane at the leading edge causing it to protrude while myosin contracts the actin network at the rear of the cell causing retraction. Protrusion at the front and retraction of the rear causes the cell to crawl as a single cohesive unit. A complex signaling network interprets environmental cues to determine the direction of movement and ensures that protrusion/retraction only occur at opposite ends of the cell.

What do we know of this signaling network? We know many of the receptors that directly transduce environmental cues (attractant and repellant molecules, often referred to as chemoattractants and chemorepellants). We know that the receptors activate a class of signaling proteins called heterotrimeric G-proteins – although the receptors

probably activate additional unknown proteins as well. We also know the final three signals directly leading to the creation of actin networks. The signaling protein Rac activates a pentameric protein complex known as Scar/WAVE (hereafter referred to as "WAVE complex"), which in turn activates a protein complex called Arp2/3. Arp2/3 nucleates new actin filaments on the sides of existing filaments to create a branched actin network that is good at pushing on things.

While we know what happens at the top and bottom of the signaling cascade, we know little of what happens in the middle – which is where a lot of the important processing occurs. For example, we did not understand how the cell restricts Rac activity to the front (a process called *polarization*) or how the cell orients Rac activity with respect to external cues (gradients of chemoattractant).

As I began my thesis project, there was significant debate on the orientation behavior of cells. Some studies had shown that cells preferentially generate protrusions in the direction of highest chemoattractant. However, others showed that cells make protrusions in random directions and then selectively maintain the ones directed up the gradient. The confusion on orientation behavior precluded detailed mechanistic insight on how the system works.

These studies were performed in various different cell types and under differently shaped gradients, adding to the confusion. Furthermore, they used cellular morphology as a readout, which is insensitive and not necessarily representative of the underlying signaling events. It was obvious that we needed a more detailed study that analyzed the internal signals under a variety of external conditions. However, it was not clear which signals should be examined because several studies casted doubt on the importance of PIP_3, which had been thought to be the most important intracellular actin-assembly signal. Meanwhile, several labs showed that the Rac/WAVE complex signaling axis was essential for actin assembly and leading edge formation in numerous cell types. Thus, it

seemed that the most important signals to analyze were Rac and the WAVE complex itself.

Shortly before I began graduate school, Orion made two discoveries that put our lab in a unique position to address this issue. First, he discovered that the WAVE complex is essential for Rac activation – suggesting that it is not merely a passive recipient of upstream signals but directly participates in the signaling process via positive-feedback onto Rac. Second, he found that the WAVE complex is recruited to the membrane in an autocatalytic fashion that produces propagating spatial waves, which collectively form the leading edge. We thought that the waves are the fundamental signaling units of protrusion. Thus, we decided to determine the behavior of waves in response to external cues in order to resolve the debate described above.

We first showed that waves orient with respect to the chemoattractant gradient better than morphologically visible protrusions do. Furthermore, we demonstrated that waves occur in other cell types besides neutrophils – indicating that they are a widely occurring phenomenon. These two observations further convinced us that waves were the best signaling readout to examine.

We found that a cell exposed to chemoattractant gradients can selectively generate waves in the proper direction; however, it can also generate waves uniformly and selectively retain the ones in the right direction. The cell employs the former mechanism when chemoattractant concentrations are low and the latter when concentrations are high. The average chemoattractant concentration is a stronger determinant of behavior than the slope of the gradient. Thus, the contradictory reports in the published literature were simply due to the different chemoattractant concentrations used in different studies.

A similar theme emerged in cells treated with spatially uniform chemoattractant where small doses cause focused generation of waves while high doses cause uniform

wave production that ultimately gets pruned down into a focused zone. This observation surprised us because uniform chemoattractant causes all previously examined signals to initially activate uniformly and then break symmetry. It demonstrates that stationary cells have internal spatial heterogeneities that can convert uniform receptor activity into polarized downstream signals.

While this study characterized the polarization behavior of waves in the cell, we still did not understand *why* they polarize. Why is Rac extremely active at the leading edge, and inactive everywhere else? Positive feedback appears to amplify Rac to high levels at the leading edge. But if positive feedback exists, then there must be some type of confinement mechanism to prevent the spot of Rac activity from growing and taking over the entire cell. Rac was thought to produce long-range autoinhibition to restrict itself to the leading edge and prevent other leading edges from forming. There were several theories for how the autoinhibition worked but all of them were hypothetical; we had no direct experimental evidence for any of them. In fact, we had no proof that Rac autoinhibition exists in the first place. I devoted the second half of my graduate career to addressing these questions.

We devised a simple experiment to determine whether the existing leading edge generates long-range autoinhibition. We reasoned that if the leading edge produces inhibition then the removal of the leading edge should cause ectopic protrusions elsewhere in the cell. We used a focused laser beam to cut off the leading edge and found that the cells often made new protrusions after severing. To our knowledge, this experiment was the first direct evidence that the leading edge inhibits protrusion at other cellular locations. How does the long-range inhibition work? The most popular proposal was that Rac recruited its own activators to the membrane at the leading edge via diffusion and capture, eventually resulting in activator depletion from the cytosol. Alternatively, Rac could simply produce its own inhibitory molecules, which then diffuse

throughout the cell. Both types of inhibition schemes are often referred to as reaction-diffusion systems due to their reliance on diffusion to spread inhibition throughout the cell.

We tested the importance of diffusion by dramatically changing cellular morphology to reduce diffusive communication. To our surprise, the leading edge inhibited protrusion even when it was only connected to the rest of the cell by a long, thin tether of membrane-bound cytoplasm. We used fluorescence recovery after photobleaching to show that, on average, the tether reduced diffusive communication between leading edge and the rest of the cell by one thousand fold. We simulated three published diffusion-based inhibition models and found that the inhibitory molecules or limiting components require very large diffusion coefficients to function in this context. These diffusion coefficients were an order of magnitude larger than those measured for proteins in cytosol and were comparable to those of water itself. This suggested to us that the long-range inhibition does not spread throughout the cell via diffusion. Thus, we started to consider alternative models for long-range inhibition that do not involve inhibitory molecules produced at the front or sequestration of signaling molecules by the front.

At this time, there was a growing body of evidence in other migratory cells that tension in the plasma membrane and/or cytoskeleton inhibits protrusion. We suspected that tension could be responsible for the long-range inhibition observed in neutrophils. We thought that the cellular deformation resulting from leading edge protrusion could increase tension in the cytoskeleton or plasma membrane. In support of this, we observed that in cells with tethered morphologies, the leading edge often snapped back to the cell body very rapidly, suggesting high tension in those cells.

We therefore decided to investigate the possibility of tension as a long-range inhibitor in neutrophils. We focused on three major questions. First, does leading edge

protrusion increase tension? We knew from our severing experiments that the leading edge inhibits protrusions elsewhere, so the leading edge should be the source of inhibitory tension. Second, if we artificially manipulate tension does that affect the signals that promote protrusion (i.e. Rac)? Our hypothesis was that artificially increasing tension in a migrating neutrophil would inactivate Rac and shut down leading edge protrusion. Third, if inhibitory tension does exist then is it in the plasma membrane or cytoskeleton?

To address the first question, we measured membrane tension during leading edge formation. We knew from conversations with other labs that cytoskeletal tension increases during neutrophil activation – although this increase is largely due to myosin contraction and not leading edge protrusion. We used an optical trap to measure membrane tension on neutrophils as they began protruding in response to chemoattractant. We captured small, adhesive polystyrene beads in the optical trap and then touched the cell surface with the trapped beads before pulling them away. Occasionally, the bead would stick to the membrane so that when we withdrew the bead, we pulled out a thin tube of membrane as well. This membrane tube exerted a pulling force on the bead, which was proportional to the membrane tension. To our delight, we found that the pulling force doubled during leading edge protrusion.

We addressed the second and third questions in a variety of ways. We first used micropipette suction to deform the cell and increase tension in the plasma membrane and cytoskeleton. This tension increase dramatically reduced Rac activity and stopped protrusion. Furthermore, when we released the suction pressure, allowing the cell to relax into its normal shape, Rac became active again and protrusion resumed. This demonstrated that the deformation-induced Rac inhibition was not an artifact of irreversible suction-induced cell damage. Thus, we had shown that tension inhibits the signals that drive protrusion. Next, we wondered whether increased tension is required

to confine Rac to a limited region of the cell. We used the myosin inhibitor blebbistatin to reduce tension in the cytoskeleton and found that Rac activity remained confined to a single zone (the leading edge) in blebbistatin treated cells. In parallel experiments, we used a hyperosmotic buffer to reduce membrane tension. In contrast to blebbistatin treatment, the reduction of membrane tension caused Rac to be active over a much larger region of the cell – resulting in uniform expansion. We also noticed that blebbistatin potentiated the effects of hyperosmotic buffer. These results told us two things. First, tension is required to restrict Rac activity to the leading edge during migration. Second, the inhibitory tension is primarily in the membrane, although the synergy between blebbistatin and hyperosmotic buffer suggests that cytoskeletal tension may play a supporting role as well.

Together our data support the following model for neutrophil polarity. Leading edge protrusion deforms the cell, which increases plasma membrane tension in the same way that inflating a balloon increases tension in the skin of the balloon. The increased membrane tension inhibits Rac activity to keep it confined to a limited region of the cell (the leading edge). We suspect that tension-based inhibition is ideally suited to maintain cell polarity during migration *in vivo*. As neutrophils pursue their prey during an infection, they must frequently crawl between cells and between extracellular matrix filaments. As they squeeze through these tight spaces, the cellular cross-section gets narrow, which would interfere with diffusive inhibition in the same way a tether would. Mechanical feedback seems to be a common design principle in the organization of multicellular tissues and organs and it now appears to pattern signals within individual cells as well.

CHAPTER TWO

Neutrophils establish rapid and robust WAVE complex polarity in an actin-dependent fashion

SUMMARY

Asymmetric intracellular signals enable cells to migrate in response to external cues. The multiprotein WAVE (SCAR/WASF) complex activates the actin-nucleating Arp2/3 complex [1-4] and localizes to propagating “waves”, which direct actin assembly during neutrophil migration [5, 6]. Here, we observe similar WAVE complex dynamics in other mammalian cells and analyze WAVE complex dynamics during the establishment of neutrophil polarity. Earlier models proposed that either spatially-biased generation [7] or selection of protrusions [8] enables chemotaxis. These models require existing morphological polarity to control protrusions. Similar spatially-biased generation and selection of WAVE complex recruitment occur in morphologically unpolarized neutrophils during the development of their first protrusions. Additionally, several mechanisms limit WAVE complex recruitment during polarization and movement: intrinsic cues restrict WAVE complex distribution during the establishment of polarity, and asymmetric intracellular signals constrain WAVE complex distribution in morphologically polarized cells. External gradients can overcome both intrinsic biases and control WAVE complex localization. Following latrunculin-mediated inhibition of actin polymerization, addition and removal of agonist gradients globally recruits and releases the WAVE complex from the membrane. Under these conditions the WAVE complex no longer polarizes, despite the presence of strong external gradients. Thus, actin polymer and the WAVE complex reciprocally interact during polarization.

RESULTS AND DISCUSSION

For neutrophils, the WAVE complex is required for motility and polarity, exhibits propagating waves generated through rapid sequential rounds of recruitment and release of the complex from the plasma membrane, and requires actin polymer for its recycling from the plasma membrane [6]. Several pieces of evidence suggest that similar WAVE complex dynamics organize protrusion in other metazoan cells: the WAVE complex is required for the movement and morphogenesis of cells in *C. elegans* [9], *Drosophila* [10, 11], and mice [3, 12]; the WAVE complex localizes to the tips of protruding lamellipodia in B16F10 murine melanoma cells [13] (Fig. 1A, Movie S1); and this leading edge localization represents rapidly cycling WAVE complex (half life 8.6 s for WAVE in murine melanoma cells compared to 6.4 s for the Hem-1 component of the neutrophil WAVE complex [6, 14]). To determine whether actin assembly is required for WAVE complex recycling in cells other than neutrophils, we depolymerized the actin cytoskeleton in B16F10 cells expressing a fluorescently tagged subunit of the WAVE complex (Abi1). Actin disassembly resulted in cessation of WAVE complex movement and significant WAVE complex enrichment (2.4 +/- 0.3 fold, $P < .005$) near the plasma membrane (Fig. 1B, Movie S2), suggesting that actin is also required for WAVE complex recycling in these cells. Collectively, these data suggest that the WAVE complex exhibits similar properties in diverse mammalian cells and is likely a general regulator of cell migration throughout metazoans.

WAVE complex dynamics exhibit several features that make them ideal for a quanitative readout of polarity in neutrophils over other internal signals such as the phospholipid PIP_3 [15-17] or cell morphology [7, 8, 18]. PIP_3 now appears to be dispensable for chemotaxis in neutrophils [19] and *Dictyostelium* [20]. Morphology results from the integration of many signals. Compared to previous morphological

studies [7, 8], our use of TIRF imaging only visualizes the footprint of the cell and is likely to emphasize stabilized protrusions versus protrusions that are unlinked to the surface.

To compare WAVE complex dynamics and cell morphology as readouts for polarity, cells were analyzed following exposure to chemoattractant gradients (Fig. 1C and 1D; Movie S3). We developed automated image analysis software (Fig. S1) to quantify the input/output relation between agonist perturbations and WAVE complex response for a large number of cells. When a micropipette containing agonist was moved to a new location, WAVE complex recruitment changed more dramatically in the following 10 s than did cell morphology (Fig 1C., compare 84 s to 94 s). For quiescent cells exposed to gradients of chemoattractant, significant WAVE complex asymmetry was observed in the absence of obvious morphological polarity (Fig 2B, 14 s time point). These cells were examined to determine how morphological protrusions and WAVE complex behavior relate to the external gradient. Both were highly accurate in predicting the ultimate gradient direction. However, protrusions oscillated significantly around the true gradient direction (SD = 24%), whereas changes in WAVE complex behavior were more precisely aligned with the gradient (SD = 12%). These data suggest that under our stimulation conditions, changes in WAVE complex dynamics represent a more quantitative and robust readout of polarity than cell morphology.

The establishment of WAVE complex asymmetry was determined by analyzing the signaling response of an initially quiescent cell to chemoattractant (Fig. 2A). Quiescent cells were exposed to a range of agonist increases and split into two equal size populations based on the size of the mean estimated increase in fractional receptor occupancy (see methods; 0.63 was the median increase). Among our micropipette experiments, the average receptor occupancy change correlated better with cell response than did the slope of the gradient (data not shown). Cells exposed to increases in estimated mean receptor occupancy from 0 to < 0.63 responded to the new

gradient with focused generation of WAVE complex recruitment (Fig 2B and 2D; Movie S4). For mean receptor occupancy increases greater than 0.63, most cells produced a relatively uniform distribution of WAVE complex recruitment that collapsed into a focused distribution on the up-gradient surface (Fig. 2C and 2D; Movie S5). In both cases, WAVE complex asymmetry ultimately aligns with the external agonist gradient.

Previous analyses of uniformly stimulated neutrophils showed initially uniform signaling responses before cells became polarized [6, 17]. It is unknown whether cells can also produce initially asymmetric signaling in response to uniform stimulation. To test this possibility, the responses of quiescent cells (when cells lost all WAVE complex dynamics and any obvious morphological front and back) were observed. A mean receptor occupancy increase from 0 to 0.1 caused the cells to produce focused WAVE complex recruitment (Fig. 3A and 3C; Movie S6). In contrast, a mean receptor occupancy increase from 0 to 0.7 caused cells to produce a spatially uniform distribution of WAVE complex recruitment that ultimately collapsed into a focused distribution (Fig. 3B and 3C; Movie S7). The first detectable response in either case occurred approximately 12-18 s after stimulation. These data suggest that immediate signaling asymmetries are generated in response to small agonist steps. Previous studies examining the establishment of PIP_3 asymmetry [17] and WAVE asymmetry [6] used larger increases in receptor occupancy, conditions that prevent the initially focused recruitment of WAVE complex in response to uniform chemoattractant (Fig. 3B and 3C).

There are several potential mechanisms that could constrain WAVE complex dynamics to a limited region of the cell surface. For instance, upstream molecular asymmetries could act to restrict WAVE complex recruitment to a limited region of the cell surface during the establishment of polarity. An example of this type of internal directional bias is centrosome position, which influences the initial axis of morphological polarity in response to uniform chemoattractant [21]. This sort of intrinsic bias could be

responsible for the immediate WAVE complex polarity in response to small steps in uniform chemoattractant (Fig 3A). A second source of internal directional bias could operate during migration. Moving cells have polarized morphologies and intracellular signals, which act as a directional bias to restrict protrusions near the existing leading edge [18, 22]. This type of internal directional bias spatially restricts WAVE complex responses for intermediate increases in mean receptor occupancy (Fig. 3D; Movie S8) in a manner similar to the role of an intrinsic bias during the establishment of polarity. However, larger steps of uniform agonist elicited uniform WAVE complex recruitment (Fig. 3E and 3F; Movie S9), indicating that this bias can be overcome.

During chemotaxis, both an external bias from the agonist gradient and the cell's intrinsic biases could influence the establishment of WAVE complex asymmetries. In other cell types, such as *Dictyostelium*, only agonist gradients and not uniform chemoattractant produce signaling polarity [15]. Under these conditions, it is difficult to separate the effects of intrinsic biases from the external gradient. In contrast, neutrophils exhibit signaling polarity in uniform chemoattractant as well as gradients [17], enabling us to determine the role of internal directional bias independent of gradient sensing.

External gradients limit the spatial exent of WAVE complex recruitment for initially quiescent cells (Fig. 2B). Here, external gradients set the final direction of WAVE complex polariy and overwhelm any internal signaling biases within the cell. This occurs for mean receptor occupancy increases less than 0.63. In contrast, under a condition where only internal signaling biases operate, a similar step size (an increase of 0.34), elicited uniform WAVE complex recruitment in polarized cells (Fig. 3E). These data indicate that gradient sensing can overwhelm intrinsic biases and can constrain cell responses over a larger range of agonist increases than intrinsic biases.

Some cues such as PIP_3 can polarize in the absence of actin rearrangements [15, 17, 23, 24], but it is unclear whether WAVE complex asymmetry can also be uncoupled from downstream actin-dependent morphological rearrangements. Neutrophils were treated with latrunculin to inhibit actin polymerization. Even in the absence of external agonist, latrunculin transiently increased the concentration of WAVE complex at the membrane (Fig. 4A, 40 s). Under these conditions the WAVE complex still responds to stimulation, although WAVE complex puncta are observed instead of propagating waves. Sudden addition of an agonist gradient increased WAVE complex recruitment (Fig. 4A, 160 and 300 s), whereas removal of agonist caused WAVE complex release from the membrane (Fig. 4A, 200 and 360 s). In latrunculin-treated cells exposed to gradients of chemoattractant, the localization of WAVE complex was relatively uniform (Fig. 4B, 170 and 330 s; Movie S10). Untreated cells typically produced focused WAVE complex recruitment in response to small increases in agonist gradients (Fig. 2B). In contrast, latrunculin-treated cells that experienced a similar increase in receptor occupancy exhibited a significantly wider WAVE complex distribution (Fig. 4C). Therefore, actin polymer, which is generated downstream of the WAVE complex, also appears to be required for the initial generation of WAVE complex asymmetry in neutrophils. Additionally, for control cells exposed to large increases in agonist gradients, the WAVE complex was initially relatively uniform but resolved into a more focused distribution over time. In contrast, this selection mechanism was not apparent over the timescale analyzed in latrunculin-treated cells (Fig. 4D). Furthermore, previous studies implicate actin polymer as a factor that stabilizes signaling components at the membrane [25, 26], whereas our data suggest that actin polymerization can also remove signaling proteins from the membrane.

Biochemical fractionation was used to measure WAVE complex enrichment near the plasma membrane as a complement to our TIRF studies. A significant two-fold

enrichment of the WAVE complex was observed in the plasma membrane fraction following stimulation and actin depolymerization, indicating that at least some of the TIRF-visible pool of the WAVE complex represents plasma-membrane association (Fig. S3).

CONCLUSIONS

Two models cover how cells reorient polarity during directional migration, and aspects of each apply to how cells initially establish polarity. One model showed that *Dicytostelium* respond by selectively retaining the pseudopod that experiences the highest agonist concentration, rather than biasing pseudopod generation [8]. In our system, the unit of selection is not a pseudopod, but rather smaller organizing units consisting of WAVE complex recruitment events. In contrast, the local generation model for chemotaxis proposes that the chemotactic behavior of the cell is the sum of local, independent protrusion events all over the surface of the pseudopod [7]. Once a cell is polarized, the probability of a protrusion event occurring in a particular location on the pseudopod depends on the relative local concentration of agonist. Extending this generation-based model to unpolarized cells can explain how a cell can initially bias WAVE complex asymmetry when receptor occupancy is low (~0.1), a phenomenon inexplicable by a selection-based model. However, the generation-based model fails to explain how cells could generate WAVE complex recruitment everywhere and selectively retain WAVE complex recruitment up-gradient; so each model succeeds where the other fails.

We propose a model where local generation events are linked to cellular adaptation machinery. For small increases in agonist, a generation-based mechanism leads to immediately focused polarity. For larger increases in agonist, the generation machinery is saturated, resulting in a uniform WAVE complex distribution. In this case,

global adaptation allows the cell to selectively retain WAVE complex recruitment to achieve WAVE asymmetry in a direction set by intrinsic biases or the external gradient. Our model enables the cell to balance rapid polarization (initial signal generation to the up-gradient side) with a more robust polarization (a slower gradual selection of uniform signal distribution, which can occur over a wider range of stimulation conditions). Importantly, the dominant mechanism of polarization depends on the amount of stimulation.

Intriguingly, actin polymerization is essential for WAVE complex polarization during chemotaxis. There are many examples of loss-of-function perturbations of chemotactic signaling that block intracellular signaling responses including PIP_3 generation, Ras and Rac activation, actin polymerization, and morphological changes in response to external chemoattractant [5, 26-32]. The WAVE complex is the first example of an intracellular signal that depends on actin polymer for its polarization but not for its global responsiveness to stimulation.

ACKNOWLEDGEMENTS

We thank John Sedat for image denoising collaboration, the Nikon Imaging Center at UCSF for Matlab analysis software, Scott Foster for leukocyte preparation, and Henry Bourne, Oliver Hoeller, Steve Altschuler, Lani Wu, Max Krummel, Benjamin Rhau, Mark Von Zastrow, Alexander Watters, Sarah Wilson, Bryant Chhun, Delquin Gong, and Julie Wu for helpful comments on the manuscript.

This work was supported by NIH R01 (GM084040), the UCSF/UCB Cell Propulsion lab (an NIH Nanomedicine Development Center), a Searle Scholars Award, an American Heart Association National Scientist Development Grant, a National Defense Science and Engineering Graduate Fellowship to A. Millius, an American Heart Association Graduate Fellowship to A. Houk, and an Achievement Awards for College Scientists (ARCS) Scholarship to S. Dandekar.

REFERENCES

1. Machesky, L.M., and Insall, R.H. (1998). Scar1 and the related Wiskott-Aldrich syndrome protein, WASP, regulate the actin cytoskeleton through the Arp2/3 complex. Curr Biol *8*, 1347-1356.
2. Kunda, P., Craig, G., Dominguez, V., and Baum, B. (2003). Abi, Sra1, and Kette control the stability and localization of SCAR/WAVE to regulate the formation of actin-based protrusions. Curr Biol *13*, 1867-1875.
3. Steffen, A., Rottner, K., Ehinger, J., Innocenti, M., Scita, G., Wehland, J., and Stradal, T.E. (2004). Sra-1 and Nap1 link Rac to actin assembly driving lamellipodia formation. The EMBO journal *23*, 749-759.
4. Stradal, T.E., and Scita, G. (2006). Protein complexes regulating Arp2/3-mediated actin assembly. Current opinion in cell biology *18*, 4-10.
5. Weiner, O.D., Rentel, M.C., Ott, A., Brown, G.E., Jedrychowski, M., Yaffe, M.B., Gygi, S.P., Cantley, L.C., Bourne, H.R., and Kirschner, M.W. (2006). Hem-1 complexes are essential for Rac activation, actin polymerization, and myosin regulation during neutrophil chemotaxis. PLoS Biol *4*, e38.
6. Weiner, O.D., Marganski, W.A., Wu, L.F., Altschuler, S.J., and Kirschner, M.W. (2007). An Actin-Based Wave Generator Organizes Cell Motility. PLoS Biol *5*, e221.
7. Arrieumerlou, C., and Meyer, T. (2005). A local coupling model and compass parameter for eukaryotic chemotaxis. Developmental cell *8*, 215-227.
8. Andrew, N., and Insall, R.H. (2007). Chemotaxis in shallow gradients is mediated independently of PtdIns 3-kinase by biased choices between random protrusions. Nature cell biology *9*, 193-200.
9. Patel, F.B., Bernadskaya, Y.Y., Chen, E., Jobanputra, A., Pooladi, Z., Freeman, K.L., Gally, C., Mohler, W.A., and Soto, M.C. (2008). The WAVE/SCAR complex promotes polarized cell movements and actin enrichment in epithelia during C. elegans embryogenesis. Dev Biol.
10. Zallen, J.A., Cohen, Y., Hudson, A.M., Cooley, L., Wieschaus, E., and Schejter, E.D. (2002). SCAR is a primary regulator of Arp2/3-dependent morphological events in Drosophila. The Journal of cell biology *156*, 689-701.
11. Rogers, S.L., Wiedemann, U., Stuurman, N., and Vale, R.D. (2003). Molecular requirements for actin-based lamella formation in Drosophila S2 cells. The Journal of cell biology *162*, 1079-1088.
12. Rakeman, A.S., and Anderson, K.V. (2006). Axis specification and morphogenesis in the mouse embryo require Nap1, a regulator of WAVE-mediated actin branching. Development (Cambridge, England) *133*, 3075-3083.
13. Hahne, P., Sechi, A., Benesch, S., and Small, J.V. (2001). Scar/WAVE is localised at the tips of protruding lamellipodia in living cells. FEBS Lett *492*, 215-220.
14. Lai, F.P., Szczodrak, M., Block, J., Faix, J., Breitsprecher, D., Mannherz, H.G., Stradal, T.E., Dunn, G.A., Small, J.V., and Rottner, K. (2008). Arp2/3 complex interactions and actin network turnover in lamellipodia. The EMBO journal *27*, 982-992.
15. Parent, C.A., Blacklock, B.J., Froehlich, W.M., Murphy, D.B., and Devreotes, P.N. (1998). G protein signaling events are activated at the leading edge of chemotactic cells. Cell *95*, 81-91.
16. Meili, R., Ellsworth, C., Lee, S., Reddy, T.B., Ma, H., and Firtel, R.A. (1999). Chemoattractant-mediated transient activation and membrane localization of

Akt/PKB is required for efficient chemotaxis to cAMP in Dictyostelium. The EMBO journal *18*, 2092-2105.
17. Servant, G., Weiner, O.D., Herzmark, P., Balla, T., Sedat, J.W., and Bourne, H.R. (2000). Polarization of chemoattractant receptor signaling during neutrophil chemotaxis. Science *287*, 1037-1040.
18. Zigmond, S.H., Levitsky, H.I., and Kreel, B.J. (1981). Cell polarity: an examination of its behavioral expression and its consequences for polymorphonuclear leukocyte chemotaxis. The Journal of cell biology *89*, 585-592.
19. Ferguson, G.J., Milne, L., Kulkarni, S., Sasaki, T., Walker, S., Andrews, S., Crabbe, T., Finan, P., Jones, G., Jackson, S., et al. (2007). PI(3)Kgamma has an important context-dependent role in neutrophil chemokinesis. Nature cell biology *9*, 86-91.
20. Hoeller, O., and Kay, R.R. (2007). Chemotaxis in the absence of PIP3 gradients. Curr Biol *17*, 813-817.
21. Xu, J., Van Keymeulen, A., Wakida, N.M., Carlton, P., Berns, M.W., and Bourne, H.R. (2007). Polarity reveals intrinsic cell chirality. Proc Natl Acad Sci U S A *104*, 9296-9300.
22. Xu, J., Wang, F., Van Keymeulen, A., Herzmark, P., Straight, A., Kelly, K., Takuwa, Y., Sugimoto, N., Mitchison, T., and Bourne, H.R. (2003). Divergent signals and cytoskeletal assemblies regulate self-organizing polarity in neutrophils. Cell *114*, 201-214.
23. Janetopoulos, C., Ma, L., Devreotes, P.N., and Iglesias, P.A. (2004). Chemoattractant-induced phosphatidylinositol 3,4,5-trisphosphate accumulation is spatially amplified and adapts, independent of the actin cytoskeleton. Proc Natl Acad Sci U S A *101*, 8951-8956.
24. Xu, X., Meier-Schellersheim, M., Yan, J., and Jin, T. (2007). Locally controlled inhibitory mechanisms are involved in eukaryotic GPCR-mediated chemosensing. The Journal of cell biology *178*, 141-153.
25. Devreotes, P., and Janetopoulos, C. (2003). Eukaryotic chemotaxis: distinctions between directional sensing and polarization. The Journal of biological chemistry *278*, 20445-20448.
26. Sasaki, A.T., Chun, C., Takeda, K., and Firtel, R.A. (2004). Localized Ras signaling at the leading edge regulates PI3K, cell polarity, and directional cell movement. The Journal of cell biology *167*, 505-518.
27. Shefcyk, J., Yassin, R., Volpi, M., Molski, T.F., Naccache, P.H., Munoz, J.J., Becker, E.L., Feinstein, M.B., and Sha'afi, R.I. (1985). Pertussis but not cholera toxin inhibits the stimulated increase in actin association with the cytoskeleton in rabbit neutrophils: role of the "G proteins" in stimulus-response coupling. Biochem Biophys Res Commun *126*, 1174-1181.
28. Wu, L., Valkema, R., Van Haastert, P.J., and Devreotes, P.N. (1995). The G protein beta subunit is essential for multiple responses to chemoattractants in Dictyostelium. The Journal of cell biology *129*, 1667-1675.
29. Kumagai, A., Hadwiger, J.A., Pupillo, M., and Firtel, R.A. (1991). Molecular genetic analysis of two G alpha protein subunits in Dictyostelium. The Journal of biological chemistry *266*, 1220-1228.
30. Sun, C.X., Downey, G.P., Zhu, F., Koh, A.L., Thang, H., and Glogauer, M. (2004). Rac1 is the small GTPase responsible for regulating the neutrophil chemotaxis compass. Blood *104*, 3758-3765.

31. Chen, L., Iijima, M., Tang, M., Landree, M.A., Huang, Y.E., Xiong, Y., Iglesias, P.A., and Devreotes, P.N. (2007). PLA2 and PI3K/PTEN pathways act in parallel to mediate chemotaxis. Developmental cell *12*, 603-614.
32. Veltman, D.M., Keizer-Gunnik, I., and Van Haastert, P.J. (2008). Four key signaling pathways mediating chemotaxis in Dictyostelium discoideum. The Journal of cell biology *180*, 747-753.

FIGURE LEGENDS

Figure 1. Propagating waves of the WAVE complex are mechanistically conserved in other mammalian cells and represent a dynamic quantitative polarity readout in neutrophils (A) Representative TIRF timelapse sequences for a B16F10 fibroblast cell migrating on fibronectin expressing Abi1 (a component of the WAVE complex) tagged with YFP. Similar to HL-60 cells, propagating waves of the WAVE complex are observed at the leading edge (Movie S1). (B) Representative Abi1-YFP TIRF timelapse sequences for a migrating B16F10 fibroblast exposed to 10 μM latrunculin at 0 s. Similar to HL-60 cells, B16F10 cells exhibit an enrichment of WAVE complex near the membrane following latrunculin treatment, suggesting a role for actin polymer in WAVE complex recycling (Movie S2). (C) Representative brightfield and Hem1-YFP TIRF timelapse sequences for a HL-60 cell executing a turn in response to a change in the direction of the agonist gradient (Movie S3). (D) Corresponding heatmap shows wave response. Green arrow indicates initial up-gradient direction; red arrow indicates final up-gradient direction. Bars, 5 μm.

Figure 2. Cells establish Hem-1 wave asymmetry through either focused generation or uniform generation followed by selection. (A) Illustration of experimental setup. An agonist gradient was applied to a cell and then removed. This process was necessary to ensure quiescence because cells adhered to a coverslip often exhibited polarity and motility even in the absence of chemoattractant. Cells were classified as quiescent when they lost all wave dynamics and any obvious morphological front and back. The micropipette was repositioned at a different angle and the gradient reapplied at t = 0 s. Therefore, all cells start with a mean receptor occupancy of 0 for this figure. The angle difference and interval between agonist applications did not affect

WAVE complex distribution, nor did the cell retain memory of the original micropipette position after the micropipette was turned back on (Fig. S2). (B and C) Representative DIC and Hem-1-YFP TIRF timelapse sequences and corresponding heatmaps show that cells exhibit a focused (B, Movie S4) or uniform (C, Movie S5) distribution of waves. Note that wave asymmetry is apparent in the absence of any obvious morphological differences (arrowheads). Green arrows indicate initial up-gradient direction; red arrows indicate final up-gradient direction. Bars, 5 μm. (D) Bar graph (left) of a 20 s average of wave response immediately after gradient reapplication. Black bars show response for cells with mean receptor occupancy (post-stimulation) of <0.63. Gray bars indicate cells with mean receptor occupancy (post-stimulation) of >0.63. Error bars are s.e.m. Asterisks indicate statistically significant differences between means of each sector ($p < 0.05$, Student's t-test). Dot plot (right) shows a statistically significant difference ($p = .03$, Student's t-test) between the mean width (red line) of the distributions as defined in Fig. S1.

Figure 3. Directional bias limits wave generation in response to small increases in mean receptor occupancy. (A and B) Initially quiescent cells were subjected to spatially uniform mean receptor occupancy increases from 0 to 0.1 (at t = 0 s), which produced focused waves (A, Movie S6), or 0 to 0.7 (at t = 0 s), which produced a spatially uniform distribution of Hem-1 waves that ultimately collapsed into a focused distribution (B, Movie S7). Bars, 5 μm. (C) Dot plot shows a statistically significant difference ($p = .001$, Student's t-test) between the mean width (red line) of the distributions. (D and E) Representative timelapse images of cells with prepolarized WAVE complex distributions responding to spatially uniform increases in mean receptor occupancy from (D) 0.61 to 0.73 (n = 6, Movie S8) or (E) 0.39 to 0.73 (n = 8, Movie S9). (F) Dot plot shows a statistically significant difference ($p = 0.002$, Student's t-test)

between the changes in wave width for small versus large increases in mean receptor occupancy (note that mean receptor occupancies are statistically different even after removing the outlier for the 0.61 to 0.73 increase). These data suggest that intrinsic directional bias can maintain the asymmetric distribution of Scar/WAVE over a limited range of agonist concentrations in both quiescent and prepolarized cells.

Figure 4. Actin polymer is required for establishment of Hem-1 wave asymmetry

(A) Transient fMLP pulses (red trace) induce transient Hem-1-YFP (black trace) accumulation at the membrane. An initially migrating cell was subjected to 20 μM latrunculin treatment to depolymerize the actin cytoskeleton (40 s). This induced Hem-1-YFP recruitment even in the absence of external stimuli. Subsequent fMLP pulses from a micropipette (160 and 300 s) induced further recruitment. When the agonist was removed, Hem-1-YFP quickly disappeared from the membrane. (B) Selected TIRF and DIC images (Movie S10) from the traces shown in (A). Red arrows indicate direction of gradient pulses. Arrowheads indicate areas of significant Hem-1-YFP accumulation at the membrane. Note the broad distribution following each agonist pulse. Bar, 5 μm. (C) Dot plot of a 20 s average of wave response immediately after an agonist pulse for cells untreated (-lat) and treated with 20 μM latrunculin (+lat). There is a statistically significant difference between the mean width (red lines) of the two populations ($p = .002$, Student's t-test). (D) Untreated cells that showed an initially broad wave distribution after an agonist pulse were compared to latrunculin-treated cells. The wave distribution in untreated cells converged into a focused distribution, whereas the wave distribution in latrunculin-treated cells did not converge. Error bars are s.e.m. Inset shows statistical significance between the difference in mean sectors (red lines) of the two populations ($p = .002$, Student's t-test).

Figure 1

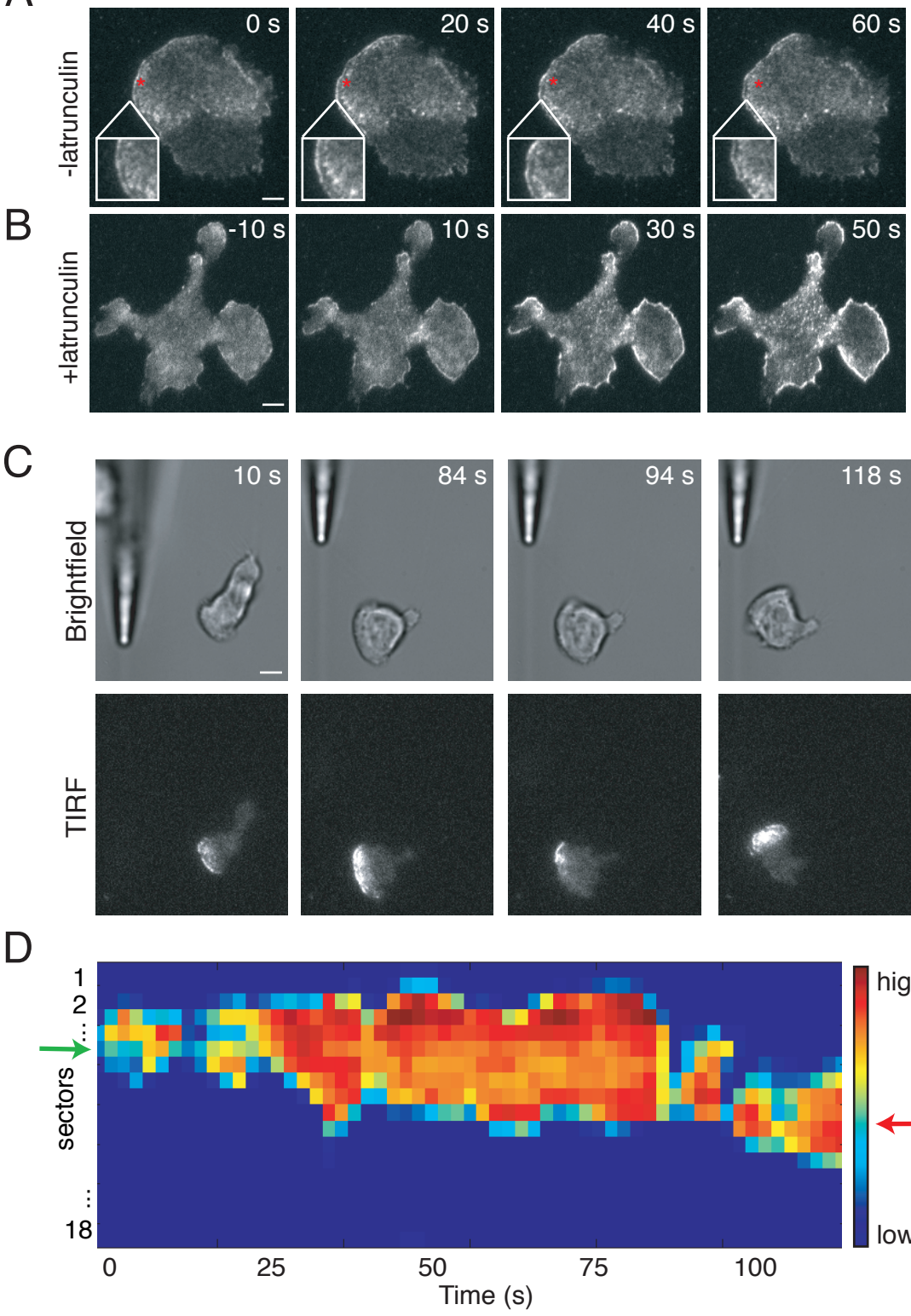
A
-latrunculin
0 s
20 s
40 s
60 s
B
+latrunculin
-10 s
10 s
30 s
50 s
C
Brightfield
10 s
84 s
94 s
118 s
TIRF
D
sectors
1
2
...
18
high
low
0
25
50
75
100
Time (s)

Figure 2

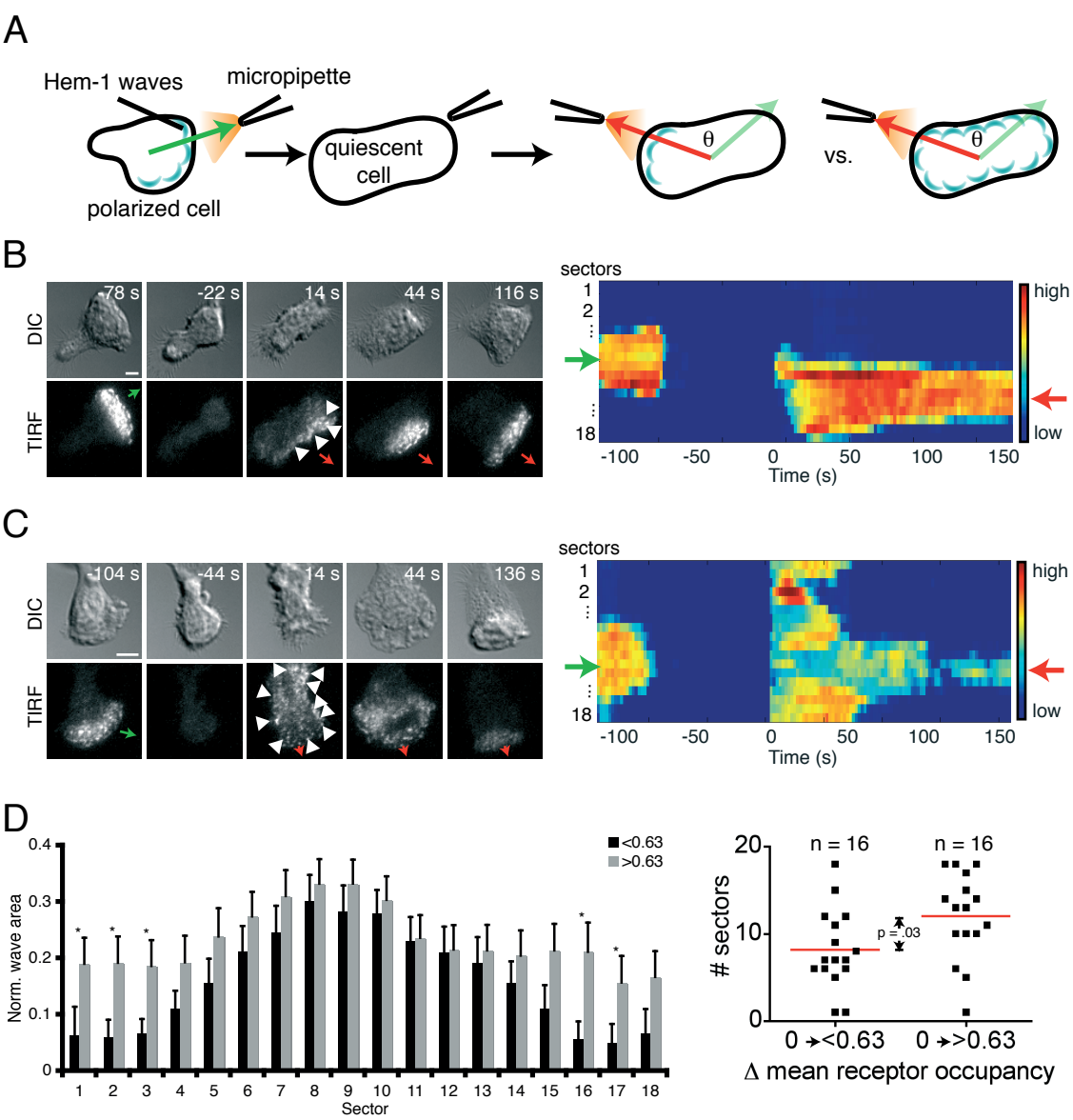
A
Hem-1 waves
micropipette
polarized cell
quiescent cell
θ
vs.
θ
B
DIC
TIRF
-78 s
-22 s
14 s
44 s
116 s
sectors
1
2
18
high
low
-100
-50
0
50
100
150
Time (s)
C
DIC
TIRF
-104 s
-44 s
14 s
44 s
136 s
sectors
1
2
18
high
low
-100
-50
0
50
100
150
Time (s)
D
Norm. wave area
0.4
0.3
0.2
0.1
0
<0.63
>0.63
1
2
3
4
5
6
7
8
9
10
11
12
13
14
15
16
17
18
Sector
n = 16
n = 16
20
10
0
# sectors
p = .03
0 →<0.63
0 →>0.63
Δ mean receptor occupancy

Figure 3

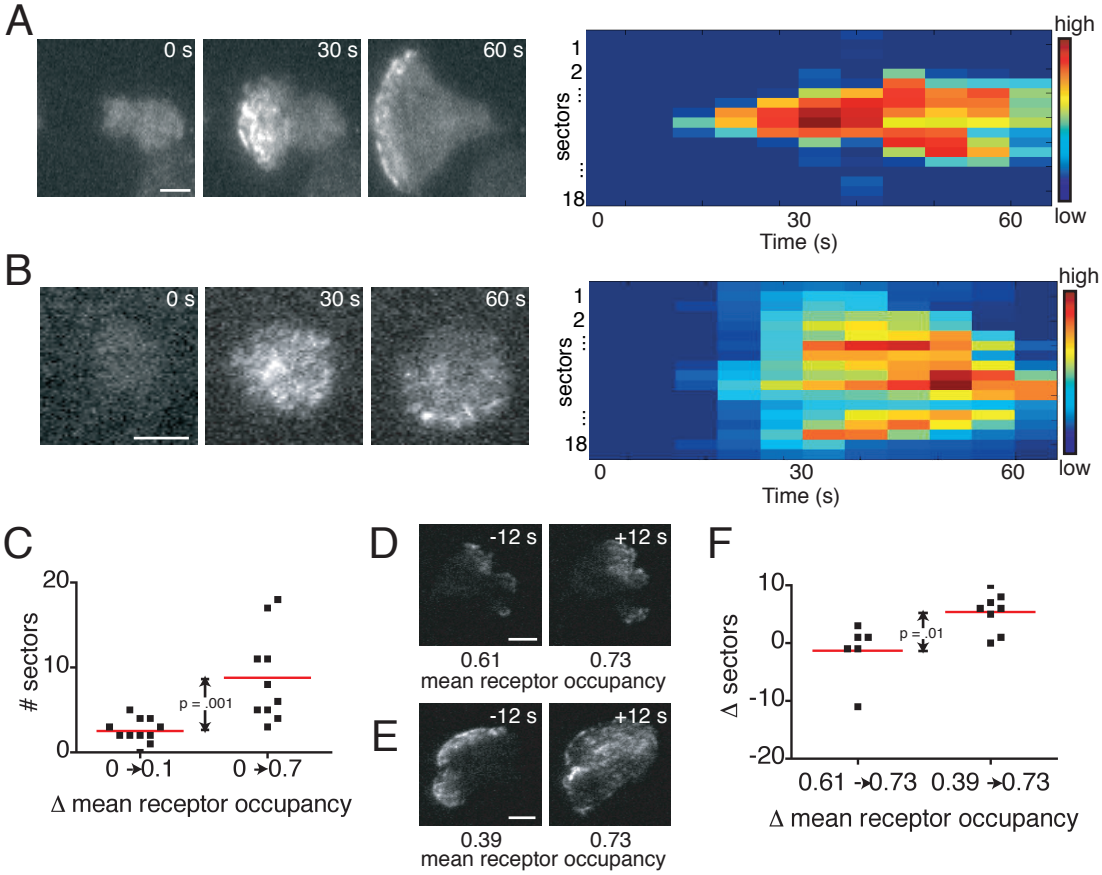
A
0 s
30 s
60 s
sectors
1
2
18
0
30
60
Time (s)
high
low
B
0 s
30 s
60 s
sectors
1
2
18
0
30
60
Time (s)
high
low
C
sectors
20
10
0
p = .001
0 →0.1
0 →0.7
Δ mean receptor occupancy
D
-12 s
+12 s
0.61
0.73
mean receptor occupancy
E
-12 s
+12 s
0.39
0.73
mean receptor occupancy
F
Δ sectors
10
0
-10
-20
p = .01
0.61 →0.73
0.39 →0.73
Δ mean receptor occupancy

Figure 4

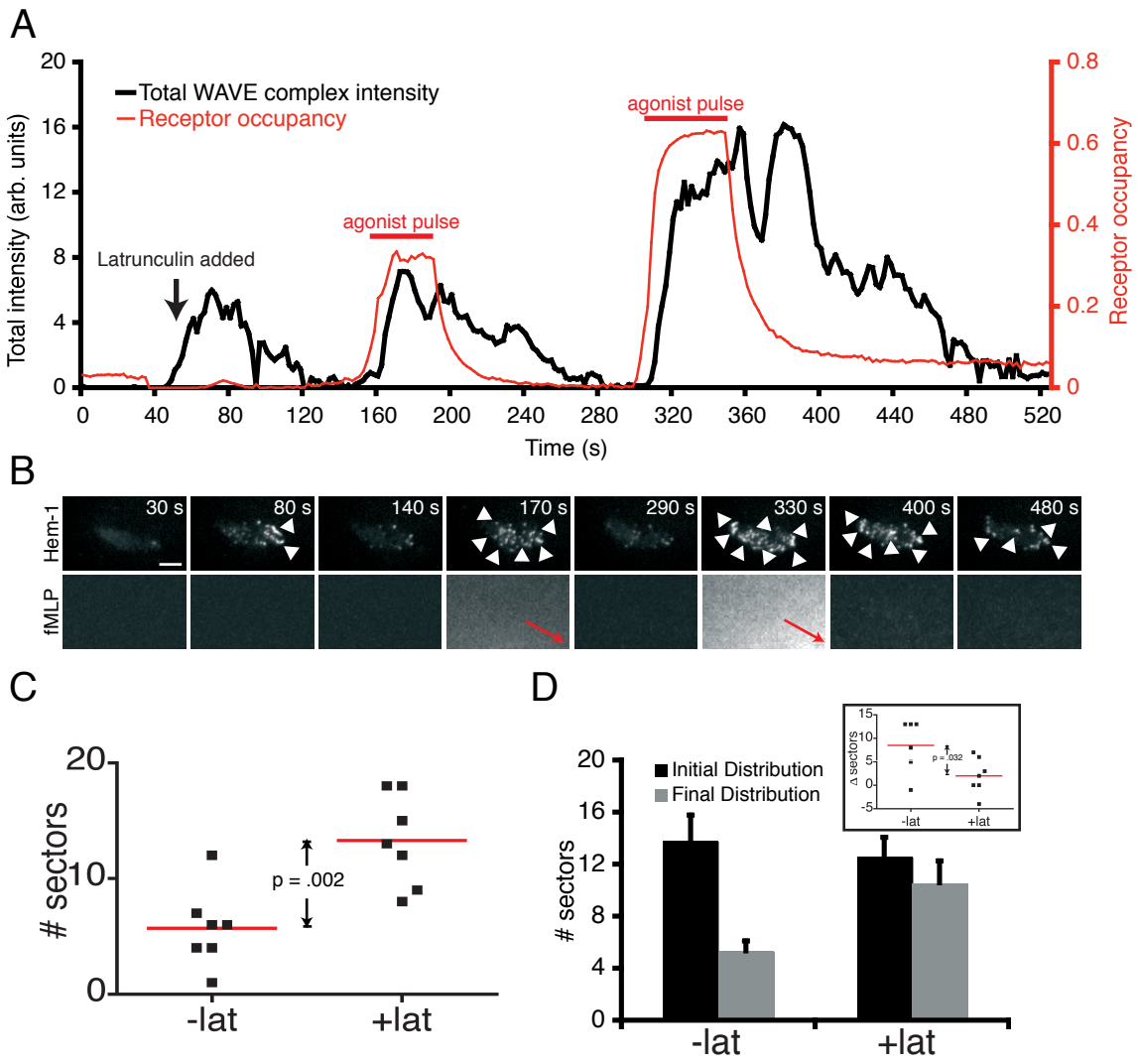
A
Total WAVE complex intensity
Receptor occupancy
agonist pulse
agonist pulse
Latrunculin added
Total intensity (arb. units)
Receptor occupancy
Time (s)
B
Hem-1
fMLP
30 s
80 s
140 s
170 s
290 s
330 s
400 s
480 s
C
# sectors
p = .002
-lat
+lat
D
Initial Distribution
Final Distribution
sectors
Δ sectors
p = .032
-lat
+lat

Supplemental Information

Cell culture

The HL-60 cell line stably expressing Hem-1-YFP was generated, cultured, and differentiated as described previously [1]. Cells were plated on #1.5 coverslips (Lab-Tek) precoated with 0.2 mg/ml bovine fibronectin (Sigma) and stimulated in RPMI plus L-glutamine, 10% FBS, and 25 mM HEPES (10-041-CM, Fisher) with indicated concentrations of formyl-met-leu-phe (fMLP, Sigma) mixed with Alexa594 hydrazide (Invitrogen).

Image acquisition

Images were taken at 37°C on a Nikon Eclipse TE2000-E inverted microscope with a 60x PlanApo TIRF 1.49 NA objective and an electron microscopy charge-coupled device (EM-CCD) camera (Cascade II 512, Photometrics; http://www.photomet.com). Sample drift was minimized using an autofocus system (Perfect Focus, Nikon). 514 nm and 561 nm lasers (20 mW ion and solid-state lasers, Melles Griot) were used for excitation of Hem-1-YFP and Alexa594 hydrazide, respectively. Nikon Elements software version 3.0 was used for image acquisition; levels of still images were adjusted linearly in Photoshop to enhance contrast.

Micropipette experiments

Typical imaging conditions used 600 ms YFP-TIRF, 20 ms 594-TIRF, and 5 ms DIC exposures every 2 s with near maximal multiplication on the EMCCD to minimize phototoxicity and photobleaching. Glass filaments (TW100F-4, World Precision Instruments) were pulled on Sutter Model P-87 (program: heat = 750, pull = 0, velocity = 20, time = 250, pressure = 100, loops 2 or 3 times) to achieve ~2-3 μm needle tip diameter. Needles were backfilled with 5 μl 200 nM fMLP containing 10 μM Alexa594 and held by a micromanipulator (MM-89, Narishige). Agonist flow rate was controlled by adjusting balance pressure between 0-3 psi on an IM-300 injection system (Narishige) connected to a needle holder (MINJ4, Tritech).

Uniform experiments

Typical imaging conditions used ND2 neutral density filter, 100 ms YFP-TIRF, 20 ms 594-TIRF and 5 ms DIC exposures every 6 s with maximal multiplication on the EMCCD to minimize phototoxicity and photobleaching. Cells were plated in 0.1 mL media. The coverslips were then placed on the microscope and timelapse movies were started. Increases or decreases in chemoattractant were monitored by mixing Alexa594 into the fMLP stocks. For Fig. 3, cells were pre-stimulated with 20 nM fMLP for 3 minutes; the fMLP was completely removed

and replaced with 0.1 mL media before the start of the movie. This was done to increase the number of quiescent cells prior to stimulation with chemoattractant.

Biochemical fractionation

One liter of 7 day differentiated HL-60 cells (or fresh pig leukocytes [2]) were spun at 1500 x g for 15 min, resuspended in ~4 mL mHBSS containing 3 mM DFP, and incubated for 15 min at room temperature. Cells were spun again for at 90 x g for 10 min and resuspended in warm cavitation buffer or cavitation buffer containing 1 μM fMLP, 10 mM Latrunculin B, and 100 μM GTPγS. Cells were pressurized for 5 min at 37°C for 5 min, lysed into 2 mM EGTA, spun at 1500 x g for 10 min at 4°C, layered on a 15%/38%/60% sucrose gradient, and spun at 100,000 x g for 1 hour. The 15%/38% interface was collected, TCA precipitated, and subsequently used for a Western blot for Hem-1 and NaK ATPase (a membrane loading control).

WAVE complex visualization within B16F10 cells

B16F10 cells were cultured on 10 cm dishes in MEM Eagle with Earle's BSS, 10% FBS, non-essential amino acids and antibiotic/antimycotic. The cells were transfected with Abi1-YFP (Lipofectamine2000) 48 hours before the experiment. For WAVE-complex visualization during spreading (Fig. 1A), Abi1-YFP transfected cells were trypsinized, replated on fibronectin-coated coverslips, and Abi1-YFP was visualized immediately after replating. This allowed us to visualize

waves as cells initially spread along the coverslip. For latrunculin experiments, Abi1-YFP transfected cells were trypsinized and replated on fibronectin-coated coverslips 24 hours before the experiment. AlF was added (30 mM NaF, 50 μM $AlCl_3$) to stimulate spreading approximately 10 min before Latrunculin B addition (10 μM). In both sets of experiments, the cells were plated on LabTek 8 well #1.5 coverglass chambers pre-coated with 0.05 mg/mL bovine fibronectin (Sigma).

Image denoising

The Hem1-YFP channel of the acquired image series was cropped in space so that only one cell was in the image. The resulting time series was denoised in collaboration with John Sedat, using software developed by Jerome Boulanger, as described in (Fig. S1), [3]. Default parameters were chosen for a two-dimensional time series, except for the patch size, which was 7x7. The effect of the denoising was to remove speckle noise from the background while minimizing feature loss from the waves, which enabled semi-automatic segmentation of the cell and wave regions. In the fMLP channel for both the uniform and micropipette experiments, the true intensities should be smoothly varying. To get rid of hot pixels (extremely bright or dark relative to surroundings), the fMLP channel was smoothed following image reconstruction examples [4].

Image segmentation

The cell region (region of the cell in contact with the coverslip) and wave region (regions of high Hem-1 density within the cell region) were defined using the denoised image. Two user-defined intensity thresholds were chosen using ImageJ, where the region of the image above the low threshold was the cell region (distinguishable above background because of cytosolic Hem-1) and the region of the image above the high threshold was the wave region (Fig. S1). For Fig. 4 (latrunculin-treated cells), the cytosolic pool of Hem-1 was greatly depleted, making it difficult to segment the cell region automatically. For these experiments, the cell region was a user-defined circle. This method of segmentation consistently underreported the width of the WAVE distribution when compared to the intensity thresholding method using control cells (data not shown).

Image analysis

We wrote analysis software in MATLAB 7.4 with Image Processing Toolbox and the help of the Nikon Imaging Center at UCSF. For the micropipette experiments, the position of the micropipette was calculated as the centroid of the region with intensity greater than 0.9*(max pixel intensity of smoothened fMLP channel). A total of 18 sectors covering 20 degrees each were drawn using the centroid of the cell region as the center, and the up-gradient direction falling

between the middle two sectors. Sectors with normalized fractional wave area greater than 0.1 were defined as sectors containing waves (Fig. S1).

Concentration and receptor occupancy calculations

For uniform chemoattractant experiments, chemoattractant concentration was known, and receptor occupancy was calculated in the same manner as the gradient experiments. For the gradient experiments, concentration was calculated by mixing known concentrations of Alexa594 with fMLP and drawing a standard curve under defined imaging conditions. Two curves were created and the average slope used to calculate concentration. Fractional receptor occupancy was calculated for a K_d of 9.5 nM for binding of fMLP to its receptor [5] using the equation $receptor\_occupancy = [fMLP]/(K_d + [fMLP])$**.** Background was subtracted from the fMLP channel in the following manner. For experiments in which some images in the time series were taken with no chemoattractant (Fig. 2), the median fMLP intensity during periods without chemoattractant was subtracted from all measurements, and all resulting negative values set to 0. For experiments in which all images had some chemoattractant, a constant value (2500 CCD counts) estimated from the median fMLP intensity values reported from the images without chemoattractant was instead subtracted, and all resulting negative values set to 0. To calculate the concentration following a change in fMLP, the median sector fMLP intensity for frames in the 20 s prior to

and following the change were calculated, and the minimum and maximum for each, respectively, was used.

Statistical methods

Unpaired, two-tailed Student's t-test was used to compare mean widths for wave distributions in Fig. 2-4. These data met the criteria for normalcy by the Lilliefors test and the Jarque-Bera test.

References

1. Weiner, O.D., Marganski, W.A., Wu, L.F., Altschuler, S.J., and Kirschner, M.W. (2007). An Actin-Based Wave Generator Organizes Cell Motility. PLoS Biol *5*, e221.
2. Weiner, O.D., Rentel, M.C., Ott, A., Brown, G.E., Jedrychowski, M., Yaffe, M.B., Gygi, S.P., Cantley, L.C., Bourne, H.R., and Kirschner, M.W. (2006). Hem-1 complexes are essential for Rac activation, actin polymerization, and myosin regulation during neutrophil chemotaxis. PLoS Biol *4*, e38.
3. Kervrann, C., and Boulanger, J. (2006). Optimal spatial adaptation for patch-based image denoising. IEEE Trans Image Process *15*, 2866-2878.
4. Gonzalez, R., Woods, R., Eddins, S. (2004). Digital Image Processing Using Matlab, (Upper Saddle River, NJ: Pearson Prentice Hall).
5. Coats, W.D., Jr., and Navarro, J. (1990). Functional reconstitution of fMet-Leu-Phe receptor in Xenopus laevis oocytes. The Journal of biological chemistry *265*, 5964-5966.

Supplemental Figures

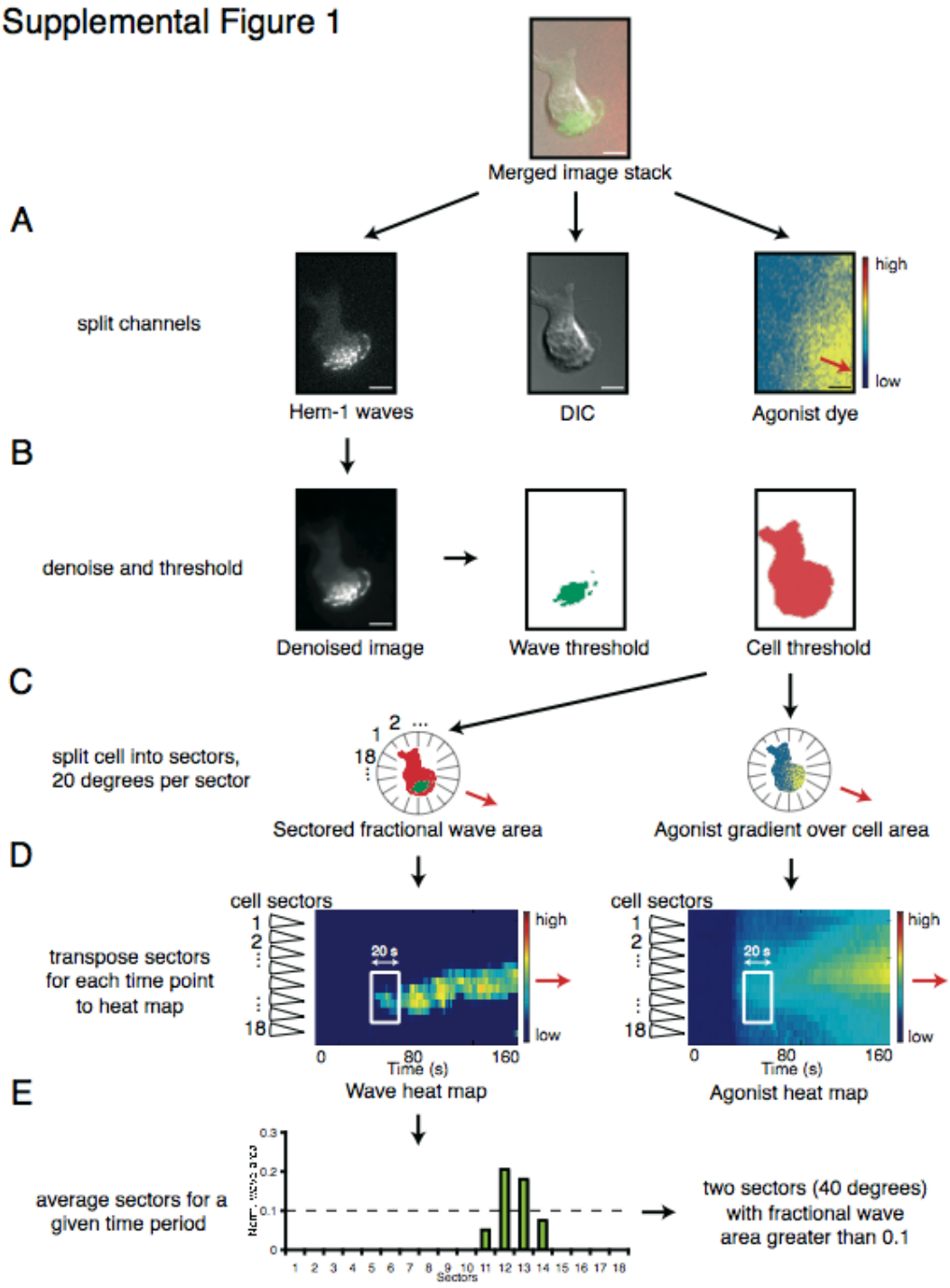

Figure S1. Illustration of image acquisition, processing, and analysis used in this paper. (A) A three channel merged image stack (top) is split into Hem-1-YFP distribution in TIRF (left), cell morphology in DIC (center), and fMLP distribution (visualized by the fluorescent dye Alexa594, which has a similar diffusion constant to fMLP) in TIRF (pseudocolored, right). Red arrow indicates up-gradient direction. Bars, 5 μm. (B) The Hem-1 channel is denoised and segmented into a wave region, which contains high Hem-1 concentration on the membrane, and a cell region, which additionally contains cytosolic Hem-1. (C) For each frame the cell is divided up into 18 equiangular sectors with the up-gradient direction (denoted by red arrow) between sectors 9 and 10. For each sector the ratio of wave area to cell area (left) and the average agonist concentration (right) are calculated. This agonist concentration is converted into a crude estimation of mean receptor occupancy using the reported Kd of the formyl peptide receptor {Coats, 1990 #27}. (D) The data from (C) is pictorially represented over the course of the movie as a heatmap. Each column is one time point, and the rows correspond to each sector's position, with high values shown in red and low values shown in blue. (E) The average of the wave response over 20 s following an agonist change (white box shown in D) is plotted on a bar graph, and the number of sectors with fractional wave area > 0.1 defines the width of the wave region.

Supplemental Figure 2

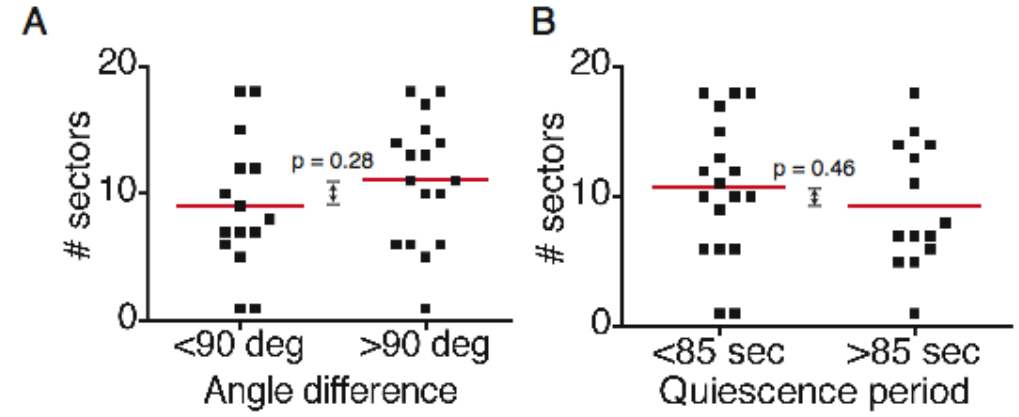

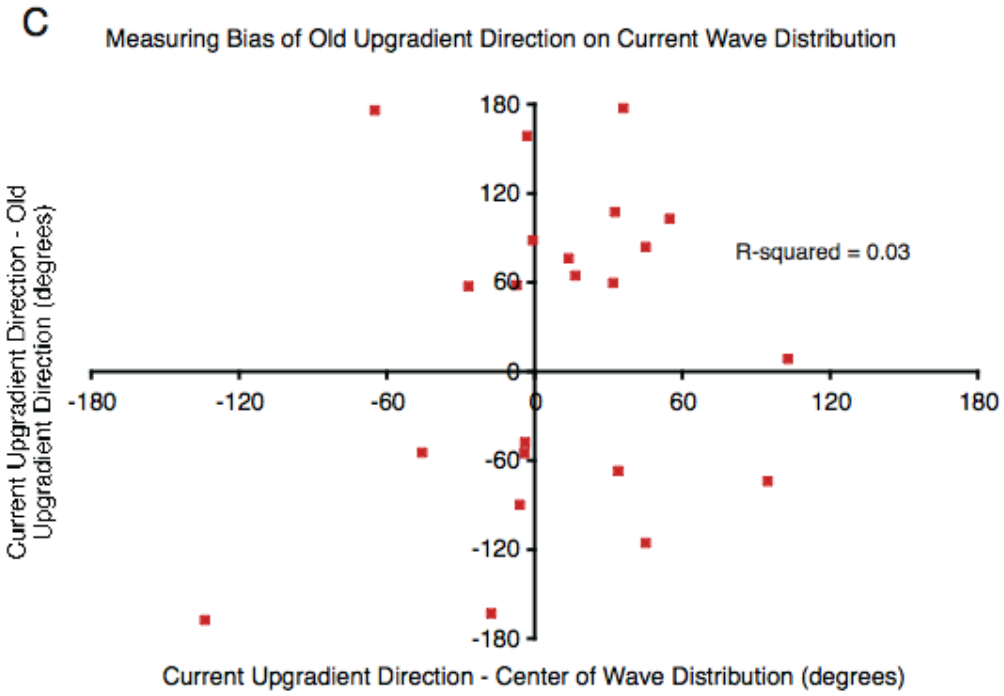

Figure S2. Angle difference and quiescence period do not affect wave distribution, nor are cells skewed toward original micropipette location. (A) Movies from Fig. 2 were sorted according to angle differences between old and new micropipette positions. Dot plot shows no statistical significance ($p = 0.28$, Student's t-test) between mean sector widths (red line). (B) Movies from Fig. 2 were sorted according to the duration between agonist applications (quiescence period). The average quiescence period was 85 s. Dot plot shows no statistical significance ($p = 0.46$, Student's t-test) between mean sector widths (red line). (C) There was no correlation between the old micropipette location on the center of the wave distribution relative and the new micropipette location (R-squared = 0.03).

Supplemental Figure 3

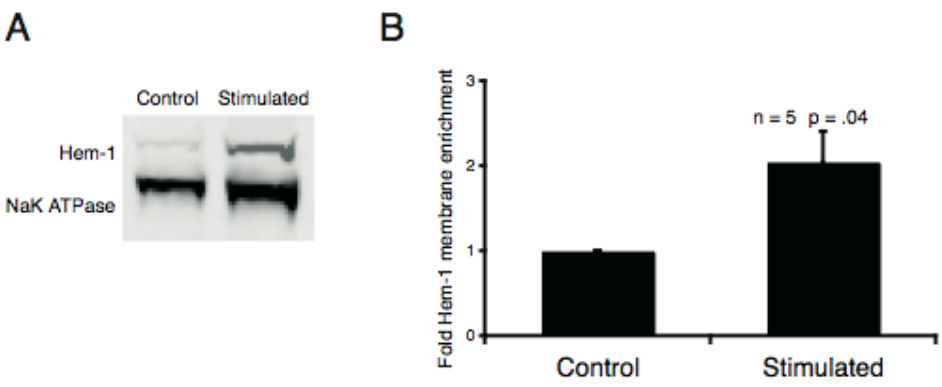

Figure S3. The WAVE complex biochemically fractionates to the plasma membrane upon fMLP stimulation and latrunculin treatment. The WAVE complex normally rapidly fluxes in and out of the TIRF field (with a half-life of 6.4 s), but stably associates in the TIRF field following actin depolymerization by latrunculin treatment {Weiner, 2007 #1}. Cavitation and discontinuous sucrose gradients were used to purify the plasma membrane of unstimulated cells versus stimulated latrunculin-treated cells. (A) Western blot shows Hem-1 and NaK ATPase (a membrane loading control) plasma membrane fractions for both untreated and stimulated (+fMLP, +latB, +GTPγS) cells. (B) Quantification shows a significant ~2-fold enrichment of the WAVE complex at the plasma membrane after stimulation compared to controls cells ($p = 0.04$, one-sample student's t-test) for 5 independent experiments.

CHAPTER THREE

Membrane tension maintains cell polarity by confining signals to the leading edge during neutrophil migration

SUMMARY

Little is known about how neutrophils and other cells establish a single zone of actin assembly during migration. A widespread assumption is that the leading edge prevents formation of additional fronts by generating long-range diffusible inhibitors or by sequestering essential polarity components. We use morphological perturbations, cell severing experiments, and computational simulations to show that diffusive-based mechanisms are not sufficient for long-range inhibition by the pseudopod. Instead, plasma membrane tension could serve as a long-range inhibitor in neutrophils. We find that membrane tension quadruples during leading edge protrusion, and increasing tension is sufficient for long-range inhibition of actin assembly and Rac activation. Furthermore, reducing membrane tension causes actin assembly to be uniformly active. We suggest that tension, rather than diffusible molecules generated or sequestered at the leading edge, is the dominant source of long-range inhibition that constrains the spread of the existing front and prevents the formation of secondary fronts.

INTRODUCTION

The ability of cells to generate polarized distributions of signaling molecules enables numerous biological processes including asymmetric cell division, neurite specification, tissue formation, and cell motility. The Rac GTPase drives actin polymerization and protrusion at the leading edge in a wide range of migrating cells (Ridley et al., 1992; Sun et al., 2004). Efficient migration requires confining Rac activity to the leading edge: spatially uniform Rac activation abolishes movement (Allen et al., 1998; Inoue and Meyer, 2008; Srinivasan et al., 2003).

In neutrophils, Rac activity is highly polarized both in response to external gradients and in the presence of uniform chemoattractant (Gardiner et al., 2002; Weiner et al., 2007). Linked positive and negative feedback loops are thought to enable many cell types to polarize during chemotaxis or random migration (Jilkine and Edelstein-Keshet, 2011; Meinhardt, 1999; Neilson et al., 2011; Turing, 1952; Xiong et al., 2010). Positive feedback amplifies small, transient fluctuations into large, temporally persistent asymmetries. GTPase and/or phosphoinositide-based positive feedback loops have been implicated in the polarization of neutrophils (Inoue and Meyer, 2008; Weiner et al., 2002; Weiner et al., 2006), neurons (Fivaz et al., 2008), *Dictyostelium* (Sasaki et al., 2004), and budding yeast (Butty et al., 2002; Wedlich-Soldner et al., 2003). Positive feedback loops require a balancing mechanism of inhibition to prevent them from overtaking the entire cell. The positive feedback reaction can limit itself by generating long-range inhibition that constrains the spread of the existing front and prevents the formation of secondary fronts. The inhibition is thought to arise either from the production of rapidly diffusing inhibitory molecules by the front (Figure 1A) or from the sequestration of limiting polarity components by the front (Figure 1B). These mechanisms of long-range inhibition depend on rapid diffusion of signaling components through the cytosol. In contrast to the components that participate in the positive

feedback loops at the leading edge, the molecules responsible for long-range inhibition are largely unknown. It has not even been experimentally determined whether this inhibition is a diffusion-based process.

Signaling-centered positive and negative feedback loops are not the only potential mechanisms of polarization. A model consisting entirely of mechanical interactions between the actin cytoskeleton, myosin, and plasma membrane accurately predicts the polarized morphologies of keratocytes (Kozlov and Mogilner, 2007) as well as the relation between cell shape and speed (Keren et al., 2008) without considering upstream signals. This model is insufficient to explain neutrophil polarity because cytoskeletal polarization and migration absolutely require Rac to be polarized (Inoue and Meyer, 2008; Srinivasan et al., 2003). Thus, for force to play a dominant role in neutrophil polarity, it must participate in the spatial patterning of signaling cascades, for example by acting as a long-range inhibitor of Rac activation (Figure 1C).

A significant challenge in discriminating between the many classes of models for cell polarity is that many of the underlying positive and negative feedback components have not been identified, and even for the known components, the key biophysical parameters are unknown. We performed experiments that discriminate between models of long-range inhibition without requiring detailed knowledge of the underlying molecular components. We used morphological perturbations and cell severing to push neutrophils into situations where existing diffusion-based long-range inhibition models break down, as verified by computational simulations. Mechanical tension is one mode of long-range inhibition that could explain our observations on stretched and severed cells. Consistent with this hypothesis, we find that membrane tension nearly quadruples during leading edge protrusion, tension increases suffice for long-range inhibition of Rac activation, and reducing membrane tension activates Rac throughout the cell. Our data suggest that long-range inhibition is not solely based on diffusible molecules generated

or sequestered at the leading edge (as has been widely assumed) but rather requires protrusion-based increases in plasma membrane tension to constrain the spread of the existing front and prevent the formation of secondary fronts.

RESULTS

Distinguishing between neutrophil polarity mechanisms with cell stretching and severing

We sought to distinguish between long-range inhibition mechanisms without requiring a detailed knowledge of the molecular players involved in the process. Due to their widely proposed roles in developmental patterning (Gierer and Meinhardt, 1972; Nakamura et al., 2006; Sick et al., 2006; Turing, 1952), diffusion-based systems are the most popular of the numerous hypothetical inhibition mechanisms in polarizing cells (Jilkine and Edelstein-Keshet, 2011). These usually involve a positive feedback reaction that either produces inhibitory molecules (Figure 1A) or depletes essential polarity components (Figure 1B). Importantly, to generate cell polarity, the inhibitory molecules or limiting components must diffuse more rapidly than the products of the positive feedback reactions. These models were typically developed for cells with spherical morphologies or assumed a 1D spatial geometry to denote the “front-back” axis. To test whether existing mathematical models are consistent with cell behavior, we devised novel experimental settings in which cellular morphologies attenuate diffusion.

If long-range inhibition solely depends on diffusion, then we can interfere with it by creating a thin neck between the pseudopod and the rest of the cell. In contrast, tension-based inhibition should still function in this context. Following brief heat shock in the presence of uniform chemoattractant, neutrophils adopt a stretched growth-cone like morphology (Malawista and De Boisfleury Chevance, 1982); (Figure 2A). Despite this altered morphology, a single zone of actin assembly (tethered pseudopod) is observed

with the cell body remaining inactive in 91% of these cells during the 250 second period of observation (N = 31, Figure 2B, Movie S1). The inactivity of the cell body is remarkable given that it is only connected to the pseudopod through a long, thin tether that is typically one micron in diameter and 25 microns long.

We simulated how three classes of diffusion based polarity models responded in a tethered morphology: Turing (Otsuji et al., 2007), wave pinning (Mori et al., 2008), and neutral drift (Altschuler et al., 2008). These models are conceptual, rolling many as-yet poorly characterized details of the polarity network into generic mechanisms of interaction and feedback. They share several common properties, namely: the total amount of molecules are assumed to be constant during the observed duration of polarization; molecules transition between two states, either at the membrane (active) or cytosol (inactive); and diffusion on the membrane is much slower than in the cytosol. In our simulations, recruitment of molecules to the membrane is autocatalytic and ultimately constrained by depletion of the cytoplasmic species. All three models predict that the cell body will remain inactive despite the tethered morphology (Figure 2C, left panels; Supplemental Figure 1). This could either reflect ongoing long-range inhibition of the cell body by the pseudopod or could be a consequence of depletion that occurred prior to tether formation and persisted indefinitely due to the lack of resynthesis of limiting components. To distinguish between these possibilities, we analyzed the behavior of the models when the cell body is severed from the pseudopod (Figure 2C, right panels; Supplemental Figure 1). All three models predict that the cell body remains inactive despite being disconnected from the pseudopod. Thus the inactivity of the cell body is not due to ongoing inhibition from the pseudopod. If it were, the cell body would have reanimated upon pseudopod removal.

All of the long-range inhibition mechanisms under consideration make strong predictions about the behavior of the cell body after it is severed from the pseudopod (Figure 3A). Diffusion-based competition for a fixed pool of molecules (limiting component) predicts that the cell body will remain inactive after pseudopod removal unless the limiting component is rapidly resynthesized. Similarly, if diffusible inhibitory molecules are responsible for long-range inhibition, then the cell body will also remain inactive unless the inhibitory molecules have a short lifetime. Both diffusion-based inhibition mechanisms predict that the cell body will remain inactive after severing unless the resynthesis/turnover rate is very high. In contrast a tension-based inhibition mechanism would allow the cell body to reanimate because severing would allow the cell to relax into a tension-free morphology. Thus, severing experiments discriminate between current long-range inhibition mechanisms.

The tethered morphology enabled us to cut the tether with a focused laser beam without destroying either the cell body or the pseudopod. We find that the cell body becomes highly protrusive within 70 seconds of pseudopod removal in 47% of the cells (N = 36, Figure 3B, Supplemental Figure S1, and Movie S2). Two sets of controls demonstrate that the reanimation of the cell body is not due to laser-induced generation of chemoattractant. Using cells containing a sensitive readout of actin assembly (SCAR/WAVE complex recruitment, Weiner et al., 2007), we observed activation of adjacent cells upon cell destruction with lasers but no detectable response following tether severing (Supplemental Figure S2). We also studied spontaneous cleavage of tethers, which occurs at a low frequency in the absence of laser cutting. Similar to laser-based severing, spontaneous cleavage of the tether also resulted in reanimation of the cell body within one minute of severing in 26% of the cells (N = 64, Figure 3C, Movie S2). Rapid reanimation of the cell body after severing is inconsistent with an inhibition mechanism involving slowly resynthesized limiting components. Our experiments

suggest that the pseudopod continuously inhibits the cell body either by sequestering rapidly synthesized limiting components, producing short-lived diffusible inhibitory molecules, or generating mechanical tension.

Tethered morphologies dramatically attenuate diffusion-based exchange between pseudopod and cell body

We reasoned that the presence of the tether should severely attenuate diffusion-based communication between the pseudopod and cell body. We experimentally determined the mixing rate between the pseudopod and the cell body using FRAP (Figure 4). We first measured the rate of recovery following GFP photobleaching in the cell body of tethered cells (Figure 4B, Movie S3). To control for reversible bleaching and new GFP synthesis, we also performed photobleaching experiments in cells that lacked a tethered pseudopod (Supplemental Figure S3). We subtracted the recovery rate due to reversible bleaching from the overall recovery rate for tethered cells to determine the amount of recovery that was due to diffusion of GFP from the pseudopod through the tether (Figure 4B and Supplemental Figure S3). Our data demonstrate that the tethered morphology slows down the exchange of GFP between pseudopod and cell body by approximately 840-fold (N = 25, Figure 4C) compared to untethered cells. The experimentally determined mixing rates correlate very well with our computationally predicted mixing rates for measured cell tether lengths and diameters (Figure 4D; Supplemental Information).

We investigated whether inclusion of synthesis and degradation of the limiting component could enable this mechanism to replicate our experimental observations in tethered and severed cells. We chose to analyze the limiting component in the context of the neutral drift model because it is the most analytically tractable. For the cell body to reanimate within 35 seconds of severing, the limiting component must be resynthesized

at a rate of at least 6 particles / sec (Supplemental Information). For the cell body to remain quiescent in the tethered state in the absence of severing, resynthesis must be balanced by loss through the tether. Since the tethered morphology dramatically reduces the rate at which molecules diffuse from the cell body to the pseudopod, the limiting component would require a diffusion coefficient of 330 μm^2/sec to maintain quiescence of the cell body (Supplemental Information). This diffusion rate is an order of magnitude larger than those reported for cytosolic proteins (Swaminathan et al., 1997) and approximately two-fold greater than that for metabolites in cytoplasm (Garcia-Perez et al., 1999). Similar constraints make a diffusible inhibitor emanating from the cell body unlikely, because the inhibitor requires a short lifetime to enable rapid reanimation from the cell body following severing, but such a short-lived inhibitor cannot survive the slow journey through the tether to prevent cell body activity in the tethered morphology.

In summary, the reanimation of the cell body after severing demonstrates that the pseudopod actively inhibits protrusions elsewhere. However, our FRAP experiments on tethered cells indicate that diffusion is too highly attenuated for efficient diffusion-based long-range inhibition. Even with resynthesis, the neutral drift model requires the limiting component to diffuse at a rate that is over an order of magnitude larger than cytoplasmic proteins. In fact, the necessary diffusion coefficient is comparable to that of water itself. Our data are inconsistent with long-range inhibition mechanisms based solely on passive diffusion. The leading edge must inhibit activation of the cell body through more rapid modes of communication such as active transport, propagating waves, or mechanical forces.

Membrane tension increases during cellular protrusion

Because mechanical propagation of information (such as tension) and diffusion-based communication do not share the same geometrical limitations, we hypothesized

that pseudopod protrusion could generate tension in the plasma membrane that rapidly propagates to inhibit protrusive activity in the rest of the cell. This hypothesis requires tension to increase during polarization. Consistent with this hypothesis, aspiration experiments on suspended neutrophils have shown that the cellular cortical tension increases during polarization (Zhelev et al., 1996). However, it is unknown whether the cortical tension represents tension in the cytoskeleton, plasma membrane, or both (Hochmuth, 2000). We used optical traps (Dai and Sheetz, 1999) to measure plasma membrane tension during chemoattractant-stimulated polarization (Figure 5, Movie S4).

Addition of chemoattractant caused a significant increase in cell protrusion accompanied by a significant increase in membrane tension (N=8, Figure 5B, C, p=0.0006, Movie S4). On average, the pulling force nearly doubled (from 8.5 to 16.6pN) during protrusion (Figure 5D) in a manner that closely correlated with cell spreading (Figure 5B, inset). We suggest that cellular protrusion is responsible for the significant (roughly four-fold) increase in plasma membrane tension. The pulling force was not a response to the mechanical forces associated with fluid exchange (N=8, Figure 5C). Pretreatment with blebbistatin, which causes a highly elongated morphology, also causes basal membrane tension to increase (Supplemental Figure S4).

Cellular deformation induces long-range inhibition of protrusion signals

If tension is a long-range inhibitor of protrusion and signaling, then increases in cell tension (even when they are not a result of pseudopod generation) should inhibit protrusion and leading edge signals throughout the cell. To test this hypothesis, we used micropipette aspiration to mimic the mechanical increases in tension that accompany protrusion (Herant et al., 2005). This perturbation likely increases tension in both the cytoskeleton and plasma membrane when performed on migrating neutrophils. We assayed the effects of tension increases on cell morphology as well as leading edge

signals using TIRF-based imaging readouts of Rac activity and SCAR/WAVE complex recruitment. Rac and the SCAR/WAVE complex localize to the leading edge of neutrophils and are essential for actin assembly in these cells (Sun et al., 2004; Weiner et al., 2006).

We brought a micropipette into contact with the cell surface and applied suction to cause the cell to bulge into the micropipette, thereby increasing cell tension (Figure 6A). Within seconds, this mechanical deformation inhibited leading edge protrusion. Following aspiration, the pseudopod retracts into the cell body, leading to a significant reduction in spread area (Figure 6B, Movie S5). Aspiration also inhibited SCAR/WAVE complex recruitment (Figure 6C, Movie S5) and Rac activation (Figure 6D, Movie S5).

Aspiration-induced inhibition of protrusion and leading edge signals was reversible (Figure 6B,D late time points, Movie S5). Thus, inhibition was not due to trivial reasons such as irreversible cell damage following aspiration. We also monitored plasma membrane integrity during aspiration with cytoplasmic dyes. We did not detect leakage of cytosolic GFP or the entrance of extracellular rhodamine phalloidin, indicating that our aspirations leave the plasma membrane intact (Supplemental Figure S5). Thus, mechanical tension suffices to act as a long-range inhibitor of protrusion and leading edge signals in migrating neutrophils.

Membrane tension restricts signals to the front of migrating neutrophils

Our aspiration data show that tension increases are sufficient for long-range inhibition of protrusion, but two important questions remain. First, does the cell require tension to spatially confine signals to the front? Second, which structures transmit the inhibitory tension: cytoskeleton, plasma membrane or both? To answer these questions we monitored leading edge signaling while reducing membrane tension with hypertonic buffers (Keren, 2011) or cytoskeletal tension with myosin inhibition (Lee et al., 2011;

Pasternak et al., 1989). Neutrophils treated with the actin inhibitor blebbistatin causes cytoskeletal tension to decrease (Lee et al., 2011) but plasma membrane tension to increase (Supplemental Figure 4). Blebbistatin treatment caused an immediate tail retraction defect and cell elongation but did not cause an expansion of signals beyond the leading edge (Figure 7A,C). Elongation often led to reduced SCAR/WAVE complex recruitment at later time points (Figure 7A,C), possibly because of increased membrane tension. After several minutes of blebbistatin treatment, the cells often developed a stellate morphology with multiple arm-like projections that appeared to be leading edges. However, close inspection revealed that only one of these projections actively protrudes at a time (Supplemental Figure S6); the others are inanimate husks of previous leading edges that were not retracted after they died. The addition of hypertonic buffer (150mM sucrose) to blebbistatin-treated cells caused an immediate and spatially uniform accumulation of SCAR/WAVE complex at the plasma membrane and resulted in a loss of cell polarity (Figure 7B,C), whereas hypotonic buffer resulted in cell rounding and a disappearance of SCAR/WAVE complex recruitment (Figure S6). Hypertonic buffer in the absence of blebbistatin also caused SCAR/WAVE complex accumulation although the effect was smaller (Figure 7C; Supplemental Figure S6). At later time points, neutrophils in hypertonic buffer often spread uniformly with wider leading edges, and multiple pseudopodia for long periods of time (Supplemental Figure S6). These behaviors are consistent with ectopic leading edge signaling throughout the cell. Based on the significant expansion of SCAR/WAVE complex recruitment in cells treated with hypertonic buffer but minimal effect of blebbistatin alone, we conclude that membrane tension plays the more dominant role in restricting signals to the leading edge.

DISCUSSION

We used microdissection and perturbations of cell morphology to push neutrophils into regimes where existing diffusion-based polarity models break down. Our results support a polarity mechanism in which membrane tension provides a long-range inhibitory signal that restricts signals to the leading edge. In contrast to diffusion-based inhibition, tension can effectively propagate through the cell even when the cellular cross-section is small. This ability could be physiologically important as leukocytes frequently have small cross-sections as they crawl through tight spaces *in vivo*, for example during transendothelial migration (Peters et al., 2008).

We suggest that tension acts as a long-range inhibitor in the following manner. First, pseudopod protrusion increases tension in the plasma membrane (as we observe with our optical trap measurements in Figure 5). This tension rapidly propagates throughout the cell to act as a long-range inhibitor of leading edge formation. In support of this hypothesis, increases in tension suffice for long-range inhibition of Rac activation and protrusion (Figure 6), and decreases in tension expand leading edge activities (Figure 7). During cell polarization, tension only becomes significant after the front has formed, by which point positive feedback enables the existing front to maintain itself. Furthermore, since the front is the source of tension, any fluctuations in front size are immediately balanced by compensatory changes in tension levels. The observation that tension spatially restricts signals such as Rac to the leading edge differentiates our model from purely mechanical (signaling-independent) models of polarity.

For tension to be an effective long-range inhibitor, it must remain high for the entire duration of neutrophil migration. If remodeling of the membrane (due to exocytosis) dissipates tension over time, then the inhibition should decay and polarization would eventually fail. Importantly, others have shown that neutrophil membrane tension remains high long after stimulation (Shao and Xu, 2002) and that

persistent deformations cause persistent increases in membrane tension (Herant et al., 2005). Resting neutrophils, like many immune cells, have numerous small wrinkles in their plasma membrane which act as a reservoir that doles out plasma membrane as membrane tension increases during cellular deformation (Hallett and Dewitt, 2007; Herant et al., 2005). Because the unfolding of wrinkles is energetically unfavorable yet reversible, membrane tension remains high as the cell tries to restore its wrinkles (Herant et al., 2005). Thus, the membrane can transmit long-range inhibitory tension in the neutrophil as in other highly motile cells like keratocytes (Keren et al., 2008).

Tension could collaborate with diffusion-based systems to guide migration

We have shown that membrane tension restricts protrusion to the leading edge, thereby allowing the neutrophil to polarize and migrate. However, it is likely that other signaling systems align the migration with external cues. Latrunculin-treated cells, which cannot polymerize actin and protrude, can still align internal signals such as PIP_3 with external chemoattractant gradients (Janetopoulos et al., 2004; Servant et al., 2000). Thus, cells can interpret chemical gradients without protrusion-based increases in tension. However, neutrophils require F-actin to polarize leading edge signals such as PIP_3 production in response to uniform chemoattractant (Wang et al., 2002). Furthermore, multiple patches of front signals coexist in latrunculin-treated Dictyostelium cells exposed to multiple sources of chemoattractant, whereas a single patch of activity dominates in untreated cells (Devreotes and Janetopoulos, 2003; Janetopoulos et al., 2004). Thus, while gradient alignment can occur without actin, important parts of the polarity program (polarity in response to uniform chemoattractant, single site of polarity in response to multiple cues) depend on the actin network, possibly reflecting the role of tension. Although diffusion-based inhibitors may be collaborating with tension for polarity in response to uniform chemoattractant, we suggest that tension is the dominant

inhibitor. Tension can operate under conditions where diffusive mechanisms fail (tethered cells), and decreasing tension in (even non-tethered) cells inhibits the restriction of protrusive signals to the leading edge.

Tension antagonizes protrusion in many cell types

Both cytoskeletal and membrane tension are capable of transmitting forces over long range (Dai and Sheetz, 1999; Keren et al., 2008; Mayer et al., 2010) to inhibit cell protrusion. Membrane tension is the loading force which growing actin filaments fight in order to protrude the membrane (Keren et al., 2008). Tension in the cytoskeleton (arising from myosin contraction) can also antagonize actin-based protrusion by pulling actin filaments away from the membrane, thereby reducing the amount of protrusion generated by a given amount of actin assembly (Cai et al., 2010).

In fibroblasts, both cytoskeletal and membrane tension limit cell protrusion. Increasing membrane tension halts spreading while decreasing membrane tension enhances the rate of lamellipodial protrusion and transiently causes uniform spreading (Raucher and Sheetz, 2000). Decreasing cytoskeletal tension (through myosin inhibition) causes faster spreading and a larger final spread area (Cai et al., 2010). Furthermore, increasing tension with biaxial cellular stretching downregulates Rac activity (Katsumi et al., 2002).

For fish keratocytes, membrane tension acts as a long-range coupling mechanism for cell polarization (Keren et al., 2008; Kozlov and Mogilner, 2007). Protrusion in one location promotes retraction in other locations and vice versa due to changes in membrane tension. Actin polymerization in a membrane bag reproduces the wide range of morphologies observed by keratocytes and accurately predicts quantitative relationships between migration speed and morphology without requiring free parameter fitting (Keren et al., 2008). Decreases in cytoskeletal tension (through

the myosin inhibitor blebbistatin) does not destroy keratocyte polarity and only slightly reduces their speed, suggesting that the plasma membrane (not the cytoskeleton) carries the important tension in this system. Although keratocyte motility has been primarily considered as a pure mechanical system (with no need for signaling inputs), a graded distribution of actin assembly is necessary for the existing models of keratocytes motility (Barnhart et al., 2011; Keren et al., 2008). In light of our findings, it will be interesting to examine leading edge signals in keratocytes and determine whether membrane tension restricts them to the front as well.

In *Dictyostelium*, cytoskeletal tension plays an important role in restricting signals to the leading edge. Traction force microscopy experiments have identified large myosin-based cytoskeletal tension increases during *Dictyostelium* migration (Meili et al., 2010). Genetic deletion of Myosin II reduces cytoskeletal tension dramatically (Pasternak et al., 1989) and increases lateral pseudopod production (Wessels et al., 1988) and Ras activation (Lee et al., 2010). These data strongly support a role for cytoskeletal tension in *Dictyostelium* polarity. Whether plasma membrane tension also plays a role in *Dictyostelium* polarity is unknown.

In neutrophils, membrane tension appears to be the dominant inhibitory mechanism for cell polarization. We find that membrane tension increases during neutrophil protrusion and that decreasing membrane tension results in the expansion of leading edge signals and a loss of polarity. In contrast, we find that decreasing cytoskeletal tension with myosin inhibition has no effect on leading edge signals, though myosin inhibition potentiates leading edge signaling increases observed in hypertonic buffer, suggesting that cytoskeletal tension may be partially redundant with membrane tension in restricting leading edge activities.

Possible mechanism of tension sensing

Our experiments suggest that membrane tension acts as a long-range inhibitor of protrusion in migrating neutrophils. How do cells sense and respond to tension? Tension-gated ion channels in the plasma membrane could transduce membrane tension into an inhibitory signal. Another potential mode of tension sensation relies on the properties of the actin nucleation machinery in neutrophils. The Scar/WAVE complex forms multiple propagating waves that organize the neutrophil leading edge (Weiner et al., 2007) and extinguish if mechanical barriers prevent them from protruding. Increases in membrane tension could similarly extinguish waves by antagonizing protrusion. Since the SCAR/WAVE complex is required for Rac activation in neutrophils (Weiner et al., 2006), the destruction of waves by membrane tension also inhibits Rac activation. Because cytoskeletal tension also antagonizes protrusion, it might inhibit signaling via SCAR/WAVE complex dynamics as well. Why don't protrusions at the leading edge extinguish themselves through increases in tension? Perhaps waves at the leading edge preferentially survive because of their high density, which could enhance survival by activating Rac or by creating a strong actin network that can protrude against the load provided by membrane tension, similar to how membrane tension limits protrusion to areas of high actin density in keratocytes (Keren et al., 2008). Tension-based polarization mechanisms appear to operate in a wide range of migratory cells, although though the sources of the tension (protrusion vs. contraction) and structures bearing the tension (membrane vs. cytoskeleton) can vary from one cell type to the next.

EXPERIMENTAL PROCEDURES

Cell culture

HL-60 cells were generated, cultured, and differentiated as described in Weiner et al, 2007. Primary neutrophils were obtained by pinprick as described in Weiner et al, 2006.

Cell severing and FRAP

Tethered cells were generated by brief heat shock as in Malawista and De Boisfleury Chevance, 1982. Cell severing and FRAP was performed with a 435 nm dye cell laser (Manually Controlled Micropoint System, Photonic Instruments).

Cell aspiration

Cell aspiration was performed with a heat-polished microneedle (3 μm diameter) positioned with a Narishige MM-89 micromanipulator with fine hydraulic control. Suction pressure was controlled with a Narishige IM-300 microinjection system.

Microscopy

Brightfield, epifluorescence and TIRF experiments were performed on Nikon TE-2000 and Ti microscopes.

Membrane tension measurements

Membrane tubes were pulled with 2 μm ConA-coated beads positioned by a 1064 nm holographic optical trap. To calculate the tether force, we measured the distance between the bead and the center of the trap (see Supplemental Methods).

Cytoskeletal and membrane tension perturbations

For hypertonic treatment experiments, we added an equal volume of hypertonic buffer (buffer + 300 mM sucrose). To inhibit myosin, we added blebbistatin to 66 μM final concentration. For combined treatment we pretreated with blebbistatin for 10 minutes prior to adding hypertonic buffer. For hypotonic treatment experiments, we added an equal volume of hypotonic buffer (H_2O + 1 mM $MgCl_2$ + 1.2 mM $CaCl_2$).

Computational simulations

Described in Supplemental Methods.

FIGURE LEGENDS

Figure 1: Conceptual mechanisms for long-range inhibition

A) *Diffusible Inhibitor.* An autocatalytic activator (A, green) produces an inhibitory molecule (I, red) that diffuses throughout the cytoplasm to act as a long-range inhibitor of leading edge formation.

B) *Limiting Component.* An autocatalytic activator in the front inhibits activation elsewhere by consuming essential substrates (S, gold) of the positive feedback loop, rather than generating a diffusible inhibitor (as in (A)).

C) *Mechanical Tension.* Protrusion at the leading edge generates mechanical tension (T, depicted as red springs) in either the plasma membrane or the underlying cytoskeleton. This tension acts as a long-range inhibitor of protrusion.

Figure 2: Maintenance of polarity in tethered cells

A) *Tether formation in heat-treated HL-60 cells.* The cell initially forms a pseudopod (black arrowhead). The pseudopod crawls away from the fixed cell body, causing a tether (white arrowhead) to form between them. The scale bar is 5 microns.

B) *Maintenance of polarity in tethered HL-60 cells. Left:* The cell body (black arrow) remains completely fixed as the pseudopod (black arrowhead) migrates a significant distance. The asterisk in the first frame denotes a neighboring cell that lacks a tether. *Right:* cell outlines from successive time points are depicted in blue, green, orange, and red, respectively. The morphology of the cell body stays constant over the 250 second observation time in 91% of the uncut cells (N = 27). The scale bar is 5 microns.

C) *Simulation of published diffusion-based inhibition models following cell stretching and severing.* The *top*, *middle* and *bottom* panels depict simulation results of a wave pinning model (*top*), Turing model (*middle*), and neutral drift model (*bottom*) following cell stretching or severing. The concentration of the activator species (u) is represented as grayscale with black being highest concentration. In the *left* panels, spherical or cylindrical cells were allowed to develop polarized signals. We then simulated the subsequent time evolution of this polarized signaling distribution in cells that were stretched into dumb-bell geometries, similar to our experimental tethers (Figure 2). In the *right* panels, the signals in our spherical or cylindrical cells were polarized as before. We then simulated the time evolution of the signals in cells that were severed into two equal halves. Steady state distributions of membrane-bound activators for all three models are shown.

Figure 3: Cells generate a new pseudopod after severing

A) *Outline of severing experiments.* Following cell polarization, the pseudopod is removed, and the behavior of the cell body is observed. If the pseudopod had sequestered a non-regenerating limiting component required for polarization, the cell body should not have the material to reanimate. Reanimation of the cell body following severing of the pseudopod would be consistent with short-lived inhibitor generated at the leading edge. This short-lived inhibitor could be due to mechanical tension, a rapidly synthesized limiting component, or a diffusible inhibitor with a short half-life.

B) *Pseudopod production after laser severing.* DIC images showing a tethered HL-60 that is severed with a laser beam just before 0 seconds. Following severing, the previously quiescent cell body responds by making a new pseudopod (white arrowhead). The cell body makes a pseudopod after severing in 47% of cells (N = 36). The scale bar is 2.5 microns.

C*) Pseudopod production after spontaneous tether cleavage.* Phase images of a cell whose pseudopod (black arrowhead) spontaneously breaks free from the cell body (black arrow) at 0 seconds. The cell body makes a new pseudopod within 50 seconds of severing (white arrowhead) and begins to migrate. The asterisks denote neighboring cells. There is significant reanimation of the cell body following spontaneous tether cleavage in 26% of cells (N = 62). The scale bar is 10 microns.

Figure 4: The tethered morphology dramatically attenuates diffusion.

A) *Outline of FRAP (Fluorescence Recovery After Photobleaching) experiment*. A GFP-expressing HL-60 cell is heated to generate a tethered pseudopod. The GFP signal in the cell body is then bleached, and the recovery in the cell body is measured to monitor diffusion-based mixing through the tether. Retraction of the pseudopod causes the contents of the cell body and the pseudopod to mix completely.

B) *Typical FRAP profile for a tethered cell.* The graph shows the normalized fluorescence recovery due to diffusion over time for the cell whose GFP fluorescence is shown in the inset images (with cell outlines in yellow). There is slow linear recovery until 160 sec, at which point the tethered pseudopod retracts and the GFP from the pseudopod rapidly mixes with the cell body.

C) *Overlaid FRAP profiles for tethered cells.* The measured fluorescence recoveries for all of the tethered cells during the first second after bleaching are overlaid in red. The expected initial fluorescence recovery for a non-tethered spherical cell (mixing rate constant = 1.2/sec) is shown in blue.

D) *Predicted vs. measured mixing rates between pseudopod and cell body for tethered cells.* Each black dot represents the diffusion-based mixing rate constant for an individual photobleached cell. The y coordinate for each cell is the experimentally measured mixing rate constant ($D_{mix,\ obs}$). The x coordinate for each cell is the predicted mixing rate constant using the formula:

$\frac{D_{mix,pred}}{D_{GFP}} = \frac{V_{tether}}{L^2 V_{cell}}$; where $D_{mix,pred}$ is the predicted mixing rate constant; D_{GFP} is the known diffusion coefficient of GFP in cytoplasm (27μm^2/s, (Swaminathan et al., 1997)); L is the tether length; and V_{cell} and V_{tether} are the volumes of the cell and the tether, respectively. The values L, V_{cell} and V_{tether} were measured for each cell from brightfield images. The predicted mixing rates correlate with the measured values (R^2 = 0.8, N=24, red line is y = x). The tethered geometry reduces mixing rate by 134 - 4472 fold for all of the cells in the experiment.

Figure 5: Membrane tension increases during protrusion

A) *Schematic outline of membrane tension measurement experiments*. The tension in the plasma membrane can be measured by pulling a thin tube of membrane from the cell surface with an adhesive polystyrene bead in an optical trap. Increases in membrane tension result in higher pulling forces on the bead. We hypothesized that cell spreading, induced by uniform fMLP addition, should cause the membrane tension to increase. As a control, we flow in buffer, which does not induce spreading and should not increase membrane tension.

B) *Pulling force over time for a representative cell*. For primary human neutrophils, the tube was first pulled to a length of ~2 microns (pull 1, arrow, light green bar) and held there briefly (hold 1, light blue bar). The tube was then extended to a length of ~10 microns (pull 2, arrow, dark green bar) and held there (hold 2, dark blue bar) before fMLP (arrow) was flowed in. The colored bars denote the time period over which the forces were averaged for the graph in D; these regions were selected to avoid sudden force jumps. Addition of fMLP caused the cell to spread and the pulling force to increase

dramatically (red bar). The ***inset*** graph shows the increase in spread area (green) and the increase in tether force (blue), both of which were normalized to the total area or force increase that occurred during the response. Brightfield images of the cell, with the outline superimposed in yellow, are shown below. The tether position, determined with a fluorescent membrane dye (DiI), is also superimposed in yellow.

C) *Pulling force over time for individual cells following buffer addition or fMLP stimulation*. The left panel shows the force traces of tubes held at constant length as buffer is flowed through the chamber to control for the effects of flow on the force measurements. The right panel shows the force traces of tubes held at constant length as the cells were stimulated by flowing fMLP through the chamber. In both panels, flow begins at the beginning of each trace.

D) *Pulling force at different stages of the experiment*. The graph shows the forces at different times during the experiment (denoted by the colored bars in B) for the eight fMLP-stimulated cells depicted in C. Each black dot represents the force measurement of an individual cell. The large and small maroon bars indicate mean force values and standard errors, respectively. After fMLP addition, the cell spreads and the force increases dramatically ($p = 0.0006$) and briefly plateaus (post-spread, red bar in B) before the tube detaches from the bead.

Figure 6: Artificially increasing tension with aspiration reversibly inhibits leading edge protrusion and signaling

A) *Outline of experiment.* Schematic showing the predicted results of aspiration experiments for a long-range inhibitor based on cell tension. The deformation of the cell due to aspiration increases tension, which would be predicted to inhibit protrusion and reduce SCAR/WAVE complex recruitment.

B) *Aspiration induces pseudopod retraction*. Aspiration of the trailing edge acts as a long-range inhibitor of protrusion. *Left:* a graph of the spread area over time during aspiration. The spread area decreases dramatically upon aspiration and then eventually rebounds after release. Tick marks indicate bright field frames shown at right. *Right:* brightfield images of the same cell. The tip of aspirated cytoplasm is shown with a black arrowhead. The pseudopod (white arrowhead) dies and retracts shortly after aspiration. When the aspirated cytoplasm is released, a new pseudopod forms with a delay of about 100 seconds.

C) *Aspiration inhibits SCAR/WAVE complex recruitment. Top:* A crawling neutrophil expressing the SCAR/WAVE complex reporter Hem-1-YFP is shown before *(-15s and 0s)* and during micropipette aspiration. The black arrowhead in the brightfield image denotes the portion of the cell aspirated into the pipette. Increasing tension via aspiration inhibits SCAR/WAVE complex recruitment throughout the cell. *Bottom:* Quantitation of Hem-1-YFP recruitment during aspiration experiments (N = 10); aspiration begins at frame seven (arrow).

D) *Aspiration inhibits Rac activity.* A crawling neutrophil expressing the Rac activation reporter PAK-PBD-YFP is shown. The fluorescence channel shows PAK-PBD-YFP visualized in TIRF mode. Each brightfield frame shows the portion of the cell aspirated into the pipette for the current (black arrowhead) and previous (white arrowhead) frames. Aspiration-mediated increases in cell tension result in a dramatic decrease in Rac activation in 85% of cells (N =27). Rac activation returns upon the release of aspiration pressure 65% of the time.

Figure 7: Membrane tension reduction causes expansion of signaling

A) *Blebbistatin treatment causes cellular elongation but no enhancement of leading edge signaling. Top:* A crawling neutrophil expressing the SCAR/WAVE complex reporter Hem-1-YFP (visualized in TIRF mode, shown as a heat map) is shown before (*-15s*) and during (*5s*, *25s*, *55s*) application of blebbistatin, which reduces cytoskeletal tension but increases membrane tension. The cells become elongated but SCAR/WAVE complex recruitment does not expand beyond the leading edge. SCAR/WAVE complex recruitment decreases at later time points, likely due to elongation-induced increases in membrane tension. *Bottom:* Brightfield images of the same cell to visualize morphology.

B) *Combination of hypertonic buffer and blebbistatin causes uniform SCAR/WAVE complex recruitment*. *Top:* A blebbistatin-treated (100μM) neutrophil expressing the SCAR/WAVE complex reporter Hem-1-YFP (visualized in TIRF mode, shown as a heat map) is shown before (*-20s* and *-10s*) and during (*5s* and *15s*) application of hypertonic buffer (150mM sucrose + 100μM blebbistatin), which reduces membrane tension. Reduction in membrane tension causes SCAR/WAVE complex recruitment throughout the cell. *Bottom:* Brightfield images of the same cell to visualize morphology. Note the uniform spreading between the *15s* and *475s* time points.

C) *Quantification of tension reduction effects on signaling*. Quantitation of Hem-1-YFP recruitment during treatment with either hypertonic buffer + blebbistatin (red, N=24), hypertonic buffer alone (blue, N=28), or blebbistatin alone (green, N=12). The number of pixels containing Hem-1 signal were quantified at each time point (see Methods and Materials) and normalized to the pre-treatment signal.

REFERENCES

Allen, W.E., Zicha, D., Ridley, A.J., and Jones, G.E. (1998). A role for Cdc42 in macrophage chemotaxis. J Cell Biol *141*, 1147-1157.

Altschuler, S.J., Angenent, S.B., Wang, Y., and Wu, L.F. (2008). On the spontaneous emergence of cell polarity. Nature *454*, 886-889.

Barnhart, E.L., Lee, K.C., Keren, K., Mogilner, A., and Theriot, J.A. (2011). An adhesion-dependent switch between mechanisms that determine motile cell shape. PLoS Biol *9*, e1001059.

Butty, A.C., Perrinjaquet, N., Petit, A., Jaquenoud, M., Segall, J.E., Hofmann, K., Zwahlen, C., and Peter, M. (2002). A positive feedback loop stabilizes the guanine-nucleotide exchange factor Cdc24 at sites of polarization. Embo J *21*, 1565-1576.

Cai, Y., Rossier, O., Gauthier, N.C., Biais, N., Fardin, M.A., Zhang, X., Miller, L.W., Ladoux, B., Cornish, V.W., and Sheetz, M.P. (2010). Cytoskeletal coherence requires myosin-IIA contractility. J Cell Sci *123*, 413-423.

Dai, J., and Sheetz, M.P. (1999). Membrane tether formation from blebbing cells. Biophys J *77*, 3363-3370.

Fivaz, M., Bandara, S., Inoue, T., and Meyer, T. (2008). Robust neuronal symmetry breaking by Ras-triggered local positive feedback. Curr Biol *18*, 44-50.

Garcia-Perez, A.I., Lopez-Beltran, E.A., Kluner, P., Luque, J., Ballesteros, P., and Cerdan, S. (1999). Molecular crowding and viscosity as determinants of translational diffusion of metabolites in subcellular organelles. Arch Biochem Biophys *362*, 329-338.

Gardiner, E.M., Pestonjamasp, K.N., Bohl, B.P., Chamberlain, C., Hahn, K.M., and Bokoch, G.M. (2002). Spatial and temporal analysis of Rac activation during live neutrophil chemotaxis. Curr Biol *12*, 2029-2034.

Gierer, A., and Meinhardt, H. (1972). A theory of biological pattern formation. Kybernetik *12*, 30-39.

Herant, M., Heinrich, V., and Dembo, M. (2005). Mechanics of neutrophil phagocytosis: behavior of the cortical tension. J Cell Sci *118*, 1789-1797.

Hochmuth, R.M. (2000). Micropipette aspiration of living cells. J Biomech *33*, 15-22.

Inoue, T., and Meyer, T. (2008). Synthetic activation of endogenous PI3K and Rac identifies an AND-gate switch for cell polarization and migration. PLoS One *3*, e3068.

Jilkine, A., and Edelstein-Keshet, L. (2011). A comparison of mathematical models for polarization of single eukaryotic cells in response to guided cues. PLoS Comput Biol *7*, e1001121.

Keren, K. (2011). Cell motility: the integrating role of the plasma membrane. Eur Biophys J *40*, 1013-1027.

Keren, K., Pincus, Z., Allen, G.M., Barnhart, E.L., Marriott, G., Mogilner, A., and Theriot, J.A. (2008). Mechanism of shape determination in motile cells. Nature *453*, 475-480.

Kozlov, M.M., and Mogilner, A. (2007). Model of polarization and bistability of cell fragments. Biophys J *93*, 3811-3819.

Lee, C.Y., Herant, M., and Heinrich, V. (2011). Target-specific mechanics of phagocytosis: protrusive neutrophil response to zymosan differs from the uptake of antibody-tagged pathogens. J Cell Sci *124*, 1106-1114.

Lee, S., Shen, Z., Robinson, D.N., Briggs, S., and Firtel, R.A. (2010). Involvement of the cytoskeleton in controlling leading-edge function during chemotaxis. Mol Biol Cell *21*, 1810-1824.

Malawista, S.E., and De Boisfleury Chevance, A. (1982). The cytokineplast: purified, stable, and functional motile machinery from human blood polymorphonuclear leukocytes. J Cell Biol *95*, 960-973.

Mayer, M., Depken, M., Bois, J.S., Julicher, F., and Grill, S.W. (2010). Anisotropies in cortical tension reveal the physical basis of polarizing cortical flows. Nature *467*, 617-621.
Meinhardt, H. (1999). Orientation of chemotactic cells and growth cones: models and mechanisms. J Cell Sci *112 (Pt 17)*, 2867-2874.
Mori, Y., Jilkine, A., and Edelstein-Keshet, L. (2008). Wave-pinning and cell polarity from a bistable reaction-diffusion system. Biophys J *94*, 3684-3697.
Nakamura, T., Mine, N., Nakaguchi, E., Mochizuki, A., Yamamoto, M., Yashiro, K., Meno, C., and Hamada, H. (2006). Generation of robust left-right asymmetry in the mouse embryo requires a self-enhancement and lateral-inhibition system. Dev Cell *11*, 495-504.
Neilson, M.P., Veltman, D.M., van Haastert, P.J., Webb, S.D., Mackenzie, J.A., and Insall, R.H. (2011). Chemotaxis: a feedback-based computational model robustly predicts multiple aspects of real cell behaviour. PLoS Biol *9*, e1000618.
Otsuji, M., Ishihara, S., Co, C., Kaibuchi, K., Mochizuki, A., and Kuroda, S. (2007). A mass conserved reaction-diffusion system captures properties of cell polarity. PLoS Comput Biol *3*, e108.
Pasternak, C., Spudich, J.A., and Elson, E.L. (1989). Capping of surface receptors and concomitant cortical tension are generated by conventional myosin. Nature *341*, 549-551.
Raucher, D., and Sheetz, M.P. (2000). Cell spreading and lamellipodial extension rate is regulated by membrane tension. J Cell Biol *148*, 127-136.
Ridley, A.J., Paterson, H.F., Johnston, C.L., Diekmann, D., and Hall, A. (1992). The small GTP-binding protein rac regulates growth factor-induced membrane ruffling. Cell *70*, 401-410.
Sasaki, A.T., Chun, C., Takeda, K., and Firtel, R.A. (2004). Localized Ras signaling at the leading edge regulates PI3K, cell polarity, and directional cell movement. J Cell Biol *167*, 505-518.
Shao, J.Y., and Xu, J. (2002). A modified micropipette aspiration technique and its application to tether formation from human neutrophils. J Biomech Eng *124*, 388-396.
Sick, S., Reinker, S., Timmer, J., and Schlake, T. (2006). WNT and DKK determine hair follicle spacing through a reaction-diffusion mechanism. Science *314*, 1447-1450.
Srinivasan, S., Wang, F., Glavas, S., Ott, A., Hofmann, F., Aktories, K., Kalman, D., and Bourne, H.R. (2003). Rac and Cdc42 play distinct roles in regulating PI(3,4,5)P3 and polarity during neutrophil chemotaxis. J Cell Biol *160*, 375-385.
Sun, C.X., Downey, G.P., Zhu, F., Koh, A.L., Thang, H., and Glogauer, M. (2004). Rac1 is the small GTPase responsible for regulating the neutrophil chemotaxis compass. Blood *104*, 3758-3765.
Swaminathan, R., Hoang, C.P., and Verkman, A.S. (1997). Photobleaching recovery and anisotropy decay of green fluorescent protein GFP-S65T in solution and cells: cytoplasmic viscosity probed by green fluorescent protein translational and rotational diffusion. Biophys J *72*, 1900-1907.
Turing, A.M. (1952). The Chemical Basis of Morphogenesis. Philosophical Transactions of the Royal Society of London *237*, 37-72.
Wedlich-Soldner, R., Altschuler, S., Wu, L., and Li, R. (2003). Spontaneous cell polarization through actomyosin-based delivery of the Cdc42 GTPase. Science *299*, 1231-1235.
Weiner, O.D., Marganski, W.A., Wu, L.F., Altschuler, S.J., and Kirschner, M.W. (2007). An actin-based wave generator organizes cell motility. PLoS Biol *5*, e221.

Weiner, O.D., Neilsen, P.O., Prestwich, G.D., Kirschner, M.W., Cantley, L.C., and Bourne, H.R. (2002). A PtdInsP(3)- and Rho GTPase-mediated positive feedback loop regulates neutrophil polarity. Nat Cell Biol *4*, 509-513.
Weiner, O.D., Rentel, M.C., Ott, A., Brown, G.E., Jedrychowski, M., Yaffe, M.B., Gygi, S.P., Cantley, L.C., Bourne, H.R., and Kirschner, M.W. (2006). Hem-1 complexes are essential for Rac activation, actin polymerization, and myosin regulation during neutrophil chemotaxis. PLoS Biol *4*, e38.
Wessels, D., Soll, D.R., Knecht, D., Loomis, W.F., De Lozanne, A., and Spudich, J. (1988). Cell motility and chemotaxis in Dictyostelium amebae lacking myosin heavy chain. Dev Biol *128*, 164-177.
Xiong, Y., Huang, C.H., Iglesias, P.A., and Devreotes, P.N. (2010). Cells navigate with a local-excitation, global-inhibition-biased excitable network. Proc Natl Acad Sci U S A *107*, 17079-17086.
Zhelev, D.V., Alteraifi, A.M., and Hochmuth, R.M. (1996). F-actin network formation in tethers and in pseudopods stimulated by chemoattractant. Cell Motil Cytoskeleton *35*, 331-344.

Figure 1

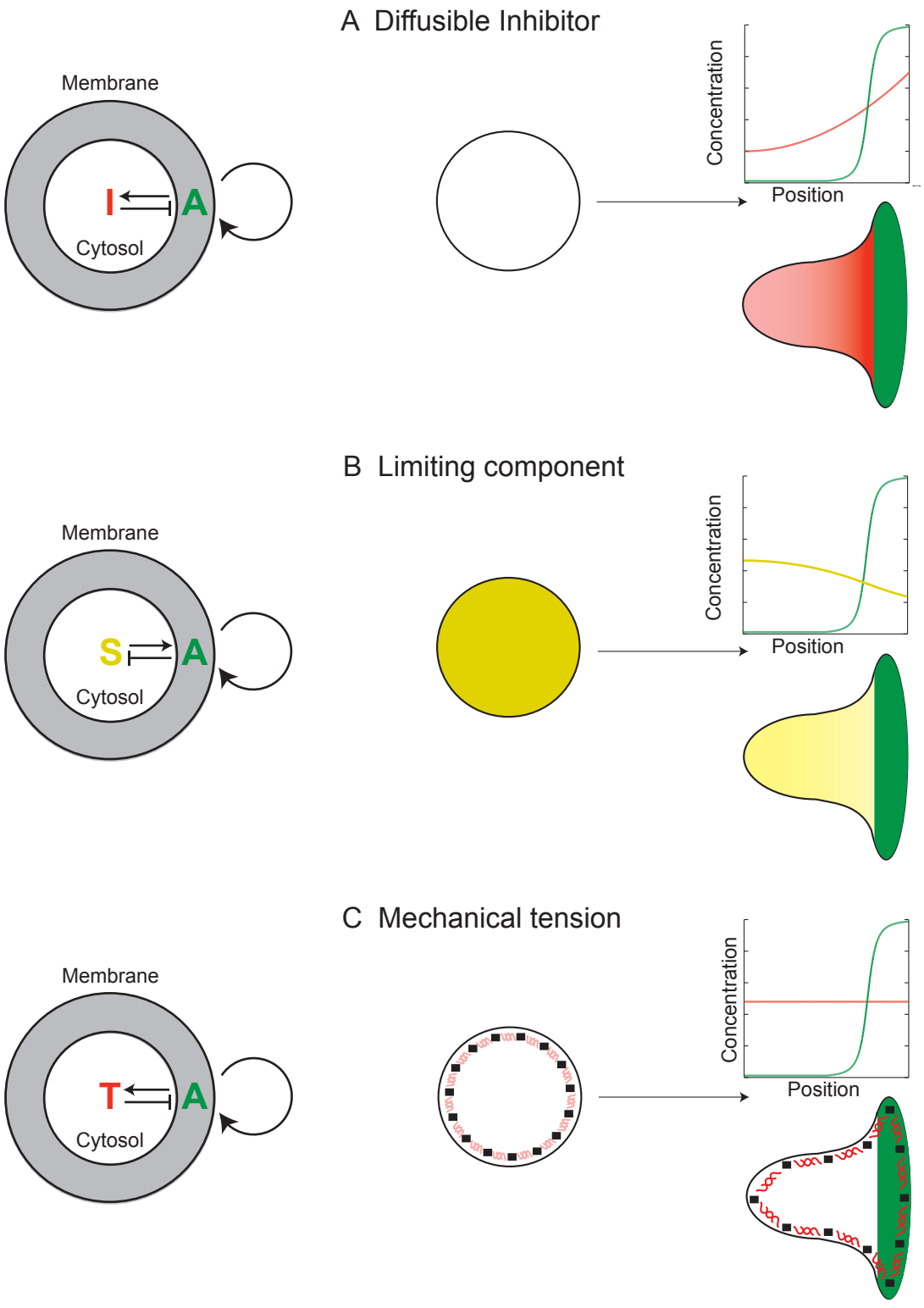
A Diffusible Inhibitor
Membrane
I
A
Cytosol
Concentration
Position
B Limiting component
Membrane
S
A
Cytosol
Concentration
Position
C Mechanical tension
Membrane
T
A
Cytosol
Concentration
Position

Figure 2

A Tether formation in heat-treated HL-60 cells

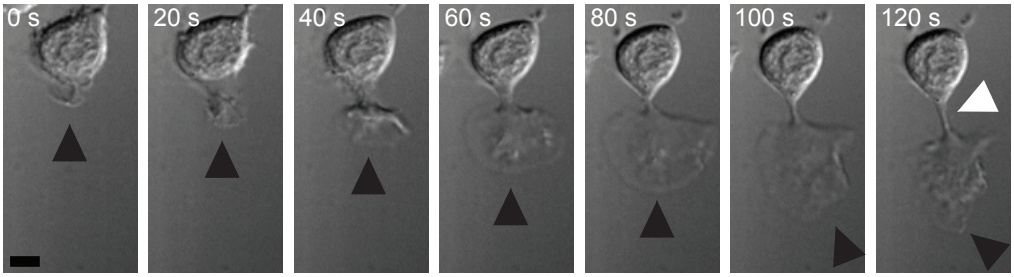

B Maintenance of polarity in tethered HL-60 cells

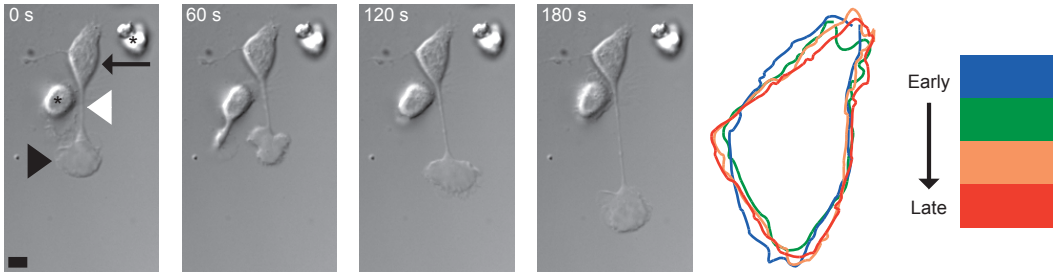

C Simulation of published diffusion-based inhibition models following cell stretching and severing perturbations

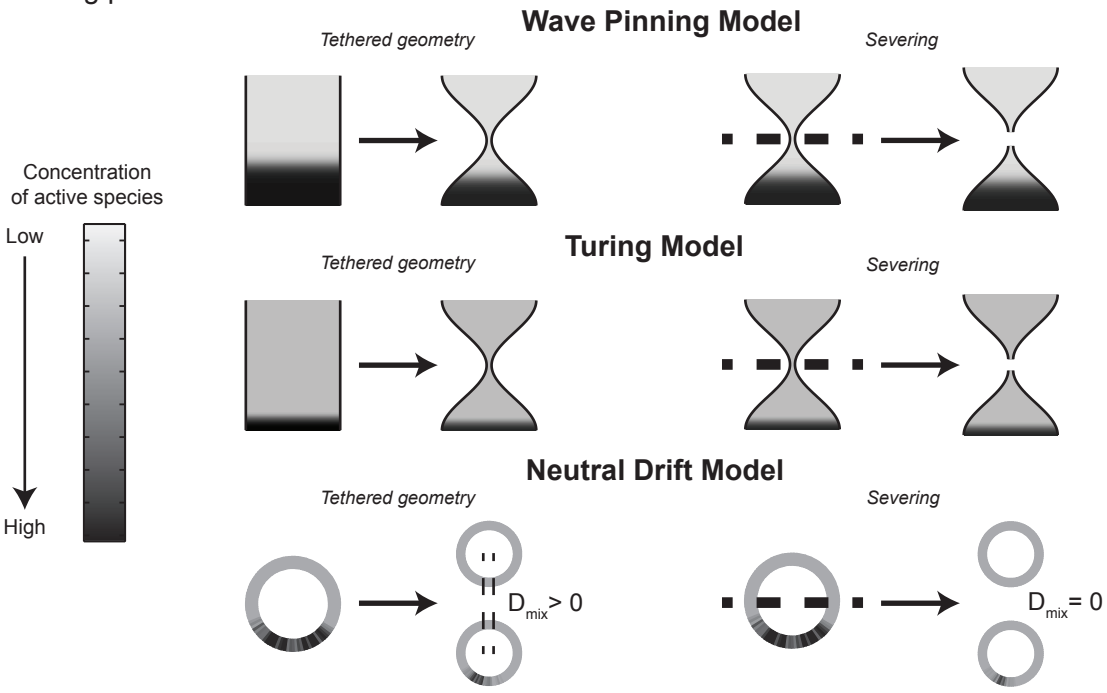

Figure 3

A Outline of Severing Experiments

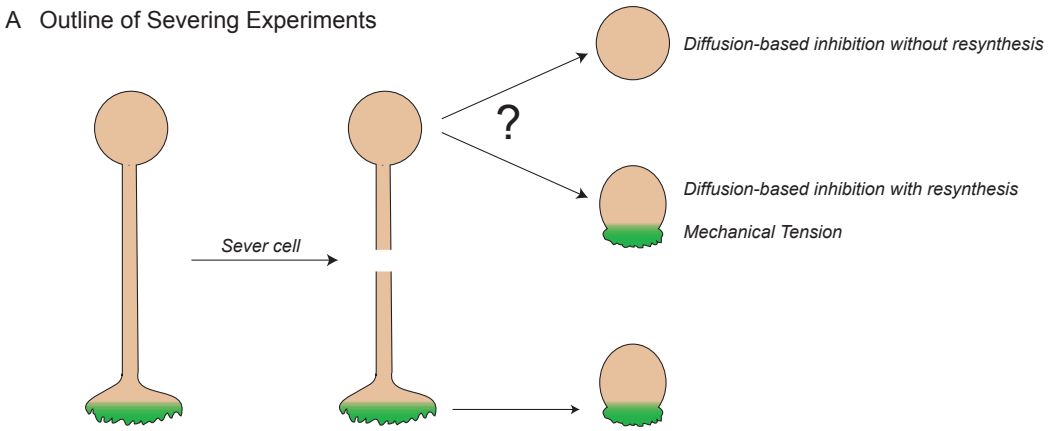

B Pseudopod production after laser severing

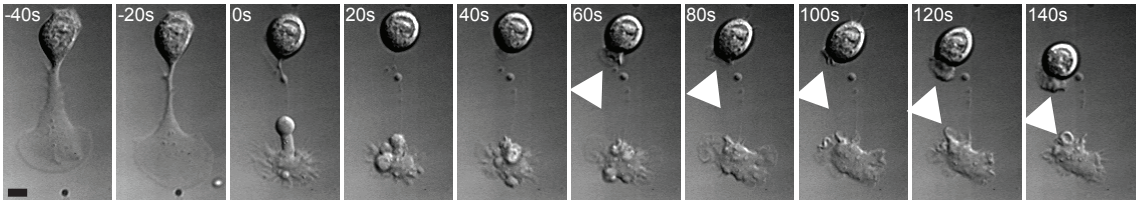

C Pseudopod production after spontaneous tether cleavage

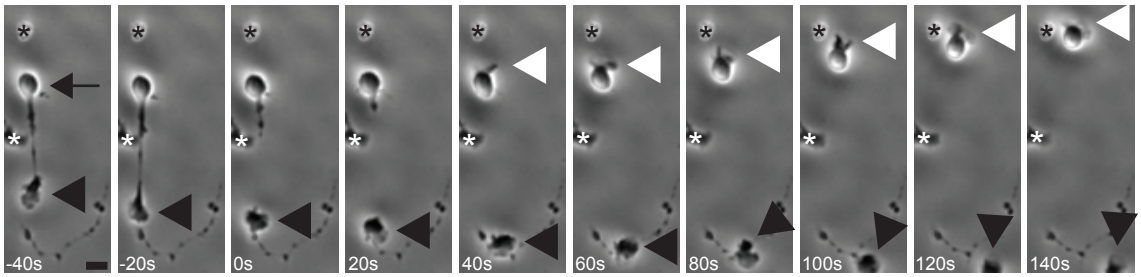

Figure 4

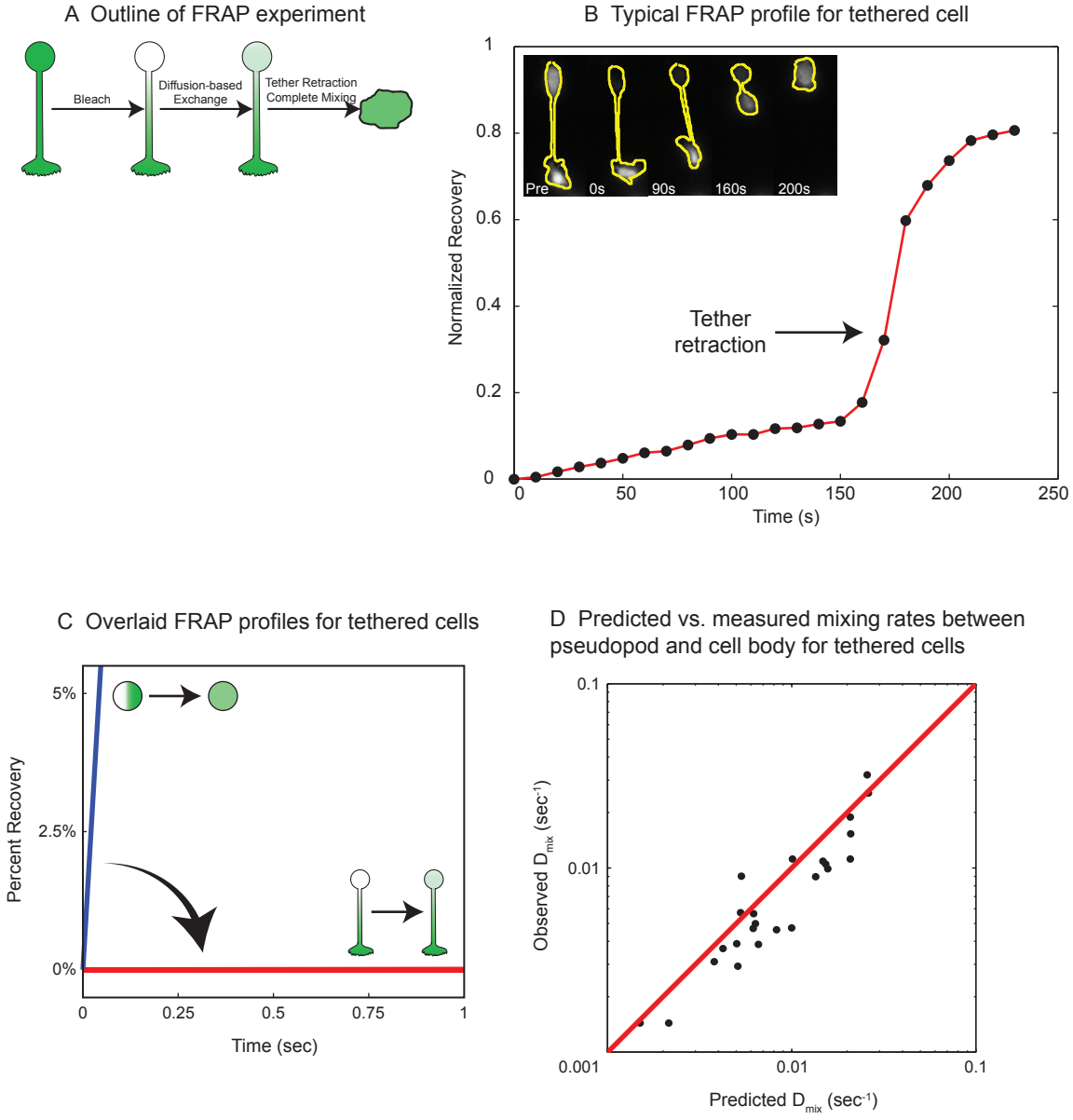
A Outline of FRAP experiment
Bleach
Diffusion-based Exchange
Tether Retraction Complete Mixing
B Typical FRAP profile for tethered cell
Pre
0s
90s
160s
200s
Normalized Recovery
Tether retraction
Time (s)
C Overlaid FRAP profiles for tethered cells
Percent Recovery
5%
2.5%
0%
Time (sec)
D Predicted vs. measured mixing rates between pseudopod and cell body for tethered cells
Observed D_mix (sec^-1)
Predicted D_mix (sec^-1)

Figure 5

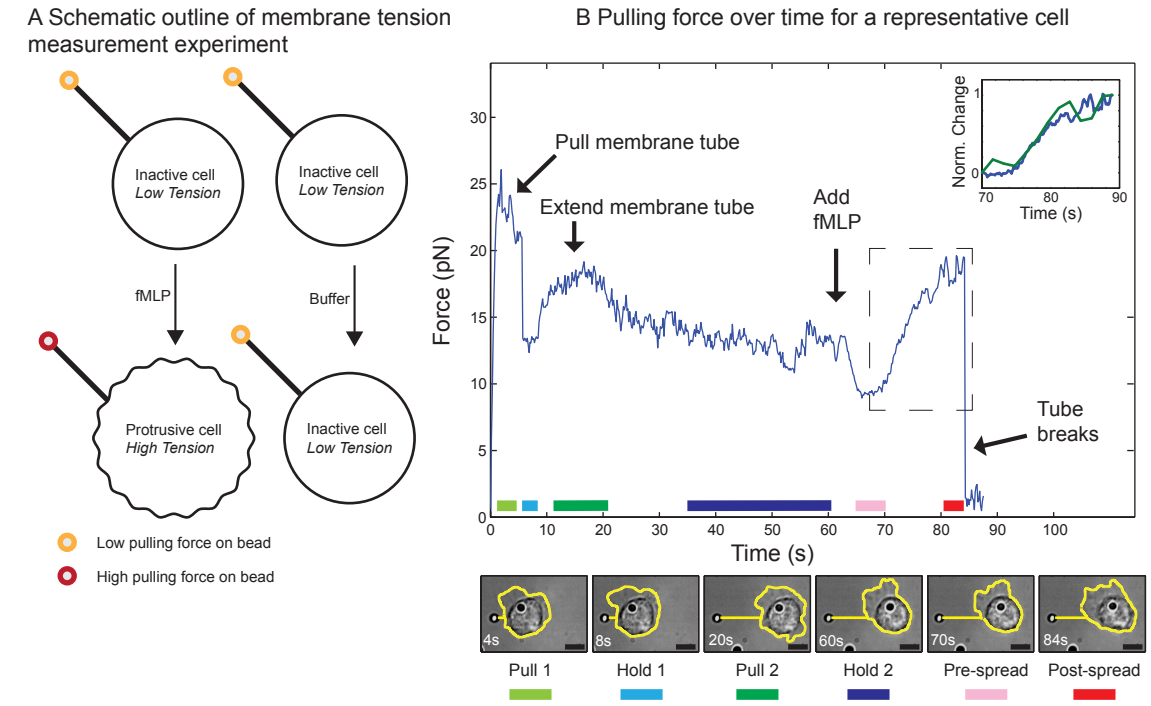
A Schematic outline of membrane tension measurement experiment
Inactive cell
Low Tension
Inactive cell
Low Tension
fMLP
Buffer
Protrusive cell
High Tension
Inactive cell
Low Tension
Low pulling force on bead
High pulling force on bead
B Pulling force over time for a representative cell
Pull membrane tube
Extend membrane tube
Add
fMLP
Tube
breaks
Force (pN)
Time (s)
Norm. Change
Time (s)
4s
8s
20s
60s
70s
84s
Pull 1
Hold 1
Pull 2
Hold 2
Pre-spread
Post-spread
C Pulling force over time for individual cells following buffer addition or fMLP stimulation
after buffer
after fmlp
20 pN
20 sec
D Pulling force at different stages of experiment
p = 0.0006
p = 0.0001
Force (pN)
Pull 1
Hold 1
Pull 2
Hold 2
Pre Spread
Post Spread

Figure 6

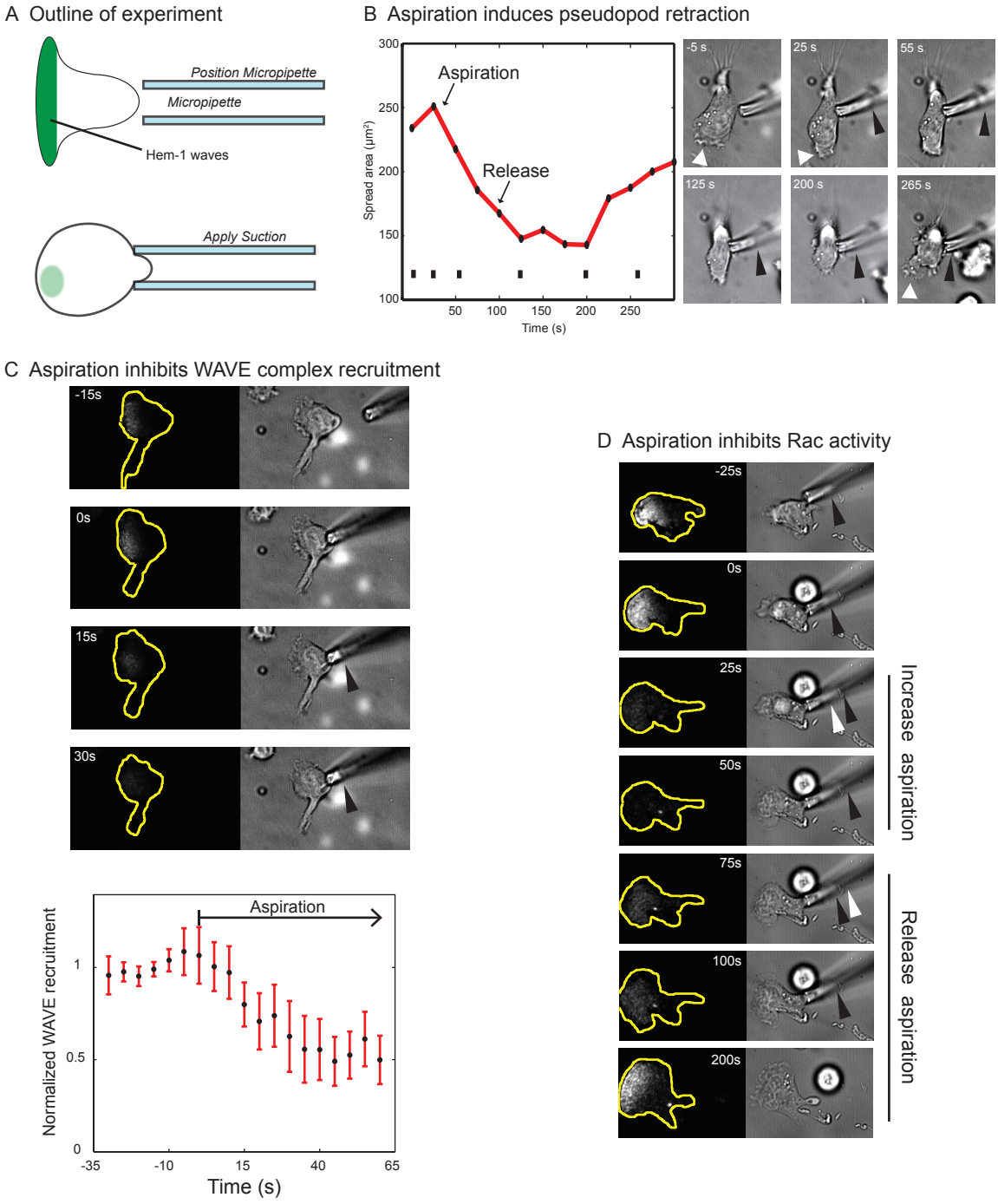
A Outline of experiment
Position Micropipette
Micropipette
Hem-1 waves
Apply Suction
B Aspiration induces pseudopod retraction
Aspiration
Release
Spread area (μm²)
Time (s)
-5 s
25 s
55 s
125 s
200 s
265 s
C Aspiration inhibits WAVE complex recruitment
-15s
0s
15s
30s
Aspiration
Normalized WAVE recruitment
Time (s)
D Aspiration inhibits Rac activity
-25s
0s
25s
50s
75s
100s
200s
Increase aspiration
Release aspiration

Figure 7

A Blebbistatin treatment causes cellular elongation but no enhancement of leading edge signaling

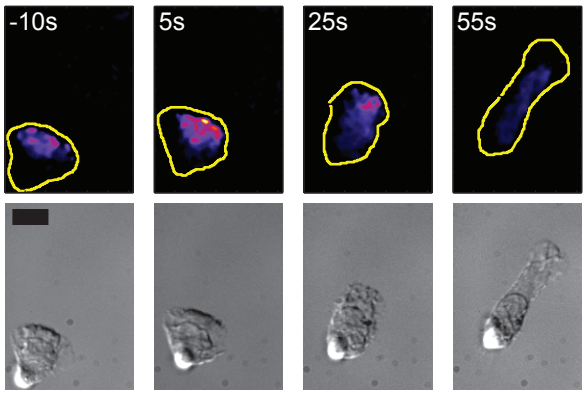

B Combination of hypertonic buffer and blebbistatin causes uniform signaling and spreading

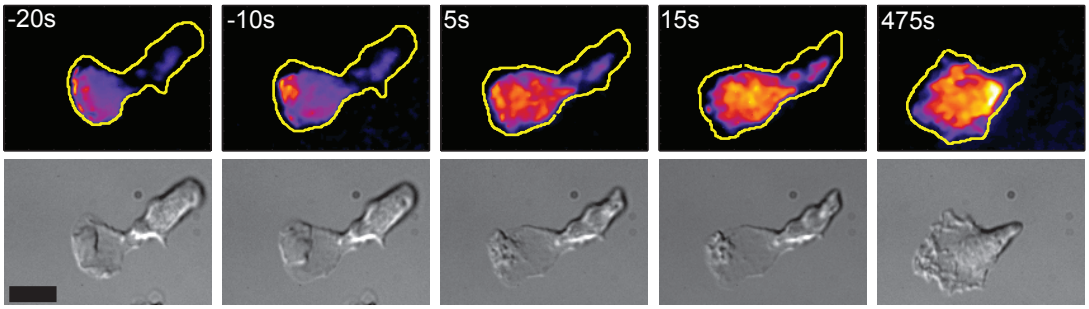

C Quantification of tension reduction effects on signaling

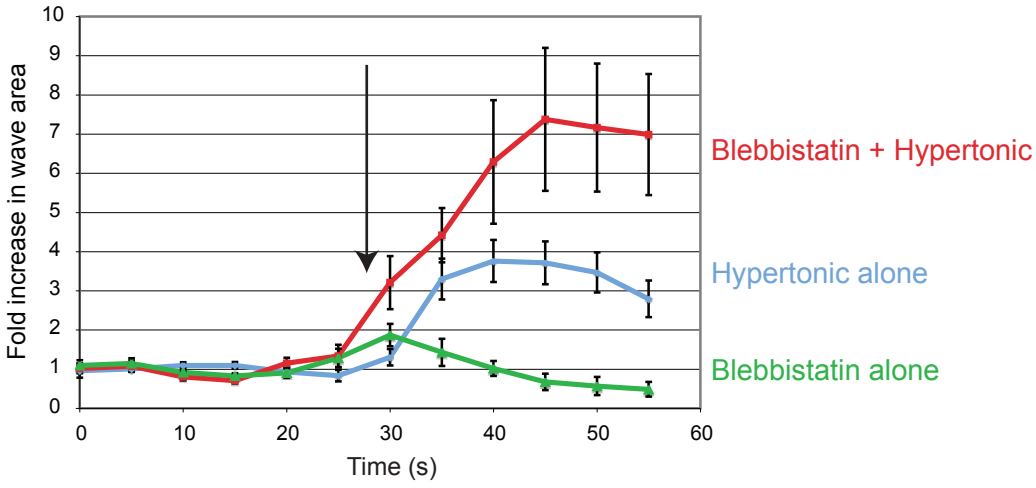

Supplement:

Mechanical tension spatially restricts signals

to the leading edge during neutrophil migration

1 Supplemental Methods

1.1 Cell culture

All of the HL-60 cell lines used in this study were generated, cultured, and differentiated as described previously [15]. Cells were plated on #1.5 coverslips (Gold Seal) that were precoated with 0.2 mg/ml porcine fibronectin (purified from porcine plasma). Experiments were performed in mHBSS medium (150 mM NaCl, 4 mM KCl, 1.2 mM CaCl2, 1 mM MgCl2, 10 mg/mL glucose and 20 mM HEPES, pH 7.2), containing 10% FBS and 50 nM fMLP.

1.2 Primary neutrophil preparation

A drop of healthy human blood, acquired by pinprick, was collected on the center of a sterile coverslip, and neutrophils were isolated as described [2]. The cells were covered with mHBSS medium and incubated at 37°C for 30 minutes prior to the experiments.

1.3 Microscopy

The cell severing and FRAP experiments were performed at 37°C on a Nikon Eclipse TE2000-E inverted microscope with a 60x PlanApo TIRF 1.49 NA objective and an electron microscopy charge-coupled device (EM-CCD) camera (Cascade II 512, Photometrics; http://www.photometrics.com). The microscope was controlled by Nikon Elements 3.0. A focused laser beam, generated by a 435 nm dye cell laser, was used to photobleach or sever the cells (Manually Controlled Micropoint System, Photonic Instruments).

The aspiration experiments as well as blebbistatin and osmotic experiments were performed on a Nikon Eclipse Ti microscope, with a 100X PlanApo TIRF 1.49 NA objective and an EM-CCD camera (Evolve, Photometrics). The microscope was controlled by Nikon Elements 3.0. The microscope was equipped with a Narishige MM-89 micromanipulator with fine hydraulic control of position for micropipette positioning. Suction pressure was controlled with a Narishige IM-300 microinjection system.

The membrane tension measurements were performed on a Nikon Eclipse Ti microscope with a 100x Plan Apo 1.4 NA equipped with a 1064 nm holographic optical tweezers setup similar to described in [9]. The cells were simultaneously visualized in brightfield in the near IR (Allied Vision Technologies, Marlin F-131B NIR) and in fluorescence through a spinning disk confocal system (Andor Revolution). The microscope and optical trap were controlled by home-made MATLAB software.

1.4 Cell tether experiments

Cells were spun at 400xg for 2 minutes and resuspended in 25 μL of buffer. We then plated 12.5 μL of cells on a coverslip and assembled a chamber by placing another coverslip on top and sealing the chamber with a 1:1:1 mixture of

vasoline:lanolin:paraffin. We found sealed chambers to be essential for efficient tether generation, possibly because of a decrease in convective mixing. For spontaneous cleavage experiments, we plated 2 μL of cells instead of 12.5 μL of cells. After plating, we incubated the chambers at 37°C to allow the cells to adhere and begin migrating. We then heated the cells at $45-48^\circ$C for 10-12 minutes, depending on which treatment produced the most tethers that day before returning them to 37°C to allow tether formation. Heat treatment caused a subset of cells (about 30%) to have multiple sites of protrusion. These multipolar cells sometimes had tethers although the extra protrusions were usually eliminated as the tether formed. Nevertheless, we observed each tethered cell for 45 seconds to verify that the cell body was inactive (polarity was maintained) prior to severing.

1.5 Optical trap experiments

Bead preparation: Streptavidin latex beads (2 μm diameter, Micromod) at 0.75 mg/mL were incubated with biotinylated Concanavalin A (Vector Laboratories) at 0.35 mg/mL for 30 min then spun and resuspended twice in DPBS and once in the buffer used for the experiment.

Samples of primary neutrophils were prepared as described above in flow chambers. The buffer was mHBSS with 1.2 mM calcium and 1% BSA. We then stained the neutrophil plasma membranes with DiI for 15 minutes. Beads were added immediately before placing the sample on the microscope. We first trapped a single bead and then moved the sample relative to the trap until we found a healthy neutrophil. We brought bead and neutrophil into contact for a few seconds before separating them by moving the stage at 1 μm/sec. It was often necessary to repeat this process several

times to get a tether to form. DiI fluorescence was used to confirm the existence of a tether. After a tether was pulled to a length of 10-15 m, we flowed in either buffer (control) or buffer containing 50 nM fMLP. We collected near IR brightfield images every 100-200 msec and confocal fluorescence images every 2 seconds. To calculate the tether force, we measured the distance between the bead and the center of the trap. To localize the beads, we analyzed the brightfield images with centroid tracking software in MATLAB (Crocker and Grier, 1996). Optical tweezers stiffness was calibrated from quantification of thermal fluctuations of beads in each trap as described previously (Mejean et al., 2009).

1.6 Aspiration experiments

Cells were spun and resuspended in buffer. They were then plated on fibronectin-coated coverslips and incubated at 37°C for 10 minutes. We washed the cells twice and left them in buffer. Glass capillaries (Sutter Instrument, B100-75-10) were pulled with a needle puller (Sutter Instrument, P-87) to have a very long taper. They were then cut using a microforge (Narishige Group, PF-900) with a glass bead, to have a smooth surface with an approximately 3 μm diameter. The micropipettes were then back-filled with the same buffer in which the cells were plated. This reduced the amount of basal suction pressure due to capillary action to allow better control of the suction pressure with the IM-300. The filled micropipettes were loaded on to the micromanipulator immediately before placing cells on the microscope.

1.7 Osmotic and blebbistatin experiments

Cells in growth media were plated on fibronectin-coated coverslips and incubated at 37°C for 10 minutes. We then washed the cells and left them in buffer (mHBSS) + 20nM fMLP (to stimulate polarization and migration). We began imaging the cells to identify polarized cells expressing Hem-1-YFP. During imaging, we added an equal volume of hypertonic buffer (buffer + 20nM fMLP + 300mM sucrose) to increase the osmolarity of the solution by 150mOsm. At later time points (after the signaling quantification), we added additional sucrose buffer to increase the osmolarity to 225mOsm. The blebbistatin experiments were performed in the same way, except that blebbistatin (66 μM final) was used instead of sucrose. In the blebbistatin/sucrose combination experiments, we pretreated the cells with blebbistatin for 10 minutes and then added hypertonic buffer containing blebbistatin as we did in the hypertonic-alone experiments. In the hypotonic buffer experiments, we added an equal volume of hypotonic buffer (ddH2O + 1mM MgCl2 + 1.2mM CaCl2 + 20nM fMLP) to reduce osmolarity by approximately 170mOsm.

1.8 FRAP Image Analysis

Cellular fluorescence was quantified at each time point using NIS Elements 3.0 by drawing a ROI within the cell and subtracting the mean fluorescence in that region from a background region outside the cell. The signal within the cell body reached its minimum value at the very end of the bleaching. This minimum signal was subtracted from each subsequent time point to calculate the recovery signal. We then calculated the normalized recovery signal by dividing the recovery signal by the drop size. Drop size was equal to the difference between the pre-bleach fluorescence signal and the minimum signal. Generally, the normalized recovery increased linearly during the first

several seconds, so we used linear regression to calculate the normalized fluorescence recovery rate for each cell. A significant amount of that recovery was due to factors other than diffusion of GFP from non-bleached areas of the cell (reversible bleaching, GFP resynthesis), so we also analyzed the normalized fluorescence recovery of cells that lacked tethers. In these cells, there was no separate pool of unbleached GFP, so the recovery was due entirely to reversible photobleaching and GFP resynthesis. By subtracting the recovery rate of untethered cells from the recovery rate of tethered cells, we were able to determine the rate of recovery that was due to GFP diffusion through the tether in each cell. We defined the apparent diffusion coefficient as the rate of normalized fluorescence recovery. We compared this apparent diffusion coefficient with those predicted analytically from cellular geometry (Ehrenfest mixing rate, Main Figure 4D).

1.9 Hem-1 Image denoising

The Hem1-YFP channel of the acquired image series was cropped in space so that only one cell was in the image. The resulting time series was denoised in collaboration with John Sedat, using software developed by Jerome Boulanger [8]. Default parameters were chosen for a two-dimensional time series, except for the patch size, which was 7x7. The effect of the denoising was to remove speckle noise from the background while minimizing feature loss from the waves, which enabled semiautomatic segmentation of the cell and wave regions.

1.10 Hem-1 Quantification

We previously developed image analysis software to quantify Hem-1 dynamics

from TIRF microscopy movies [10]. We used this software to compute the number of pixels that contained Hem-1 signal with a user-defined threshold of the Hem-1 YFP signal. We normalized the number of pixels containing Hem-1 signal at each point to the number of pixels containing Hem-1 signal at the first time point.

2 Modelling Overview

We test whether several existing diffusion-based models of cell polarity are sufficient to explain new observations of neutrophils stretching and severing. The results of the previously described experiments provided us with three typical behaviors for polarized neutrophils:

(B1) when neutrophils were stretched into a tethered morphology, the region of frontness was not lost;

(B2) while stretched, no new sites of frontness appeared elsewhere;

(B3) when the tether was severed, frontness could reform on both halves.

2.1 Reassessment of existing mathematical models

Many models have been proposed to explain the creation and/or maintenance of cell polarity. These models were typically developed for prototypical cells with standard spherical geometries or assumed a 1D spatial geometry to denote the “front-back” axis. The observations of polarized neutrophils in different stretched and nonconvex cell geometries provided an opportunity to test the consistency of mathematical models and experimental results in these novel settings.

2.2 Justification of model choices

We chose to focus on three diffusion-based polarity models: the Neutral Drift Polarity model [1]; Wave Pinning [11]; and Turing [13]. These models share several common properties, namely: the total amount of molecules are assumed to be constant during the time frame of polarization; molecules can be in two states, typically considered to be localized at the membrane (active) or cytosol (inactive); and diffusion on the membrane is considered to be much slower than in the cytosol. These models were also chosen because they are conceptual, rolling many as-yet poorly characterized details of the polarity network into generic mechanisms of interaction and feedback. We thus evaluated the performance of mathematical models based on their ability to achieve these three behaviors.

2.3 Geometry of the cell

Consider a cell that is split into two parts of equal size (``left'' and ``right''), and of a narrow bridge of length L connecting them. Let V_{cell} denote the cell volume, and V_{neck} the volume of the neck. We assume for simplicity that V_{neck} is a cylinder with constant cross section, or, in the 2D case, that V_{neck} is a rectangle.

3 Neutral Drift Polarity model

We considered the so-called Neutral Drift model of polarity, inspired by the polarization of Cdc42 in yeast [1]. In this model, a finite number of particles moved spontaneously, and in a non-directed fashion, from the cytoplasm to the membrane with rate k_{on} and in the reverse direction with rate k_{off}. Additionally, positive feedback

enabled a particle on the membrane to recruit a particle from the cytoplasm to its location with rate k_{fb}, after which the particles underwent independent Brownian motions on the membrane with diffusion constant D. Particles within the cytosol were assumed to diffuse much faster than D and were treated as a pool. Mathematical analysis previously showed that for large numbers of particles the system tended to a homogeneous equilibrium distribution on the membrane, whereas for intermediate numbers of particles the system transiently and recurrently formed polarized regions of particles [1, 5].

To apply this idea to the current study, we modified the model to account for a neutrophil being stretched into ``left'' and ``right'' halves of equal volumes connected by a thin neck (see section 2.3). In this case, model parameters were as before on each half, but cytoplasmic particles were allowed to mix between the two halves with a mixing rate D_{mix}. We further removed the constraint that feedback strength varies with the number of particles to keep a fixed percentage of particles on the membrane. In this formulation, feedback operates strictly by mass action, and a threshold for the number of particles exists, below which polarity is suppressed and above which polarity spontaneously appears [5]. During short time intervals, in which no membrane-cytoplasm particle transitions occurred, the total number of cytoplasmic particles $N = n_{LC} + n_{RC}$ remained constant, while only the sizes of the right ($n(t) = n_{RC}$) and left ($N - n_{RC}(t) = n_{LC}$) pools changed. This process is analogous to the classic Ehrenfest process that models mixing of particles in two connected gas chambers [14], for which the mean and standard deviation of the number of particles can be computed explicitly (see next section):

$$\mathrm{E}[n(t)] = \frac{N}{2}(1 - e^{-2D_{mix}t}), \tag{1}$$

$$\sigma^2[n(t)] = N(1 - e^{-4D_{mix}t}). \quad (2)$$

Importantly, a mathematical approximation can be derived that relates the Ehrenfest mixing rate to the geometry and diffusion rate of the stretched cell. If L is the length of the neck, D is a measured cytosolic diffusion rate, and V_{neck} and V_{cell} are the volumes of the neck and cell respectively, then

$$L \approx \sqrt{\frac{D}{D_{mix}} \frac{V_{neck}}{V_{cell}}}. \quad (3)$$

An intuitive argument can now be given as to why this model (or, in fact, any model that requires particles to diffuse at a finite rate between the body and the head of the cell), with no additional mechanisms, will not give behaviors consistent with the experimental observations of stretched neutrophils with long necks. For a given observation period in time, L can be made large enough, or equivalently D_{mix} small enough, that no (or an insignificant number of) particles are expected to transit from one side to the other. During this time, model behaviors are then the same for both cases, regardless of whether the neck is very thin or cut. However, this contradicts the experimental observation that polarization behavior changes between well-stretched and severed cells.

To illustrate the behavior of the model for well-stretched and cut cells, we simulated the evolution of particles for cells with various neck lengths. Partitioning the cell into two halves required us to consider volume effects. On- and off-rates were unaffected: each particle still had the same probability of spontaneously associating or disassociating from the membrane. However, dropping the volume commensurately increased the feedback rates for each half to account for the increased concentration of particles near each membrane. We simulated the stochastic process for N = 1000

particles as previously described [1]. Model parameters for each half were: k_{on} = .01 min^{-1}; k_{off} = 9 min^{-1}; k_{fb} = 20 min^{-1}; to compute L, we used: $D = 10\mu m^2$/sec, $\frac{V_{neck}}{V_{cell}}$ = 0.1. For these parameters, about 100 particles are expected to be on the membrane at equilibrium [1]. We next investigated how these 100 particles were distributed on each half during stretching, and whether each side could, in principle, be stimulated to polarize as observed for behavior B3.

First, we assumed that the left side of an unstretched cell had polarized with n_m particles on the left membrane. For simplicity, we assumed that the right membrane was empty and that the remaining particles in the cytosol were divided equally between the two halves. We next effectively varied neck length L by setting appropriate D_{mix} between the two halves. Finally, to test whether stimulated polarization could occur on the right half we moved n_m of the particles from the right cytosol onto the right membrane. Then, we evolved for 30 (virtual) minutes the particle system which, for our model parameters, started with 450 cytosolic particles on each half and 100 left and 0 right membrane particles. When the length L was small, the numbers of cytosolic particles rapidly equalized between the cell halves and, with equal probability, one or the other side lost all membrane particles. However, as L increased, only the left side (corresponding to the pseudopod) stayed polarized; the right side (corresponding to the cell body) was unable to maintain enough particles on the membrane to be considered polarized regardless of the large numbers of initial particles placed on the membrane (Figure S1). Similarly, our simulation showed that the right side could not polarize when we simulated cutting the cell (we performed simulations exactly as before except with D_{mix} = 0). Thus, behavior B3 was violated (Supplemental Figure S1).

4 Derivation of equation (3)

4.1 Brownian motion

Suppose particles undergo Brownian motion with diffusion coefficient $D > 0$. Let $p(t,x)$ be the probability density that one finds a particle at the point $x \in V_{cell}$, at time $t > 0$. Then

$$\frac{\partial p}{\partial t} = \tfrac{1}{2} D \Delta p. \qquad (4)$$

Assuming that particles bounce off the boundary of the cell (and do not get absorbed), we must impose Neumann boundary conditions, i.e. ∇p is everywhere tangential to the boundary (``$\frac{\partial p}{\partial n} = 0$").

Solutions to this equation can be found by expanding p in eigenfunctions of the Laplacian. Let the eigenfunctions be φ_n, with eigenvalues $-\lambda_n$, so

$$-\Delta \varphi_n = \lambda_n \varphi_n, \qquad 0 = \lambda_0 < \lambda_1 \le \lambda_2 \le \cdots. \qquad (5)$$

The lowest eigenvalue is $\lambda_0 = 0$, and its corresponding eigenfunction is a constant $\varphi_0(x) = 1$.

The second eigenvalue λ_1 is given by the Raleigh quotient

$$\lambda_1 = \min\{\frac{\int_C |\nabla u|^2 \, dx}{\int_C u^2 dx} : \int_C u dx = 0\}. \qquad (6)$$

Any minimizing function u is an eigenfunction φ_1.

4.2 The limit of a very narrow bridge

By substituting any function u in the Raleigh quotient one gets a upper bound for λ_1. In particular, one can try the following function

$$u_1(x) = \begin{cases} +1 & \text{on the left half} \\ -1 & \text{on the right half} \\ \text{linear} & \text{in between on the bridge} \end{cases}$$

The gradient of this function vanishes everywhere except in the neck V_{neck}, where it is given by

$$\nabla u_1 = \frac{2}{L}\,\vec{\mathbf{e}}_1$$

and $\vec{\mathbf{e}}_1$ is the unit vector along the axis of the bridge going from left to right. The "2" in the numerator is the difference between the values of u_1 at the ends of the bridge.

The Raleigh quotient for this function is thus

$$\lambda_1 \le \frac{\int_C |\nabla u_1|^2}{\int_C u_1^2} = \frac{\int_B (2/L)^2\,dx}{\int_C u_1^2} \approx \frac{4}{L^2}\frac{V_{neck}}{V_{cell}}.$$

Here we assume that the bridge is much smaller than the cell ($V_{neck} << V_{cell}$) and thus that $u_1 = 1$ on most of the cell. This implies $\int_{V_{cell}} u_1^2 \approx V_{cell}$.

If the volume of the neck is much smaller than the cell, then this implies that $\lambda_1 << L^{-2}$ is a small number, and one can show that in the limit $V_{neck}/V_{cell} \to 0$ the eigenfunction φ_1 converges to u_1 (i.e. it becomes constant on each half, and transitions linearly between these two constants along the bridge.) It follows that for $V_{neck} << V_{cell}$ one has

$$\lambda_1 \approx \frac{4}{L^2}\frac{V_{neck}}{V_{cell}} \tag{7}$$

$$\varphi_1 \approx u_1. \tag{8}$$

4.3 The Ehrenfest diffusion rate

Suppose that initially there are no particles on the right, and that N particles are uniformly distributed on the left. If the bridge is very narrow, then we can write the initial particle distribution as

$$p(0,x) \approx NV_{cell}^{-1}\{\varphi_0(x) + \varphi_1(x)\}.$$

Using the fact that both φ_0 and φ_1 are (nearly) constant on the left and right halves of the cell, one finds that the above expression simplifies to

$$p(0,x) \approx \begin{cases} 2NV_{cell}^{-1} & \text{on the left half} \\ 0 & \text{on the right half} \\ \text{linear} & \text{in between on the bridge} \end{cases}$$

From this one sees that $\int_{V_{cell}} p dx = N$, i.e. the total number of particles is indeed N. (we assume the bridge is narrow so its contribution to the integral is negligible.)

The particle density $p(t,x)$ evolves by the heat equation with diffusion coefficient $D/2$, and the functions φ_j are eigenfunctions with eigenvalue λ_j, so at time $t > 0$ the particle distribution must be

$$p(t,x) \approx NV_{cell}^{-1}\{e^{-D\lambda_0 t/2}\varphi_0(x) + e^{-D\lambda_1 t/2}\varphi_1(x)\}$$

$$= NV_{cell}^{-1}\{\varphi_0(x) + e^{-D\lambda_1 t/2}\varphi_1(x)\}.$$

The expected number of particles in the right half of the cell is

$$\mathsf{E}n_R(t) = \int_{\text{right half}} p(t,x)dx.$$

In the right half we have $\varphi_0 = 1$ and $\varphi_1 \approx -1$, so on the right half of the cell the particle density is approximately

$$p(t,x) \approx \frac{N}{V_{cell}}(1 - e^{-D\lambda_1 t/2}.)$$

This implies

$$\mathsf{E}n_R(t) \approx \frac{N}{V_{cell}} \int_{\text{right half}} (1 - e^{-D\lambda_1 t/2})dx = \frac{N}{2}(1 - e^{-D\lambda_1 t/2}).$$

In the Ehrenfest model, where particles can jump from the left half to the right or back at a rate of D_{mix} times per second, one finds under the same assumptions that

$$\mathsf{E}n_R(t) = \frac{N}{2}(1 - e^{-2D_{mix}t}).$$

Thus we find this relation between the Brownian diffusion rate D of particles in the cell, and the mixing rate D_{mix} for the Ehrenfest model:

$$D_{mix} = \frac{D}{4}\lambda_1 = \frac{D}{L^2}\frac{V_{neck}}{V_{cell}}.$$

This relation is valid under the assumption that the bridge is very narrow (V_{neck} = V_{cell}).

5 Reaction-Diffusion (RD) Models for Cell Polarity

Since polarity defines a single ``front-back'' axis, most proposed RD models for cell polarity have been studied on a one-dimensional uniform domain. To account for the effect of shape change in the current study, we modified the conservation equation for particle density to take into account the effect of non-constant cross-sectional area $A = A(x,t)$ (see [7]):

$$\frac{\partial u(x,t)}{\partial t} = D\frac{\partial^2 u}{\partial x^2} + \frac{D}{A}\frac{\partial A}{\partial x}\frac{\partial u}{\partial x} - \frac{u}{A}\frac{\partial A}{\partial t} + f(u). \qquad (9)$$

This 1D approximation is valid, provided that the particle distribution in the transverse (y) direction equilibrates much faster than in x direction and is constant in

y (see [4] for detailed derivation). (Note that the second (advection-like) term on the RHS of (9) represents a correction to the diffusion process due to changes in shape, while the last term represents dilution of concentration due to changes in volume.)

Using this approach, we consider the following generalization of a two component RD model:

$$\frac{\partial u(x,t)}{\partial t} = D_u \frac{\partial^2 u}{\partial x^2} + \frac{D}{A}\frac{\partial A}{\partial x}\frac{\partial u}{\partial x} - \frac{u}{A}\frac{\partial A}{\partial t} + f(u,v), \tag{10a}$$

$$\frac{\partial v(x,t)}{\partial t} = D_v \frac{\partial^2 v}{\partial x^2} + \frac{D}{A}\frac{\partial A}{\partial x}\frac{\partial v}{\partial x} - \frac{v}{A}\frac{\partial A}{\partial t} + g(u,v). \tag{10b}$$

We consider u and v to be different states of a single polarity protein, such as a Rho GTPase. We assume that u is the active (membrane-bound) form of the protein, and v is the inactive (cytosolic) form. We treat u and v as effective mean concentrations within a vertical column throughout the cell, thus considering the two species as residing in the same domain. Note that the cytosolic form has higher diffusivity than the membrane-bound form ($D_v >> D_u$). Due to the interconversion between the two states we have $f(u,v) = -g(u,v)$. Thus, system (10) satisfies mass conservation for the total amount of material in the cell.

We consider two such mass-conserved models, the first, referred to as the Otsuji model, is based on Turing instability. The second one, referred to as the Wave-Pinning model, is based on travelling wave phenomena. In the experiments described in the Main Text, the cell is prepolarized before the pseudopod crawls away and the tether forms. To simulate this behavior for the Otsuji and Wave-Pinning models (Main Figure 2C), we allowed the cells to establish polarity with ``normal'' morphologies (Main Figure 2C, far left panels) and then gradually converted the cell into a tethered morphology

while continuing the simulation for each of the three models. In both cases, we varied the geometry of the cell by a dumbbell shape in which we allow a neck to form and ultimately pinch off. We then continued the simulation to obtain steady state signal concentration profiles in the tethered morphology for each model (Main Figure 2C, mid left panels). In both models, tether formation did not cause the unpolarized side of the cell (the cell body) to become polarized.

6 Otsuji model

We considered a recent model for polarization of neutrophils that made use of a Turing mechanism for pattern formation [13]. This model consists of a mass-conserved reaction-diffusion (RD) system, where the homogeneous steady state (corresponding to the unpolarized cell) undergoes a diffusion-driven (Turing) instability. Several other models proposed for cell polarity based on diffusion-driven instability [6], [12] also share mass-conservation of components and exhibit similar behaviors, despite being based on different molecular networks.

The Otsuji model is given by equations (10) with reaction kinetics

$$f(u,v) = -g(u,v) = a_1\left[v - \frac{u+v}{\left(a_2 s(u+v)+1\right)^2}\right]. \qquad (12)$$

We use realistic diffusion coefficients for Rho GTPases ($D_u = 0.1\mu\mathrm{m}^2/\sec$, $D_v = 10\mu\mathrm{m}^2/\sec$) and rescale the published parameter values from [13] to obtain $a_1 = 25\sec^{-1}$, a_2 =0.7 $\mu\mathrm{M}^{-1}$ and initial conditions $u+v = 2\mu\mathrm{M}$.

Numerical simulation showed that for a 1-D domain with constant cross-sectional area multiple polarized peaks are ultimately unstable, resulting in a single stable peak [13]. To mimic the experimental situation, we initially allowed a cylindrical cell to polarize

forming a single peak . We then stretched the neck, and finally allowed it to pinch off. Our simulation showed that polarization behaviors are similar for highly stretched cells and severed cells (Main Figure 2C). Thus, since one of the cut halves could not repolarize, condition B3 was violated.

7 Wave-pinning (WP) model

We next considered a representative from a different class of RD models for cell polarity, the wave-pinning model [11]. The WP model consists of equations (10) with bistable reaction kinetics

$$f(u,v) = -g(u,v) = v\left(k_0 + \frac{\gamma u^2}{K^2 + u^2}\right) - \delta u. \qquad (13)$$

We used previously published parameters from [11]: D_u = 0.1 μ m^2/sec, D_v = 10 μ m^2/sec, k_0 =0.067 sec^{-1}, $\gamma = 1$ sec^{-1}, K = 1 μ M, and δ =1 sec^{-1}.

The WP model does not undergo a Turing instability. Instead, an external stimulus triggers a travelling wave of activation, which spreads throughout the cell, decelerates, and eventually stops inside the domain, forming a stationary ``frontness'' region. Pinning of the travelling wave is dependent on depletion of the fast-diffusing inactive form due to mass conservation, and the size of the polarized region is directly proportional to the total amount of u and v in the cell.

As with the previous model, we allowed the cell to polarize on one side and then allowed a neck to pinch the cell into two halves. Again, our simulation showed that polarization behaviors are similar for highly stretched cells and severed cells (Main Figure 2C). Hence, condition B3 was violated.

8 Molecular accounting of re-synthesis for the neutral drift polarity model

In the neutral drift model after severing the unpolarized cell half will not have enough particles to polarize. However, one might be concerned that degradation and synthesis of particles could regenerate polarity. Here we present a simple argument that suggests that this is not the case. We make the following simplifying assumptions:

1. We assume a constant production rate of molecules in a given volume per unit time and and first order degradation rate. We assume that these physical parameters are independent of the cell state (such as whether it is severed, stretched, etc.). The newly produced molecules are assumed to be in the cytosolic (unpolarized) state.

2. We assume that prior to severing the left half of the cell is polarized, while the right half is unpolarized. After severing, the right half is able to reanimate within a given amount of time.

3. We assume that in the tethered state exchange of molecules occurs between the two compartments via an Ehrenfest model of diffusion. We further assume that only cytosolic molecules can exchange compartments. The relationship between the Ehrenfest mixing rate and the diffusion coefficient for the dumbbell geometry is as calculated earlier.

We will show that a *de novo* production of particles that ensures the cell reanimates after severing, but not during stretching, requires an unrealistic diffusion coefficient for the cytosolic particles. Let $N(t)$ be the total number of particles in the right half. Then

$$\frac{dN}{dt} = k_{\text{prod}} - k_{\text{deg}} N,$$

where k_{prod} is the number of particles produced per unit time, and k_{deg} is a first order degradation rate. At steady state, the total number of particles in the right half is

$N_{ss} = k_{prod}/k_{deg}$, and we can rewrite the equation as

$$\frac{dN}{dt} = k_{deg}(N_{ss} - N),$$

and hence

$$\frac{d(N_{ss} - N(t))}{dt} = -k_{deg}(N_{ss} - N(t)),$$

so that the quantity $N_{ss} - N(t)$ decays exponentially.Thus, starting with N_0 particles,

$$N_{ss} - N(t) = (N_{ss} - N_0)e^{-k_{deg}t}. \qquad (14)$$

Now, there are two scenarios for which we need to consider the solutions: the time after severing required for the right half to polarize (denoted by T); and the time before severing during which the cell is stretched and two halves of the cells are tethered (the left half is assumed polarized and the right is not). We denote this time by nT. Note that the cell body requires less time to reanimate after severing than it spends in an unpolarized stretched state prior to severing. (As reference, $T \approx 50\,\mathrm{sec}$ and $n \approx 3$.)

We first consider the time required for the right cell to reanimate, in order to obtain an estimate for the degradation rate. One of the main features of the neutral drift model is that there is critical number of particles, N_c^* that can be accommodated in the cytosol. When $N < N_c^*$ all particles are in the cytosol, and for $N > N_c^*$, we have, on average, $N - N_c^*$, present on the membrane. We introduce two additional thresholds. First, we let $N_{np} = N_c^* + \sqrt{N_c^*}$ be a ``no polarization'' threshold. This is the minimum number of particles required to empirically observe polarization (resulting in $\sqrt{N_c^*}$ particles on the membrane). Second, we let $N_p$ be a ``polarization'' threshold. When particle density is

above this value, polarization is very likely to be observed. These two thresholds are assumed to be reasonably well separated with $N_{np} < N_p < N_{ss}$. Define

$$\alpha = \frac{N_{ss} - N_{np}}{N_{ss} - N_p}$$

(Note that $\alpha > 1$ by definition). Now, for the right side to polarize after T seconds, we require $N(T) = N_p$, and assume that prior to severing $N_0 = N_{np}$. Our explicit solution (14) gives

$$N_{ss} - N_p = (N_{ss} - N_{np})e^{-k_{\deg} t},$$

and the degradation constant can be simply written as

$$k_{\deg} = \frac{\ln \alpha}{T}.$$

As an example, consider $N_c^* = 450$, and choose $N_{np} = 470 \approx N_c^* + \sqrt{N_c^*}$, $N_p = 480$, and $N_{ss} = 500$ and $T \approx 35\sec$. Then $k_{\deg} = \frac{\ln(1.5)}{35} \approx 0.012 \text{particles}/\sec$, and $k_{prod} \approx 5.8 \text{particles}/\sec$.

We next consider the period of time during which the two halves are connected by a tether. During that time mixing between the two halves occurs at rate D_{mix}. We assume that particles are building up in the cytosol due to production at rate k_{prod}, and investigate whether loss of particles through the tether can prevent polarization from occurring. (During this time, we assume that there are no particles on the membrane - this is reasonable when membrane on-events are rare - and test in the analysis below whether enough particles could theoretically build up in the cytosol so that a nucleation event could even lead to polarization.) The rate of change is given by

$$\frac{dN}{dt} = k_{deg}(N_{ss} - N) - D_{mix}(N - N_c^*). \quad (15)$$

Note that since the left half is polarized, the number of particles in that compartment available for cytosolic mixing through the tether is N_c^*. In order to keep the cell body unpolarized during this stage, we require $N(t < nT) \le N_{np}$, and for $N = N_{np}$ the rate of mixing must be no less than the net rate of particle creation (i.e., $dN/dt \le 0$). It follows that

$$k_{deg}(N_{ss} - N_{np}) \le D_{mix}(N_{np} - N_c^*).$$

Rearranging, we obtain

$$D_{mix} \ge k_{deg} \frac{N_{ss} - N_{np}}{N_{np} - N_c^*}.$$

Recall that we have previously calculated the relation between the mixing rate and the cytosolic diffusion coefficient for the stretched dumbbell geometry:

$$D = L^2 \frac{V_{cell}}{V_{neck}} D_{mix}.$$

It follows that

$$D \ge L^2 \frac{V_{cell}}{V_{neck}} \frac{\ln \alpha}{T} \frac{N_{ss} - N_{np}}{N_{np} - N_c^*}.$$

To gain insight into the constraints that this relationship places on the required diffusion coefficient during the tethered period, we estimate the parameters as follows: $L = 25\mu\text{m}$, $V_{cell}/V_{neck} = 31$ and $T = 35\,\text{sec}$. As before, using $N_c^* = 450$, $N_{np} = 470$, $N_p = 480$, and $N_{ss} = 500$, results in $\alpha = 1.5$ and

$$\frac{N_{ss} - N_{np}}{N_{np} - N_c^*} = \frac{500 - 470}{470 - 450} = \frac{30}{20} = 1.5.$$

It follows that

$$D \geq L^2 \frac{V_{cell}}{V_{neck}} \frac{\ln \alpha}{T} \frac{N_{ss} - N_{np}}{N_{np} - N_c^*} = 25^2 \times 31 \times \frac{\ln(1.5)}{35} \times 1.5 > 330 \mu \mathrm{m}^2/\sec,$$

which is over an order of magnitude faster than the measured diffusion coefficient for GFP in the cytoplasm ($< 30 \mu \mathrm{m}^2/\sec$).

9 Estimate of D_{mix} for spherical cells

For a tethered cell

$$D_{T,mix} = \frac{D}{L^2} \frac{V_{neck}}{V_{cell}}.$$

For a non tethered cell we have, assuming it is a sphere of diameter a, it can be shown

$$D_{NonT,mix} \approx 17.3 \frac{D}{4a^2}.$$

Hence,

$$\frac{D_{mix}(\text{nontethered})}{D_{mix}(\text{tethered})} = \frac{17.3 \frac{D}{4a^2}}{\frac{D}{L^2} \frac{V_{neck}}{V_{cell}}} = 17.3 \frac{L^2}{4a^2} \frac{V_{cell}}{V_{neck}}.$$

Using numbers from Section 8

$$a = 10\mu, \quad L = 25\mu, \quad V_{cell}/V_{neck} \approx 31$$

we get

$$\frac{D_{mix}(\text{nontethered})}{D_{mix}(\text{tethered})} \approx 838.$$

References

[1] Altschuler, S.J., Angenent, S.B., Wang, Y., and Wu, L.F. (2008) *On the spontaneous emergence of cell polarity,* Nature, Aug 14; 454:886-890.

[2] Cassimeris, L., McNeill, H., and Zigmond, S.H. (1990). *Chemoattractant-stimulated polymorphonuclear leukocytes contain two populations of actin filaments that differ in their spatial distributions and relative stabilities*. J Cell Biol 110, 1067-1075.

[3] Crocker, J.C., and Grier, D.G. (1996). *Methods of digital video microscopy for colloidal studies.* J Colloid Interface Sci 179, 13.

[4] Jacobs, M. (1967). Diffusion Processes. New York: Springer-Verlag.

[5] Jilkine, A., Angenent, S.B., Wu, L.F. and Altschuler, S.J. (2011) *A density-dependent switch drives stochastic clustering and polarization of signaling molecules*; PLoS Comput Biol 7(11): e1002271.

[6] Goryachev, A.B., and Pokhilko, A.V. (2008). Dynamics of Cdc42 network embodies a Turing-type mechanism of yeast cell polarity. FEBS Lett 582, 1437-1443.

[7] L. Edelstein-Keshet Mathematical Models in Biology McGraw Hill, 1988.

[8] Kervrann, C., and Boulanger, J. (2006). *Optimal spatial adaptation for patch-based image denoising.* IEEE Trans Image Process 15, 2866-2878.

[9] Mejean, C.O., Schaefer, A.W., Millman, E.A., Forscher, P., and Dufresne, E.R. (2009). *Multiplexed force measurements on live cells with holographic optical tweezers.* Opt Express 17, 6209-6217.

[10] Millius, A., Dandekar, S.N., Houk, A.R., and Weiner, O.D. (2009). Neutrophils establish rapid and robust WAVE complex polarity in an actin-dependent fashion. Curr Biol 19, 253-259.

[11] Mori, Y., Jilkine, A., and Edelstein-Keshet, L. (2008). Wave-pinning and cell polarity from a bistable reaction-diffusion system. Biophys J 94, 3684-3697.

[12] Subramanian, K.K., and Narang, A. (2004). A mechanistic model for eukaryotic gradient sensing: spontaneous and induced phosphoinositide polarization. J Theor Biol 231, 49-67.

[13] Otsuji, M., Ishihara, S., Co, C., Kaibuchi, K., Mochizuki, A., and Kuroda, S. (2007). A mass conserved reaction-diffusion system captures properties of cell polarity. PLoS Comput Biol 3, e108.

[14] van Kampen, N.G. Stochastic Processes in Physics and Chemistry, 1981, North-Holland.

[15] Weiner, O.D., Marganski, W.A., Wu, L.F., Altschuler, S.J., and Kirschner, M.W. (2007). *An actin-based wave generator organizes cell motility.* PLoS Biol 5, e221.

Supplemental Figure 1. Polarization behavior for cut cells is similar to highly stretched cells

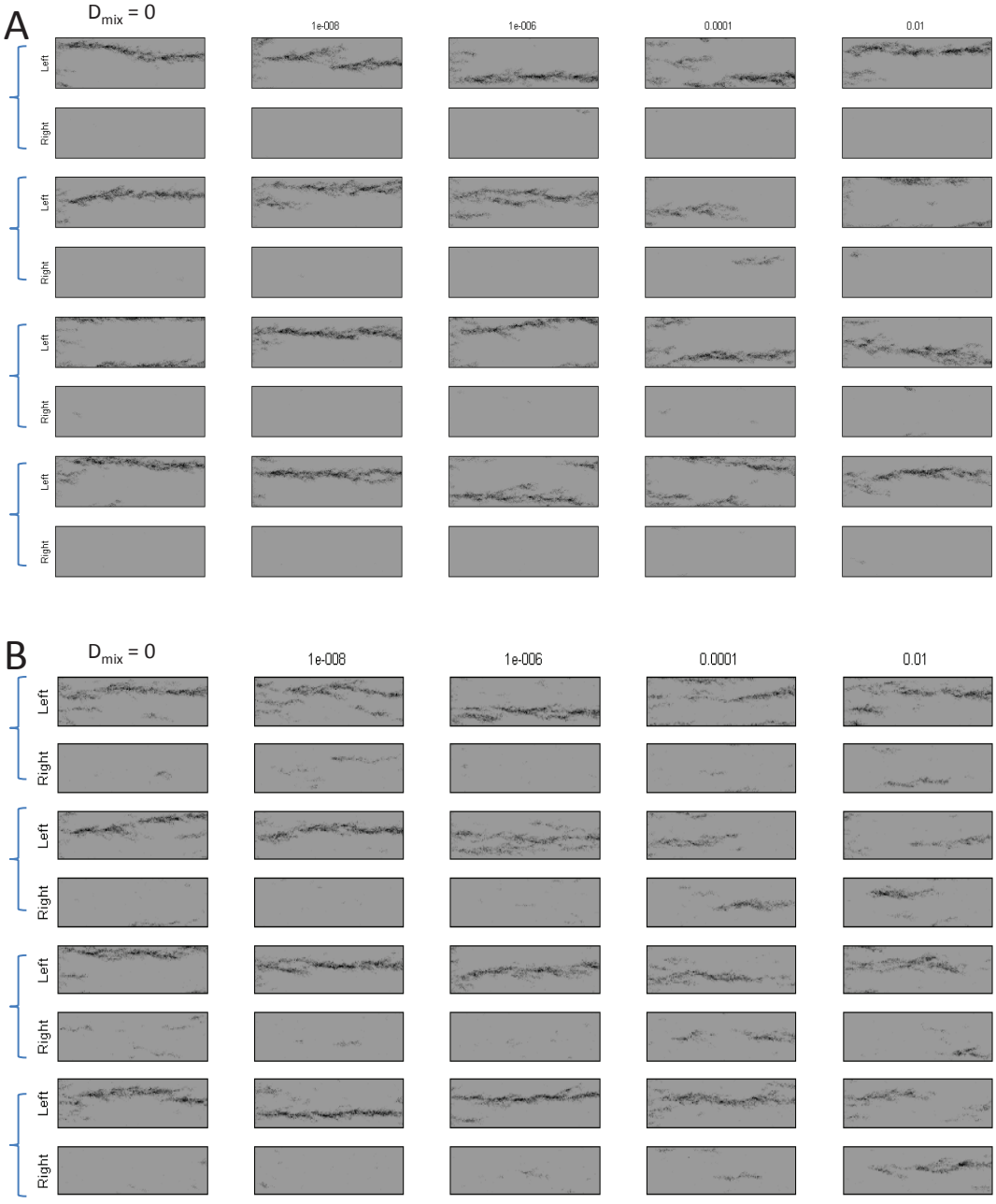

(A-B) Shown are simulation results of the neutral drift polarity model based on mass action kinetics with different spontaneous membrane association rates, kon: (A) kon = 0.0005, and (B) kon = 0.005. Other simulation parameters are given in supplemental materials. Each column was simulated with varying Dmix rates (0, 10-8, 10-6, 10-4, 10-2). Kymographs of 4 sampled simulations are shown, each with left (upper) and right (lower) halves. A total of 1000 particles were used. Initially, 550 were placed on the left, 450 on the right; on each half, 10% of the particles were randomly seeded on the membrane. Cut cells are in the leftmost column. Highly stretched cells are in the second and third columns from the left.

Supplemental Figure 2. Cutting the tether with a laser beam does not activate adjacent cells, related to Figure 3.

A) Shooting tether with laser beam does not cause SCAR/WAVE complex recruitment in adjacent cells

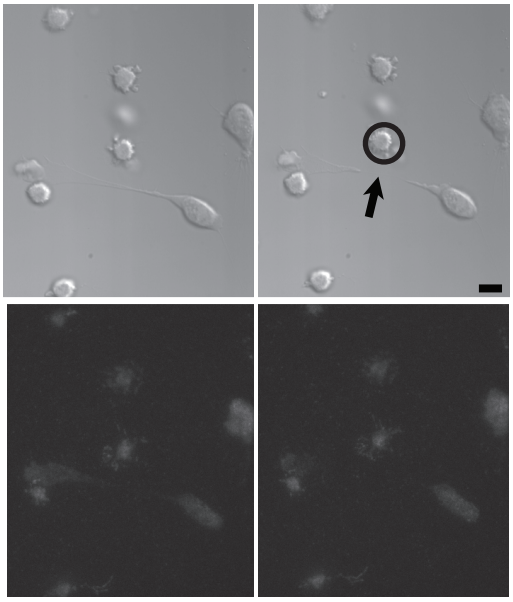

B) Shooting cell body with laser beam causes SCAR/WAVE complex recruitment in adjacent cells

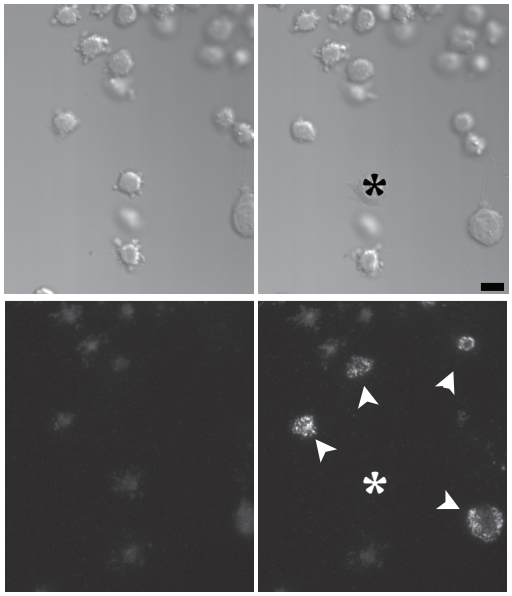

(A,B) HL-60 cells expressing Hem-1-YFP were incubated at 45C for 12 minutes and then imaged at 37C with DIC (top panels) and Total Internal Reflection Fluorescence (TIRF) microscopy (bottom panels), with one frame every five seconds. (A) Shooting the tether with a focused laser beam (black arrow) did not detectably activate neighboring cells (no increases in recruitment of Hem1-subunit of SCAR/WAVE complex to the membrane, bottom panel); scalebar = 10 microns. (B) The stage was then repositioned and an adjacent cell body was shot and destroyed (bold asterisk, corresponds to circled cell in (A)). Destroying the cell body activated SCAR/WAVE complex recruitment in several of the neighboring cells (arrowheads in bottom panel); scalebar = 10 microns.

Supplemental Figure 3, Correcting for fluorophore regeneration during FRAP experiments.

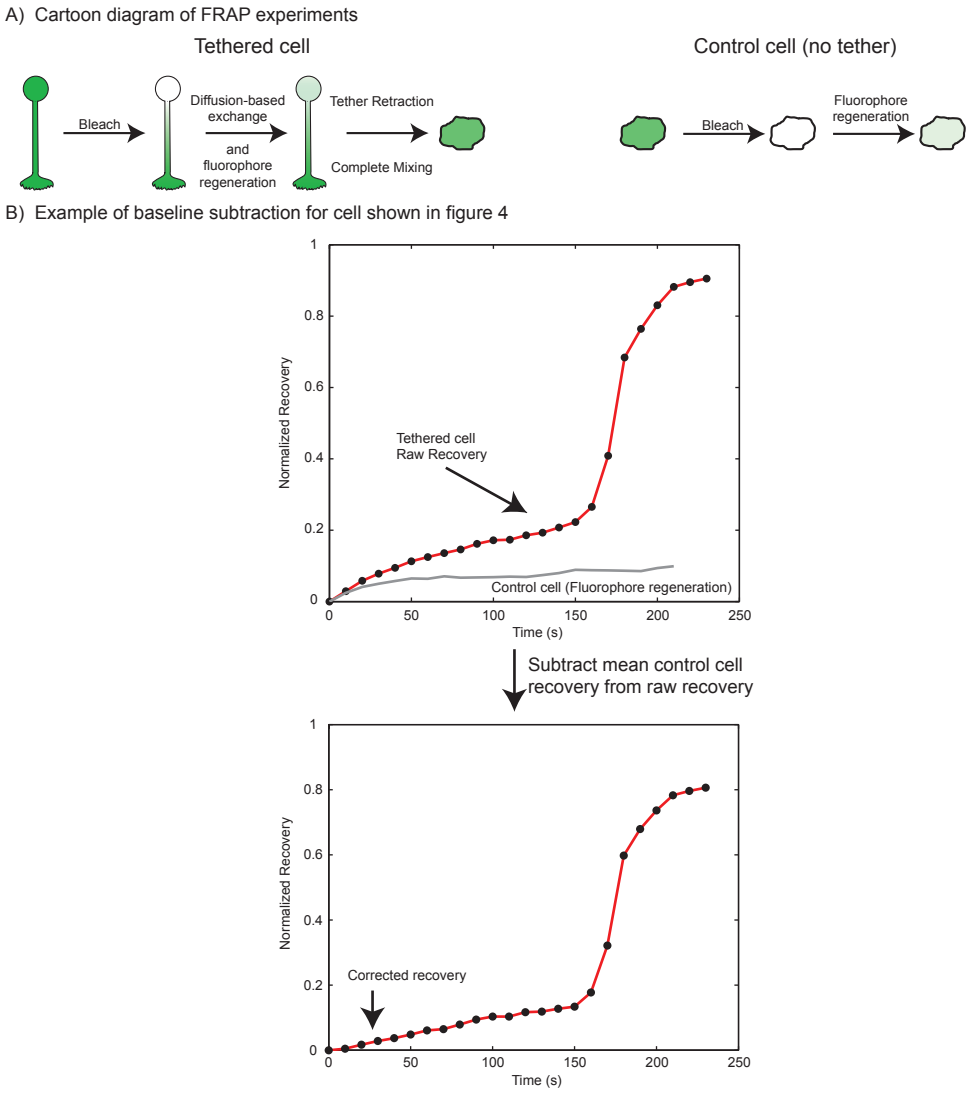

A) Cartoon diagram showing the bleaching of GFP in the cell body of a tethered cell (left) and bleaching all of the GFP in a control cell that lacks a tether (right). B) Top: Fluorescence recovery time course for a sample tethered cell (red) and the mean fluorescence recovery time course for control cells (grey). Note that there is significant recovery in control cells, about 10% of the bleached signal. Since these cells have no pool of unbleached GFP, we conclude that this recovery is due to fluorophore regeneration (reversible bleaching and GFP resynthesis). Bottom: We correct for fluorophore regeneration by subtracting the mean control cell fluorescence recovery from the fluorescence recovery of each tethered cell. The observed mixing rate constant $D_{mix,obs}$ is simply the initial slope of the normalized, corrected fluorescence recovery time course.

Supplemental Figure 4: Membrane tension measurements in presence of blebbistatin, related to Figure 5

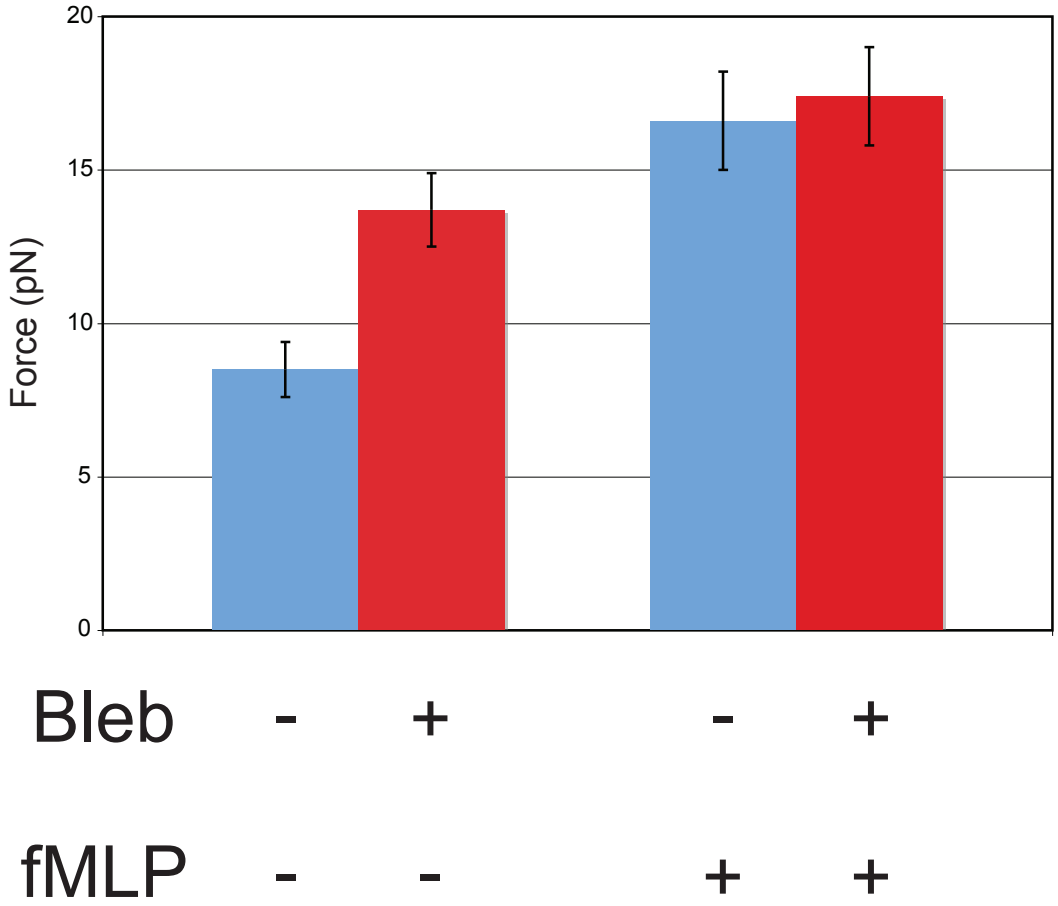

Graph of pulling forces for blebbistatin-treated or control neutrophils in the presence or absence of fMLP. Blebbistatin treatment caused the membrane tension to increase in the absence of fMLP. Pulling force increased from 8.5pN in negative controls to 13.7pN in blebbistatin-treated cells. This membrane tension increase was likely due to the elongated, stellate cellular morphologies caused by blebbistatin treatment. Chemoattractant stimulation caused the membrane tension to increase to the same value, regardless of whether the cell had been treated with blebbistatin.

Supplemental Figure 5, Analysis of Plasma Membrane Integrity during aspiration experiments.

A) There is no detectable GFP leakage during aspiration (N=5)

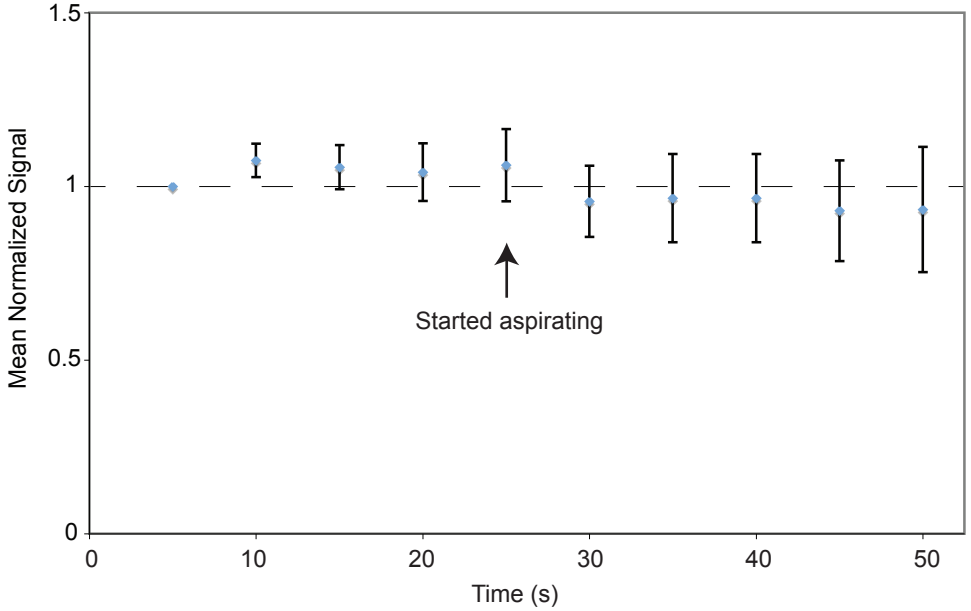

B) Poking with a broken needle causes dramatic GFP leakage

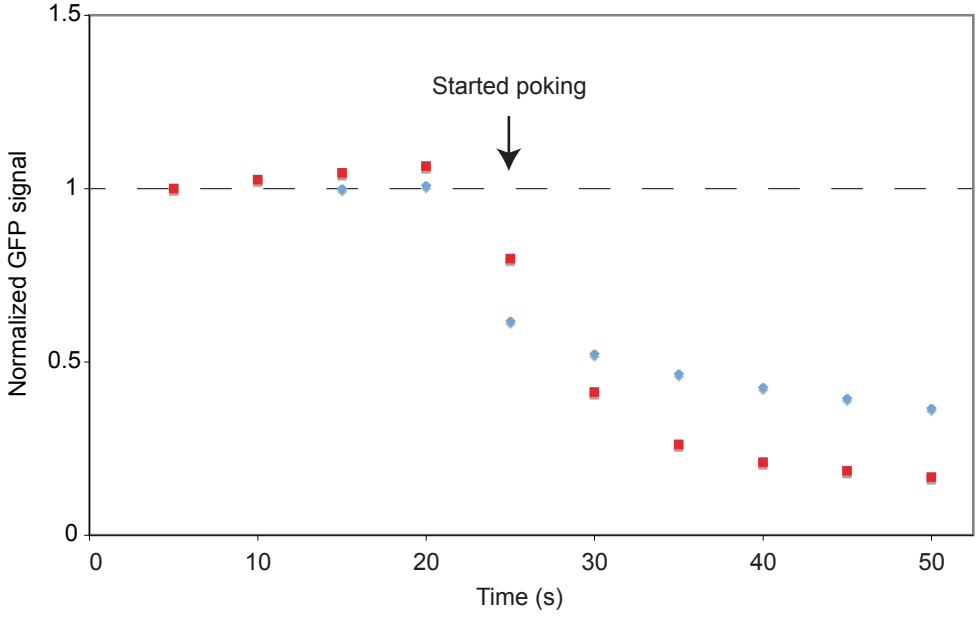

A) Quantification of cytoplasmic GFP signal during micropipette aspiration. Suction began at 25 seconds and did not cause a detectable drop in cytoplasmic GFP signal, indicating that there was no cytoplasm leakage during aspiration. B) We detect cytoplasmic leakage (significant reduction in cytoplasmic GFP signal) when we rupture the plasma membrane using a broken micropipette (N=2). Thus, we conclude that the plasma membrane stays intact during our aspiration experiments.

Supplemental Figure 6: Membrane tension reduction, but not cytoskeletal tension reduction, results in ectopic leading edge signaling, related to Figure 7

A Blebbistatin treatment causes elongated, stellate morphologies but no ectopic signaling

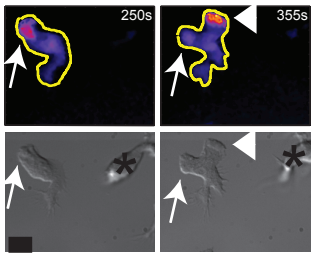

B Hypotonic buffer abolishes WAVE complex recruitment

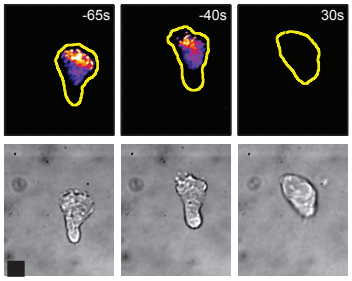

C Hypertonic buffer causes ectopic WAVE complex recruitment

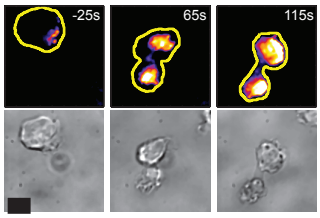

A) *Blebbistatin treatment causes elongated, stellate morphologies but no ectopic signaling.* Top: A crawling neutrophil expressing the SCAR/WAVE complex reporter Hem-1-YFP (visualized in TIRF mode, shown as a heat map) is shown 250s and 355s after blebbistatin treatment. Bottom: DIC images of the same cell shows cell morphology; the asterisks denote a neighboring cell. At 250s, the cell has an elongated morphology with a single active pseudopod (white arrow). At 355s, a new pseudopod has emerged (white arrowhead). The old pseudopod has not retracted (white arrow), giving the false impression of a multipseudopod phenotype in the still-frame DIC image. However, only the new pseudopod has SCAR/WAVE complex recruitment. Thus, signaling is still restricted to a single leading edge despite myosin inhibition.

B) *Hypotonic buffer abolishes WAVE complex recruitment.* Top: A neutrophil expressing Hem-1-YFP is shown before (-65s and -40s) and after (30s) application of hypotonic buffer (40% mHBSS final), which increases membrane tension. Increasing membrane tension abolishes SCAR/WAVE complex recruitment throughout the cell. Bottom: Brightfield images shows cell morphology. Hypotonic buffer causes the cell to stop protruding and round up.

C) *Hypertonic buffer causes ectopic WAVE complex recruitment.* Top: A neutrophil expressing Hem-1-YFP is shown before (-25s) and after (65s and 115s) addition of hypertonic buffer (150mM final). While WAVE complex recruitment was initially confined to a single leading edge, hypertonic buffer causes a second leading edge to emerge. Both leading edges in the hypertonic-treated cell have more WAVE complex recruitment than the untreated cell. Cells with multiple persistent pseudopodia are prevalent in hypertonically treated cells but rare in control cells. Bottom: Brightfield images show cell morphology.

CHAPTER FOUR

Summary and Future Directions

My graduate work produced three new insights into neutrophil motility:

1. The polarization of signals can occur via two distinct modes (polarized generation vs. uniform generation followed by selective retention). The mode chosen by the cell depends on the magnitude of chemoattractant stimulation.

2. Leading edge protrusion increases plasma membrane tension, which inhibits protrusive signals throughout the cell.

3. This inhibitory membrane tension is required to restrict Rac activity to a limited portion of the cell (the leading edge).

Our data support the following model for neutrophil polarization. First, leading edge protrusion increases tension in the plasma membrane. This tension rapidly propagates throughout the cell to act as a long-range inhibitor of leading edge formation. In support of this hypothesis, increases in tension suffice for long-range inhibition of Rac activation and protrusion, and decreases in tension expand leading edge activities. During cell polarization, tension only becomes significant after the front has formed, by which point positive feedback enables the existing front to maintain itself. Furthermore, since the front is the source of tension, any fluctuations in front size are immediately balanced by compensatory changes in tension levels. Our model also predicts that if the cell mistakenly builds two fronts, the tension will get very high and kill the weaker of the two fronts. Thus, the combination of a positive feedback loop with inhibitory membrane tension ensures that the cell focuses its protrusive efforts in one direction, enabling efficient migration. While we believe we have found the basic mechanism underlying neutrophil polarization, many important questions remain unanswered.

First, we must determine the mechanism by which tension inhibits Rac and the WAVE complex. The first line of experiments will be pharmacology and siRNA against known, or suspected, tension transducers that have been found in other cell types. We could increase tension with micropipette aspiration and see whether various drug treatments or gene knockdowns prevent the tension increase from inhibiting signals. Ion channels are thought to transduce tension and there are a myriad of channel blockers that could confirm that ion channels play a role and possibly identify the relevant ion. I doubt that we will identify the specific transducing channel with pharmacology because most compounds inhibit multiple channels. Src family kinases transduce cytoskeletal tension in fibroblasts and we could inhibit them with drugs or knock down their targets in neutrophils. Adhesions directly sense tension in fibroblasts. If adhesions transduce inhibitory tension in neutrophils then tension increases should have no effect on cells in suspension. We could also knockdown Talin, which transduces tension in adhesions. Curvature-sensitive GEFs and GAPs are good candidates for membrane tension transducers, so we could determine which neutrophil-expressed GEFs and GAPs contain BAR domains and then perform a focused siRNA screen on that candidate pool.

Perhaps WAVE complex waves directly transduce inhibitory tension. Unfortunately, we have no specific tools to change WAVE complex recruitment dynamics. Therefore, to investigate the role of waves as tension transducers, we must first determine the detailed biochemical mechanism of how they work. Only then will we be able to adjust wave dynamics in ways that should make them more or less tension sensitive and see whether these changes have the predicted effect. Therefore, we are beginning to biochemically dissect wave complex recruitment using lysates and supported lipid bilayers. From this, we hope to identify perturbations that cause static WAVE complex recruitment instead of propagating waves, which should cause uniform

spreading. Alternatively, increasing the wave stall force should cause a steady state morphology change such as wider leading edges or longer cells.

In addition to mechanistic information, we must also determine quantitative input/output relationships between cellular morphology, tension and signals. Much progress has already been made in this regard with respect to signaling. Sophisticated light-based dimerization strategies in combination with fluorescence based signaling readouts will soon enable us to measure quantitative relationships between many nodes in the motility signaling network.

Unfortunately, comparable tools for measuring and manipulating tension do not exist yet. All current methods for tension measurement have significant flaws. The optical trap method used in this thesis actually measures the sum of membrane tension and membrane-cytoskeleton adhesion. It is unclear whether the force contributions from these two terms can be distinguished from one another. Furthermore, actin assembly and lipid re-ordering within the membrane tubes reduce the measured force in a way that has nothing to do with membrane tension. Finally, it is extremely difficult to simultaneously make tension measurements from different regions of the same cell with optical traps. As a result, the critical assumption that tension is uniform throughout the cell membrane remains untested.

The situation is only slightly better for cytoskeletal tension. One can measure the resection of laser-induced holes in the cytoskeleton and estimate tension, but this is destructive and may perturb the cell. Traction force microscopy only reports unbalanced forces that pull or push on adhesions. If cytoskeletal tension is internally balanced or located in filament networks that do not couple to adhesions, then it will not be detectable with this method. Aspiration is a single-site measurement and so cannot measure the intracellular distribution of forces. It does not differentiate between membrane and cytoskeletal tension, either. Finally, the mathematical formulas used for

converting aspiration measurements into tensions were derived for spherical cells in suspension and may not be valid for nonspherical, adherent cells.

Fortunately, it should be possible to develop fluorescent tension readouts that overcome these limitations. Cytoskeletal tension readouts will probably come first. There are already fluorescence-based readouts for cytoskeletal forces applied to the adhesion protein Talin. The strategy is to make a construct that has two actin filament binding domains flanking a FRET pair separated by a flexible linker. Tension in the actin network will pull the actin binding domains apart separating the FRET pair and eliminating FRET signal. Alternatively, the actin binding domains could flank a concealed protein-protein docking site, to which a fluorescent-labeled protein binds. Tension would separate the actin-binding domains, exposing the docking site and relocalizing the fluorescent protein to the cortex.

There are several properties of membranes that could be exploited to develop membrane tension sensors. Membranes get thinner as they stretch, so lipophilic dyes whose quantum yield (or membrane incorporation) is sensitive to bilayer thickness should be tension-sensitive. Tension reduces the floppiness of the membrane as well. There are numerous protein domains that specifically bind curved membranes (BAR domains, e.g.). Tension should prevent a GFP-BAR fusion protein from binding the membrane. One can also envision a protein with two weak membrane-binding sites that can only bind the membrane when it induces a wrinkle that engages both binding sites. Such a construct should have difficulty binding a tense membrane that resists wrinkling. The presence of membrane folds and wrinkles could indirectly readout membrane tension. Some labs have used fluorescence to directly visualize large membrane folds that are flattened out when membrane tension increases in spreading fibroblasts. However, in neutrophils, the wrinkles are often smaller than the diffraction limit, making them difficult to visualize. Nevertheless, it might be possible to infer their presence from

fluctuations in plasma membrane intensity or the Z-position of membrane bound quantum dots. Super-resolution fluorescence techniques could directly visualize wrinkles, although they require fixation. These techniques will allow us to measure the magnitude and spatial distribution of tension in the membrane and cytoskeleton.

The currently available tools for tension manipulation are also unsatisfactory. Aspiration increases both cytoskeletal and membrane tension and one cannot tell which one affects signals. Stretching cells with deformable substrates activates signals via adhesions and also potentially changes both membrane and cytoskeletal tension. Detergents will perturb membrane proteins in addition to reducing membrane tension. Osmotic membrane tension perturbations are the least specific of all, as they change the concentration of every molecule in the cell.

We are trying to develop new tension manipulation tools that will be far more specific than anything currently available. We plan to use inducible wrinkle formation, inducible membrane traffic and pulling multiple membrane tethers to perturb membrane tension. We will add curvature-inducing proteins to the buffer in order to induce wrinkles, which should increase membrane tension by forcing the remaining unwrinkled membrane to cover a larger area. We can adapt the recently developed light-induced dimerization system to manipulate membrane trafficking. It is straightforward to pull multiple membrane tethers with an atomic force microscope. We can specifically decrease cytoskeletal tension with photo-unstable actin crosslinkers. Photo-induced crosslinkers could also enable us to rapidly change cytoskeletal stiffness. This will change the degree to which subsequent deformations increase tension. I do not know if light or drug-induced dimerization is energetic enough to deform the cytoskeleton and directly increase tension. Perhaps light or drug-induced activation of myosin could accomplish this. One fundamental caveat of all these manipulations is that the

membrane and cytoskeleton exert opposing forces on one another. Thus, increasing membrane tension will compress the cytoskeleton to some degree, and so on.

Finally, we must get a better idea of where endogenous tension comes from. We do not understand the relative importance of actin polymerization and hydrostatic pressure in generating membrane tension. We find that the cell never breaks symmetry in the presence of hypertonic buffer, suggesting that hydrostatic pressure is required to increase the membrane tension enough to antagonize signaling. We do not know whether actin assembly at the leading edge, and the resulting protrusion, increases cytoskeletal tension. Cytoskeletal tension increases during polarization but this is largely due to myosin activation. We could answer this question by directly inducing actin assembly (but not myosin activity) with light-based activation of a nucleation-promoting factor while monitoring cytoskeletal tension with a fluorescent readout. We do not know how adhesions affect cytoskeletal tension, either. By coupling to the extracellular matrix they could absorb tension and insulate the tensions in different cellular regions from one another. Fluorescent cytoskeletal tension readouts should resolve this issue easily.

Reciprocal interactions between signaling and mechanics are an increasingly appreciated design principle in biology. This is an exciting time for our field given the large number of fundamental questions that remain unanswered. Hopefully, new techniques will pave the way towards a deeper understanding of the interplay between signaling, forces and form.

Publishing Agreement

It is the policy of the University to encourage the distribution of all theses, dissertations, and manuscripts. Copies of all UCSF theses, dissertations, and manuscripts will be routed to the library via the Graduate Division. The library will make all theses, dissertations, and manuscripts accessible to the public and will preserve these to the best of their abilities, in perpetuity.

Please sign the following statement:

I hereby grant permission to the Graduate Division of the University of California, San Francisco to release copies of my thesis, dissertation, or manuscript to the Campus Library to provide access and preservation, in whole or in part, in perpetuity.

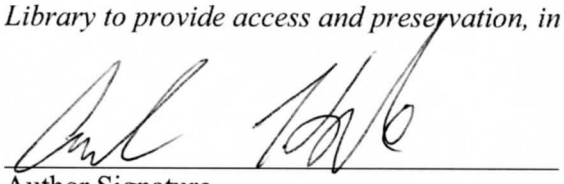

Author Signature

12/18/11

Date